SISSA - SCUOLA
INTERNAZIONALE
SUPERIORE
DI STUDI AVANZATI
TRIESTE
Strada Costiera 11

ISAS - INTERNATIONAL SCHOOL
FOR ADVANCED STUDIES

Global Properties of Early–type Galaxies

Thesis submitted for the degree of
"Magister Philosophiae"

Astrophysics Sector

Candidate:

Nicola CAON

Supervisor:

Professor
M. CAPACCIOLI

Academic Year 1990/91

TRIESTE

Contents

Introduction

The simultaneous advent of CCD detectors and of more and more powerful image processing facilities in the last 10 years has allowed to collect large amounts of reliable photometric and spectroscopic data. Together with observations in non–conventional spectral bands (radio, UV, X), they have deeply changed our current understanding of what elliptical galaxies are. In fact elliptical galaxies appears no longer the simple objects they were thought to be, but complex multicomponent systems. Under the same apparent morphology, there seem to coexist at least two families of E's, with different physical properties. The first is formed by disky systems, which have kinematic, radio and X properties similar to those exhibited by S0 galaxies, and are the continuation of the sequence of lenticular galaxies toward vanishingly small bulge–to–disk ratios. The second is composed of boxy galaxies, which are characterized by heterogeneous kinematic properties and are usually powerful radio and X–ray sources; they are likely to be the result of mergers. On the other hand, regardless of boxiness or diskyness, inside the dimensional space defined by luminosity, scale length, projected central dispersion, central density, and metallicity, all elliptical seem to lie on a plane, that is any of the listed parameters is a function of other two of them. This does not contradict the division of ellipticals in distinct families, as it means only that they obey the same physical law, i.e. to the Virial theorem.

It must be noticed that the investigation of the properties of elliptical galaxies is often plagued by the use of samples made of sparse and/or distance–unconstrained objects, or of apparent magnitude–limited samples, biased toward intrinsically bright objects. Moreover, since the use of different samples and/or of different techniques to extract the relevant astrophysical quantities may give different results, and even produce spurious correlations, as we shall see in the thesis, it is of vital importance to define and study galaxy samples as complete and homogeneous as possible.

This need is the motivation of the present line of research of the writer. The aim is to perform the photometric mapping of a sample of about 65 E and S0 galaxies belonging to the Virgo and to the Fornax Clusters, and to extract the set of all relevant geometrical and photometric parameters, to be complemented by kinematic data. The key features of this project are the completeness of the sample, which includes all the early–type galaxies brighter than $M_B = -17.3$,

the fact that galaxies belongs to two cluster placed at about the same distance from the observer, which minimizes the errors related to the determination of the distance–dependent parameters; and the quality of the material and the techniques used (the coupling of CCD and photographic images), which permits to reach a state–of–art accuracy. This in turn will allow a really unbiased and statistically significative study of the properties of early–type galaxies.

In this thesis we wish to present an up–to–date review of our knowledge on elliptical galaxies, with particular emphasis on those aspects closer to the research project above outlined. Chapter 1 describes the main photometric and kinematic properties of early–type galaxies.

Chapter 2 is devoted to the discussion of the 'manifold' of early–type galaxies and of the so–called Fundamental Plane of elliptical galaxies, together with its interpretation in the frame of the Virial theorem. Moreover, the correlation between effective radius and effective surface brightness is re–examined, showing that for galaxies at fixed total luminosity there is actually a large spread in the effective parameters.

In Chapter 3, after a brief summary of the techniques used to detect isophotal patterns, the correlations of the isophote shapes with global parameters are presented, and the division of elliptical galaxies into distinct subfamilies is discussed.

In Chapter 4 we present original data concerning the isophotal properties of a sample of E and S0 galaxies in the Virgo and of Fornax cluster. Chapter 5 concerns the properties of the stellar disks found in early–type galaxies, the ways of modelling galaxies as the sum of two or more components, and their use as diagnostics of the galaxian structure.

The intrinsic shapes of elliptical galaxies and bulges is considered in Chapter 6, where either photometric and kinematic evidences for triaxiality are analysed.

In Chapter 7 the components of external origin, such as dust lanes, shells, polar rings are briefly described.

Chapter 8 is devoted to a review of the properties of the interstellar medium, in particular of the X–ray emitting hot gaseous halo in elliptical galaxies. A new evolutionary model of the hot gas content and X–ray emission is discussed at some length.

UV emission by elliptical galaxies is described in Chapter 9.

Lastly, Chapter 10 presents a brief account of the chemical and photometric evolution models for elliptical galaxies.

Chapter 1

Photometric and kinematic properties

1.1 Fitting laws

The first analytical formula used to describe the luminosity profile of a spheroid was the Reynolds–Hubble one, applied to the central part of the Andromeda nebula (see HUbble 1930):

$$\frac{I(r)}{I(r_0)} = 4\left[1+\frac{r}{r_0}\right]^{-2}$$

The area integral of this equation diverges, but this fact has no physical consequence, as galaxies have finite size.

1.1.1 The $r^{1/4}$ law

In 1948, performing the photographic surface photometry of three early–type galaxies, de Vaucouleurs presented a new fitting formula, called the de Vaucouleurs $r^{1/4}$ law:

$$I_(r) = I_e\, 10^{-3.3307\left[(r/r_e)^{1/4}-1\right]}$$

or

$$\mu(r) = \mu_e + 8.3265\left[(r/r_e)^{1/4}-1\right]$$

where r_e, called *effective radius*, is the equivalent radius of the isophote containing half of the total luminosity (the equivalent radius of an isophote is defined as the radius of that circle which enclose the same area of the isophote), and μ_e is the corresponding (*effective*) surface brightness.

The $r^{1/4}$ law, which is shape–free, as it depends on only two scale factors, has been proposed as a purely empirical law, without any physical meaning; because of its proved ability to represent with a fair accuracy the luminosity profile of E galaxies and bulges of S0's and spirals over a wide range of surface brightness, it has been extensively used as a standard ruler by observers, and as a reference or as

an input constraint by theoreticians. On the other hand, dissipationless collapse can naturally provide a physical justification of the $r^{1/4}$ law, as it is obtained starting from fairly general initial conditions (Aguilar & Merrit 1990); in addition to a first–order agreement with the de Vaucouleurs law, recent N–body simulations (Londrillo, Messina & Stiavelli 1991) have been shown to produce also the observed departures from the average $r^{1/4}$ behaviour.

A detailed description of this law and of related formula can be found in App. A.

There are essentially two ways to compute the scale parameters of the $r^{1/4}$ law (Capaccioli 1989). The first consists in fitting with a straight line: $y = ax + b$the luminosity profile in the $(r^{1/4}, \mu)$ plane. The scale parameters are then given by

$$r_e = (8.3265/a)^4 \qquad \mu_e = B + 8.3265$$

. This means that the error on r_e is related to that on a by: $\delta r_e/r_e = 4\,\delta a/a$. Since $\delta a/a$ can be easily larger than 5% even in the best studies, the effective radius is determined with an uncertainty of about 20%. The second way to measure r_e and μ_e is through their definition. In case of deep surface photometry ($\mu_B(lim) \sim 28$), such as that obtained by coupling CCD images with photographic scans, it is possible to compute the total integrated luminosity L_T with only a small extrapolation term, of the order of 5%, and therefore to derive the isophote containing half of the total light. Since $L_T \propto r_e^2$, we have $\delta r_e/r_e = 1/2\,\delta L_T/L_T$, so the formal error on r_e is $\sim 3\%$ (ignoring photometric scale errors).

The second method seems to be preferable to the first, if an accurate deep photometry can be obtained. In fact it makes use of the definition of the effective parameters, and is less sensitive to photometric errors. On the contrary, the first method, when applied to CCD luminosity profiles which describe the inner region of the galaxies, expecially for large ones, can give results which are not representative of the entire galaxy.

The main advantages of the $r^{1/4}$ law are its simplicity (but the spatial emissivity does not have a simple analytical representation), its ability to reasonably well fit the light profiles of normal E's and bulges over an ample interval of surface brightness, and the providing of a coordinate transformation which turns most of a light profile into a straight line. Furthermore, it has been revealed very useful to analyse light profiles in terms of deviations from the best $r^{1/4}$ fitting, which was a key point in discovering the presence of substructures such as disks, bars, shells.

1.1.2 Other fitting formulae for elliptical galaxies

Several other fitting formulae have been proposed and applied to describe light profiles of early–type galaxies.

Baum's (1955) formula:

$$\frac{I(r)}{I(r_0)} = 2\left[\frac{r}{r_0}\left(1+\frac{r}{r_0}\right)\right]^{-1}$$

coincides with Reynolds–Hubble for $r \gg r_0$, and is steeper at small galactocentric distances, diverging at $r = 0$. Also the area integral diverges with r.

Oemler's (1976) formula:

$$\frac{I(r)}{I(r_0)} = 4\left[1+\frac{r}{r_0}\right]^{-2} \exp\left(-\frac{r^2 - r_0^2}{\beta^2}\right)$$

is almost coincident with Reynolds–Hubble in the core region, and is progressively steeper at increasing distances. The free parameter β is a convenient tool for modelling the variety of shapes of the outer light profiles of giant ellipticals.

King's (1962) formula:

$$\frac{I(r)}{k} = \left\{\frac{1}{[1+(r/r_c)^2]^{1/2}} - \frac{1}{[1+(r_t/r_c)^2]^{1/2}}\right\}^2$$

developed to model the projected density distribution of globular cluster, has been applied also to profiles of elliptical galaxies (King 1966). it is semi–empirical, as it is related to quasi–isothermal isotropic dynamical models. It has two characteristic lengths: the *core* radius r_c, where the surface brightness is half of the peak value, and the *tidal* radius r_t, where $I(r)$ falls to zero. While dwarf spheroidal are indeed tidally truncated, normal ellipticals are not. With an appropriate selection of the tidal radius King's formula may be adjusted to match closely the $r^{1/4}$ law.

Sersic's (1968) formula:

$$\frac{I(r)}{I_0} = \exp\left(A\, r^{2/n}\right) \qquad \begin{cases} n = 8 & (r^{1/4}) \text{ law} \\ n = 2 & \text{exponential law} \end{cases}$$

is a generalization of the $r^{1/4}$ law, and contemplates also the case of the exponential law.

Jaffe's (1983) formula: concerns the spatial emissivity rather than the projected brightness:

$$\rho(r) = \frac{1}{4\pi}\left(\frac{r}{r_\star}\right)^{-2}\left(1+\frac{r}{r_\star}\right)^{-2}$$

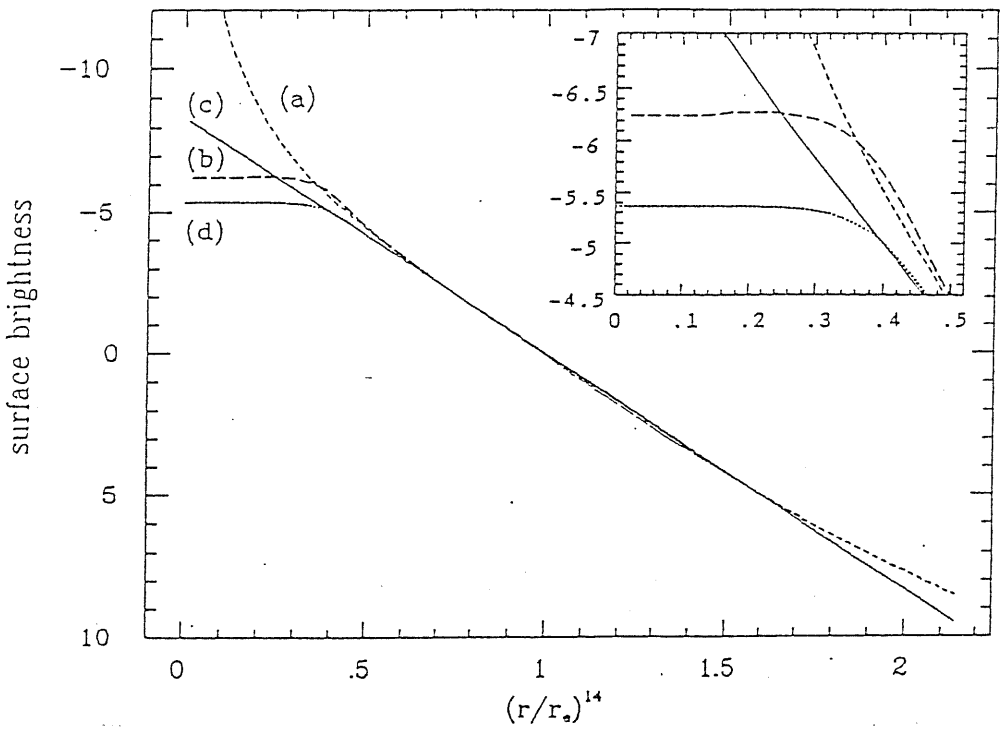

Figure 1.1: Comparison between Jaffe's (a) and de Vaucouleurs' (c) luminosity laws; the effective radius is the same for both formulae. The two laws are very similar over the total range covered by observations of large galaxies ($0.1 \div 8r_e$), except the region affected by seeing: in this range the Jaffe's law show a small but clear concavity in the $(r^{1/4}, \mu)$ plane. (b) and (d) represent the two formulae convolved with a same gaussian PSF having $\sigma_\star = (1/60)r_e$; while the convolved $r^{1/4}$ law becomes flat at small radii, Jaffe's law maintains an innermost steeper gradient (see also the blow–up in the inset). From Capaccioli (1989).

r_* is the radius of the spherical surface containing half of the total luminosity; the radius containing half of the projected total luminosity is: $r_e = 0.763 r_\star$. The projected surface brightness at distance r from the center is:

$$I(x) = \begin{cases} (4x)^{-1} + \left[(1-x^2)^{-1} - (1-x^2)^{-3/2}\,(2-x^2)\,\mathrm{arccosh}(1/x)\right]/2\pi & x < 1 \\ (4x)^{-1} - \left[(1-x^2)^{-1} + (x^2-1)^{-3/2}\,(x^2-2)\,\arccos(1/x)\right]/2\pi & x > 1 \end{cases}$$

where $x = r/r_*$. Jaffe's law produces light profiles very similar to $r^{1/4}$ ones, with Jaffe's law showing a slight upward concavity in a $(r^{1/4}, \mu)$ plot, as is sometime found in elliptical galaxies (Fig. 1.1). It has a much easier representation for the spatial emissivity, while the surface brightness run is a deal more complicated.

1.1.3 The exponential/sech^2 law for disks

Disks, provided they are not seen edge–on, are generally described by an exponential law:

$$I(r) = I_0 e^{-r/h}$$

where I_0 is the central surface brightness and h is the scalelength radius. It is a convenient fitting formula, because of its semplicity and its capability to describe disk luminosity profiles.

As for the edge–on disks, the observations of brightness profiles perpendicular to the equatorial plane suggest the sech^2 formula for the volume emissivity (see Kormendy 1982):

$$\rho(r,z) = \rho_0 e^{-r/r_0} \mathrm{sech}^2(z/z_0)$$

z_0 is the scale height in the z direction perpendicular to the plane. The sech^2 dependence describes a self–gravitating sheet of stars in which the vertical velocity dispersion σ_z is independent of z. Neglecting internal absorption, the above equation gives the following projections:

$$\text{face–on} \qquad I(r) = 2\rho_0 z_0 e^{-r/r_0}$$

which corresponds to the exponential law;

$$\text{edge–on} \qquad I(r,z) = 2\rho_0 r K_1(r/r_0)\mathrm{sech}^2(z/z_0)$$

where K_1 is a modified Bessel function of the first kind.

Further useful formulae relative to the exponential and the sech^2 laws can be found in Appendix A

1.2 Color and line–strength gradients

The variation of colors within and between ellipticals is a well–known characteristic of early–type galaxies. In general, more luminous elliptical galaxies tend to be redder and more metal rich; however, color gradients are markedly weaker in ellipticals than in disk galaxies.

Even if too many poorly known parameters govern the chemical evolution of galaxies: initial mass function, yield, star formation efficiency, gas flows and winds (see Sect. 10), the color–luminosity relation and the color gradients can give valuable information on the galaxy formation process. In fact, if galaxies were formed purely by dissipation, the most massive galaxies would have the largest color gradients (Carlberg 1984), whereas mergers cause initial color gradients to decrease (*e.g.* White 1979). Furthermore, since the number of mergers undergone by a galaxy is expected to increase with luminosity, a decrease of the color gradient with luminosity is expected.

It is generally assumed that color changes indicate changes in metallicity. The best evidence comes from the spectroscopic measurements of absorption line in ellipticals (*e.g.* Thomsen & Baum 1989). In fact, colors and absorption–line strengths run in parallel. The Mg b and Fe absorption–line strengths are stronger in high mass ellipticals, which are redder; in individual galaxies, line strengths generally decrease outward from the center, and colors tend to get bluer outwards. This also indicate that dust absorption is not a major factor in color variations.

Analysing a sample of 17 elliptical galaxies, Franx and Illingworth (1990) have computed the mean color gradients:

$$\Delta(B-R)/\Delta\log r = -0.07 \pm 0.01$$

and

$$\Delta(U-R)/\Delta\log r = -0.23 \pm 0.03$$

Remarkably, the gradient $\Delta(U-R)/\Delta(B-R)$ among galaxies is very similar to the ratio of mean gradients within galaxies $(\Delta(U-R)/\Delta\log r)/(\Delta(B-R)/\Delta\log r)$. This suggest that the same mechanism produces color variations within galaxies and among galaxies.

Vader *et al.* (1988) and Peletier *et al.* (1990) have searched for possible correlations of the color gradients with other structural parameters. While the latter found no relation between total luminosity and color gradient, nor is there a relation between color gradient and $(v/\sigma)^*$, the former claim that anisotropic, pressure–supported ellipticals tend to have smaller color gradients, and that color gradients in boxy ellipticals get smaller as boxiness increases. Kormendy & Djorgovski (1989), combining together three samples of CCD multiband photometry, showed that color gradients are weak or absent at low luminosities ($M_B > -20$), and largest near the peak of the luminosity function ($M_B = -20$), as shown in Fig. 1.2.

Franx & Illingworth (1990) present evidences that the local color is a function of the local escape velocity, which is related to the effective radius and velocity dispersion by: $v_{esc} = \langle\sigma\rangle F(r/r_e)$, where $\langle\sigma\rangle$ is the root mean square velocity dispersion and F is a dimensionless function (Fig. 1.3). This suggest that the local escape velocity is the primary factor that determines the metallicity of the stellar population. However, given the present level of development of galaxy formation models, the metallicity–local escape velocity relation does not allow the exclusion of any of the proposed mechanism for producing metallicity gradients.

As for the line–strengths, a detailed study by Gorgas, Efstathiou, & Aragon salamanca (1990) shows that, at variance with previous belief (Faber 1977), there are large variations in the Mg_2 gradients from galaxy to galaxy (see Fig. 1.4), and the same holds for other line–strength gradients such as Mg_1, Mgb, and the iron lines.

The importance of the Mg_2 index is due to its sensitivity to metallicity and insensitivity to the shape of the IMF. There is some evidence that galaxies with high

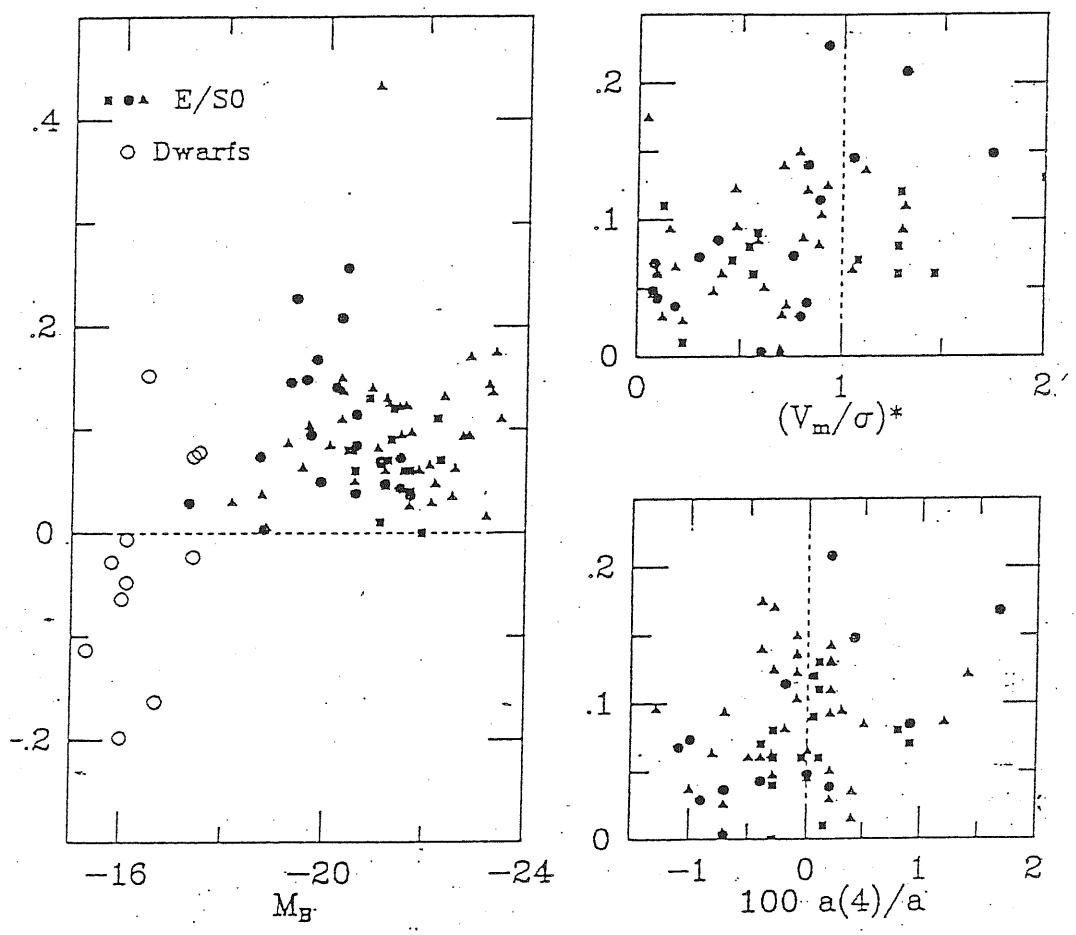

Figure 1.2: Correlations of color gradients with other galaxy properties. Gradients are defined as $\Delta(\text{Color})/\Delta(\log r)$, in magnitude per decade in radius; positive values indicate reddening toward the center. From Kormendy and Djorgovski (1989).

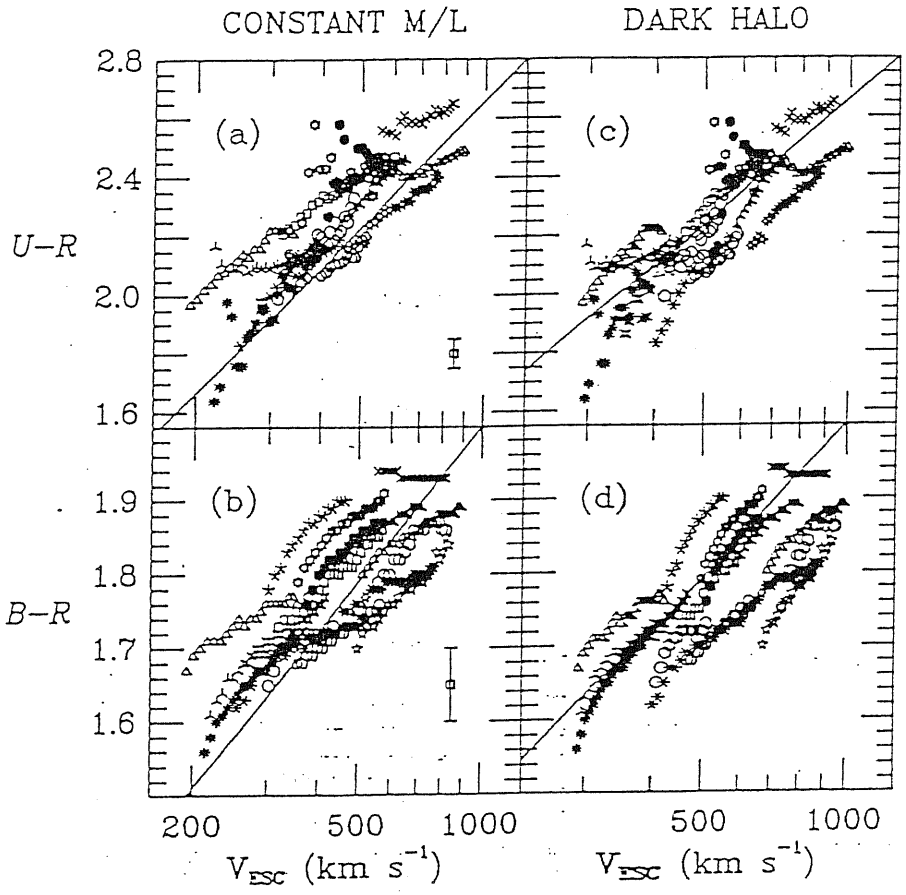

Figure 1.3: Local color as a function of the local escape velocity. Each galaxy is plotted with a different symbol. In (a) and (b) the M/L ratio is assumed to be constant throughout the galaxy; in (c) and (d) the galaxies are assumed to have dark halos with total mass being 10 times large than the luminous mass. The thin lines have the slope predicted from the relation between mean color and central velocity dispersion. From Franx & Illingworth (1990).

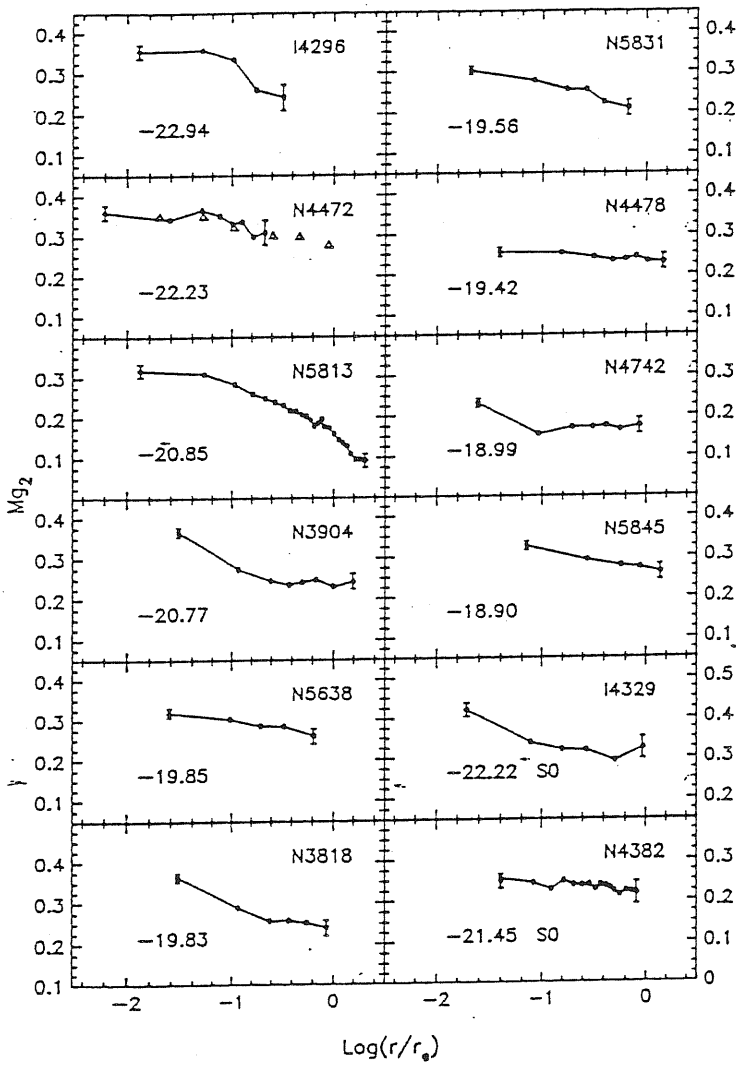

Figure 1.4: Major axis gradients in 12 early–type galaxies. Mg_2 is plotted versus $\log(r/r_e)$, where r_e is the effective radius. The error bars give an estimate of the errors for the inner and outer points. From Gorgas *et al.* (1990).

central velocity dispersions and high central line–strengths tend to have steeper gradients. The corresponding metallicity gradient is relatively weak: typically, the metallicity drops from about $2 \div 3$ times solar abundance in the nuclear regions to about solar abundance at $r \sim 0.5 - 1 r_e$. cD galaxies are characterized by shallower gradients than the mean for normal Es.

This figures suggest that elliptical galaxies have experienced different star formation histories, which can be easily interpreted in the context of the formation of E galaxies by merging.

1.3 Rotation and anisotropic pressure

When Bertola and Capaccioli (1975) discovered that the elliptical galaxy NGC 4697 posses a rotation velocity too low to be compatible with the flattening being produced by stellar rotation, a new interest raised on the kinematical properties of ellipticals.

The investigation of a sample of luminous ellipticals by Illingworth (1977) showed that all of the elliptical observed had slow stellar rotation, which provide insufficient support to account for their flattening. On the other hand, the bulges of a sample of edge–on spiral galaxies had rotation velocities and flattenings consistent with them being oblate, isotropic rotators. In 1983 Davies *et al.*, motivated by the realization that these bulges were on the average about 2 mags fainter than the ellipticals studied by Illingworth, studied a sample of 11 low–luminosity ellipticals, finding that their kinematic behaviour was more similar to that exhibited by the bulges than that showed by the brighter ellipticals.

On the bases of the results above described, theoreticians started trying to find a new mechanism, different by rotation, capable of produce the observed flattening. The right answer to this problem was given by Binney (1978), who proposed that elliptical galaxies may have anisotropic velocity dispersion, that is, for an axisymmetric system, the mean–square random velocity along the symmetry axis is lower than that on the equatorial plane.

Let us consider an axisymmetric system which rotates about its symmetry axis (the z–axis), is seen edge–on, and whose only streaming motion is rotation about the z–axis. The anisotropy parameter δ is defined by:

$$\Pi_{zz} = (1 - \delta)\Pi_{xx} = (1 - \delta) M \sigma_0^2$$

where Π_{xx} and Π_{zz} represent respectively the x and the z components of the kinetic energy tensor, M is the total mass and σ_0^2 is the mass–weighted mean–square random velocity along the line of sight to the galaxy. By applying to this system the tensor Virial theorem we can obtain the following formula:

$$\frac{v_0^2}{\sigma_0^2} = 2(1 - \delta)\frac{W_{xx}}{W_{zz}} - 2$$

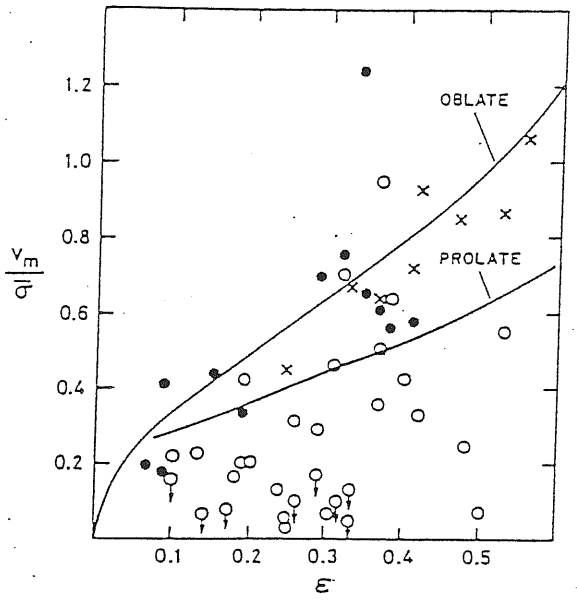

Figure 1.5: Ratio of the peak rotation velocity to the velocity dispersion plotted against observed ellipticity. Open circles are luminous ellipticals ($M_B < -20.5$), filled circles are faint ellipticals and crosses are bulges of spirals. The mean line for oblate isotropic galaxies and the median line for prolate isotropic galaxies are shown. From Davies (1987).

where v_0^2 is the mass–weighted mean square rotation speed, and W_{xx} and W_{zz} are the x and z components of the Chandrasekhar potential energy tensor. For a system whose isodensity surfaces are similar concentric ellipsoid, the ratio W_{xx}/W_{yy} depends only on the ellipticity ε_e of these surfaces, and not at all on the radial density structure. Therefore, the quantity v_0/σ_0 depends on ε_e and δ only.

This relation suggests a diagnostic tool, known as the v/σ test, to measure the degree of anisotropy of an elliptical galaxy. It consists in comparing the position of the representative points of the galaxies in the $(V/\sigma,\varepsilon_e)$ plane with the line corresponding to the oblate, isotropic model with $\delta = 0$ (see Fig. 1.5); in general V is the maximum rotation velocity, σ is the dispersion velocity averaged within $1/2\ r_e$, and ε_e is the apparent ellipticity.

We shall notice that the ellipticity corresponding to to the model is the intrinsic one; however, it can be shown that projection effects move the model practically along the same line, if the intrinsic flattening is lower than 0.6. Galaxies which lie close to the model line are therefore isotropic rotators, while galaxies below this line are characterized by anisotropic pressure, whose importance is related to the distance from the model line. The degree of anisotropy is measured by $(V/\sigma)^*$, the ratio of V/σ to the value corresponding to the isotropic model of equal ellipticity. Fig. 1.6 plots $(V/\sigma)^*$ against absolute magnitude for a sample of normal ellipticals, cD and brightest cluster galaxies, and bulges. It is evident

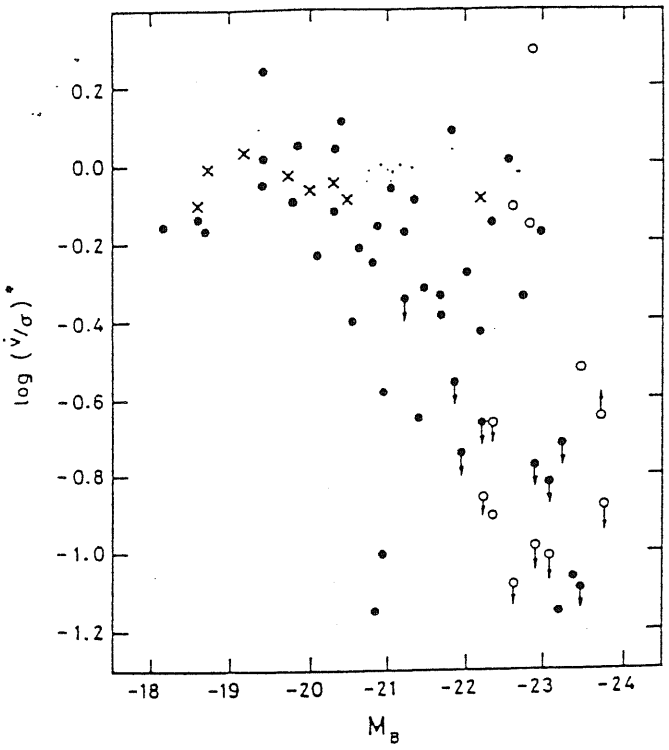

Figure 1.6: log $(v/\sigma)^*$, the value of v/σ normalized to the value expected for oblate isotropic galaxies of equal flattening, plotted versus absolute magnitude. Filled circles are ellipticals, crosses are bulges, open circles represent cD and brighter cluster galaxies. From Davies (1987).

that galaxies of different luminosities have different kinematical behaviour: while low–luminosity ($M_B > -20.5$) ellipticals and bulges are supported by rotation, the bright ellipticals form a much less homogenous group characterized by a very large spread of values of $(V/\sigma)^*$.

An important remark on the use of the $(V/\sigma/\varepsilon)$ test to disky ellipticals has been made by Nieto, Capaccioli & Held (1988). In fact, the application of the test requires that we measure the quantities specific to the spheroid. While the presence of an embedded faint disk should not significantly affect the kinematical measurements, so that the observed quantities can be safely taken as referring to the spheroid, the disk is expected to produce two effects on the ellipticity profile: 1) a purely photometric one, the presence of the disk yielding a flatter ellipticity, 2) a real physical effect, the disk potential contributing to the flattening of the bulge.
The authors performed the test taking for the ellipticities a value appropriately chosen to represent the bulge flattening, and showed that the luminosity range within which E's are isotropic oblate rotators is higher than reported before; moreover, they conclude that all statistical analysis of large samples of E's can give

inconclusive or contradictory results because of the mixture of different populations.

1.4 Minor axis rotation and triaxiality

The result that a great part of elliptical galaxies are not supported by rotation but by anisotropies in their velocity dispersion indicate that they do not have to be oblate spheroids, but can have a triaxial shape.

A triaxial galaxy seen along practically any line of sight will show rotation both along the minor and major axis, as the projections of the main axes will not coincide with the observed major and minor axes; vice versa, in the absence of figure rotation, elliptical galaxies showing rotation along both of the projected principal axes can not be oblate rotators. Therefore, study of the triaxiality requires at least both major and minor axis kinematic measurements. Franx, Illingworth, & Heckman (1989) have studied major and minor axis kinematics of a sample of 22 elliptical galaxies. They define the kinematic misalignment angle Φ as:

$$\tan \Phi = \mid \frac{v_{minor}}{v_{major}} \mid$$

where v_{minor} and v_{major} are the maximum rotation velocities along the photometric main axes; a value $\Phi = 0$ indicates that the galaxy does not have minor axis rotation, while $\Phi = 90$ degrees indicates rotation around the long axis. 60% of the galaxies in the sample have their kinematical axis within 10 degrees of the photometric minor axis, while about 30% show kinematic misalignments larger than 30 degrees; in two cases, rotation on the minor axis is larger than rotation on the major one (see Fig. 1.7).

These percentages suggest that ellipticals that rotate about their long axes ('spindle'–like) are rare, and that it is unlikely that ellipticals are generically prolate tumbling bars. On the other hand, the lack of minor axis rotation, and therefore a close to zero misalignment angle, does not necessarily mean that the galaxy is oblate, because triaxial galaxies show little minor axis rotation for many viewing angles.

It is interesting to see whether isophote twists, which is thought to be produced by changes in the intrinsic flattening of triaxial galaxies, is correlated to minor axis rotation. Franx *et al.* find that galaxies with high kinematic misalignment ($> 60^{\circ}$) show a small kinematic twist, while galaxies with intermediate misalignments all show large photometric twist; furthermore, galaxies with large photometric twist all have a twist of the sign opposite to the sign of the misalignment. This could mean that the intrinsic shape of the galaxies may be different in the inner regions than in the outer ones, specifically that galaxies are nearer to oblate at the inner regions, and more triaxial in the outer regions (see also Sect. 6.3).

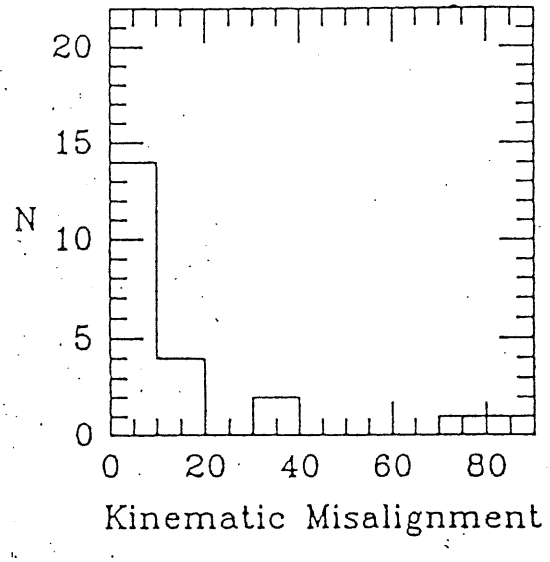

Figure 1.7: Histogram of the kinematic misalignment angle Φ. From Franx *et al.* 1989.

1.5 Kinematic subsystems

The first kinematically–distinct, rapidly–rotating nuclear components was discovered in the giant elliptical IC 1459 (Franx & Illingworth 1988). In this galaxy, one quarter of the stars in the core of IC 1459 out to a radius of 5 arc–seconds rotate in the opposite sense to those in the bulk of the galaxy; core stars have a much greater rotation velocity than the main part of the galaxy. The higher v/σ of the central component led to suggest that it could be a disk.

In other cases, a core rotating at a skew angle has been detected. While counter–rotation between core and main body can be a stable phenomenon in an axisymmetric galaxy, inclinations around 90 degrees between the angular momenta of core and main body indicate a triaxial shape, or a not yet completely static configuration. Detailed kinematic information of the core of NGC 5322 has been obtained by looking at the broadening function, that is the line–of–sight velocity distribution (Fig. 1.8).

It reveals that the core of NGC 5322 most likely consist of two kinematically decoupled components (Bender 1990). One of them counter rotates rapidly with respect to the main body of the galaxy, and contributes about one third to the light of the core.

The most accepted explanation for core subcomponents is the merging; however, it is an astonishing fact that ellipticals with peculiar core kinematics occur in all kinds of environment, ranging from dominant cluster galaxies to object in small groups, and there is no correlation with environment. Several scenarios can be imagined (Bender 1990):

Accretion of a gas–rich companion: Gas settles in the core, and subsequent

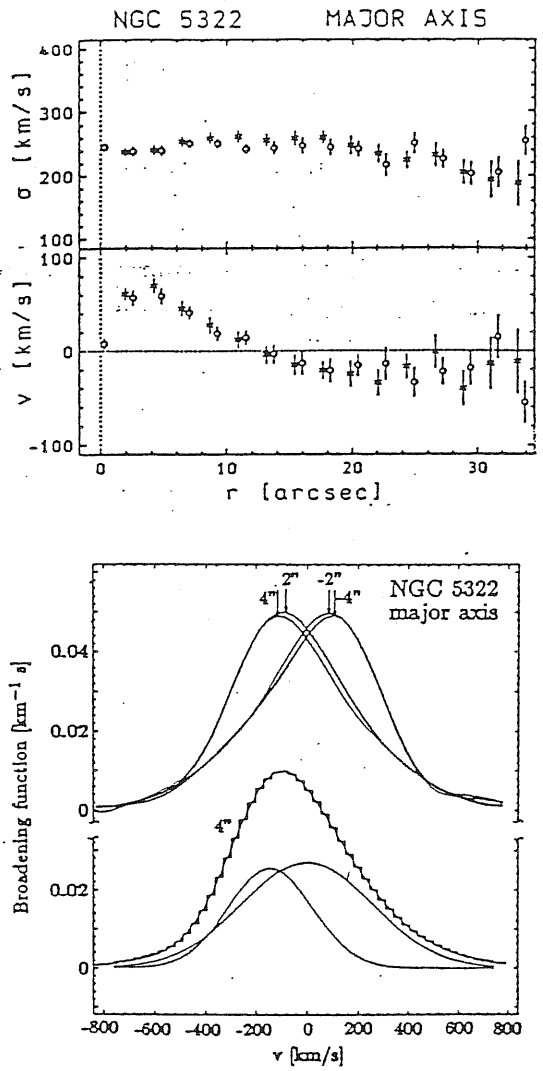

Figure 1.8: Upper panel: Rotation velocity V and velocity dispersion σ of NGC 5322 along the major axis. The curves were folded around the symmetry axis with different symbols referring to different sides. Lower panel: the line-of-sight velocity distribution (broadening function) of NGC 5322 on the projected major axis at ± 2 arcsec and ± 4 arcsec distance to the center, along with the broadening function at 4 arcsec fitted by the superposition of two Gaussians. From Bender (1989).

star formation leads to a stellar counter–rotating core; the rotation reflects the orbital angular momentum.
Merging of a luminous elliptical with a low–luminosity compact elliptical which settles in the core of the merger
Merging of two spirals as suggested by observations of obvious mergers and of IRAS galaxies.
Multiple merging in compact groups: the dynamical evolution of a compact group most likely results in a elliptical.

Weak counter–rotation can also be explained by less violent processes like:
'Primordial' misalignment: N–body simulations of collapsing proto–galaxies have shown how misaligned angular momenta between core and main body can be produced (Barnes & Efstathiou 1987)
Tidal torques: which could be able to reverse the outer parts of a lower luminosity companion of a massive galaxy (May, van Albada, & Norman 1985)
Bar motions: low amplitude counter–streaming could be due to motions in a bar (Bettoni 1989).

Of course, more detailed inner kinematics observations, as well as more extensive theoretical analysis and N–body simulations, are needed to constrain these possible formation scenarios and also to give hints to the shape of the central potential.

1.6 Measurements of the mass–to–light ratios

Several methods have been conceived to measure the mass–to–light ratio of an elliptical galaxy. However, they are able to give only qualitative results, due to the uncertain assumptions at the basis of the methods. Moreover, if the M/L ratio of ellipticals is, like spirals, an increasing function of the radius, due to the presence of dark matter, the resulting values will depend on which part of the galaxy is measured.

One of the most direct method is the King's or core fitting method (see Binney & Tremaine 1987). It is assumed that the surface brightness profile of the galaxy (or at least that of its inner regions) is fitted by an isothermal sphere (see Sect. 1.1.2). Computing the core radius r_c and measuring the line–of–sight velocity dispersion σ, the central density is derived by use of:

$$\rho_0 = \frac{9\sigma^2}{4\pi G r_c^2}$$

Then, the central luminosity density is $j_0 = 0.495 I(0)/r_c$, from which the mass–to–light ratio is $M/L = \rho_0/j_0$.

It is obvious that this method gives the correct results so long as the isothermal model is a good description of the physics of the galaxian core, and, as shown in

Sect. 3.4, this assumption is far from being correct.

Another method is known as Poveda's formula. It assumes a spherical galaxy, in which both light and mass follow exactly the $r^{1/4}$ law, and with an isotropic velocity dispersion tensor. The M/L ratio is then yielded by:

$$M/L = \frac{0.210\sigma_0^2}{GI_e r_e}$$

where σ_0 is the central line–of–sight velocity dispersion. Of course all of the assumptions are wrong in differing degrees for all real galaxies.

A method which makes use of all the available data, not just central or average values consists in the application of the Jeans equation to a spherical, or nearly spherical system. In a galaxy in which both the density and the velocity structures are invariant under rotations about the galactic center, the velocity ellipsoids are spheroid with their symmetry axes pointing to the galaxy center. If we define:

$$\beta(r) = 1 - \frac{v_\theta^2}{v_r^2}$$

as the degree of anisotropy of the velocity distribution at each radius, where v_{theta} and v_r are the tangential and radial velocity dispersions respectively, the Jeans equation can be rewritten as (see Binney & Tremaine 1987):

$$M(< R) = -\frac{r v_r^2}{G}\left(\frac{d\ln\nu}{d\ln r} + \frac{d\ln v_r^2}{d\ln r} + \beta\right)$$

where ν is the volume luminosity density. Observations give the surface brightness at each projected radius $I(R)$ and the line–of–sight velocity dispersion $\sigma_p(R)$. Since only two functions are measured, while the mass $M(r)$ depends on three undetermined functions $v_r(r)$, $\beta(r)$ and $\nu(r)$, it is not possible to derive the radial run of $M(r)$ from observations alone. However, a unique mass model can be derived from the observational data if one of the free functions is constrained to follow some a priori law.

For instance, we can assume that the velocity ellipsoids are spherical throughout the galaxy, so that $\beta = 0$. This is the case of the mass measurements by X–ray emission, where $M(r)$ is obtained by coupling the above formula with the hydrostatic equilibrium equation (see Sect. 8.6.4). Alternatively, one can assume a constant mass to light ratio Γ, measuring it through, for instance, the Poveda formula and derive the radial run of the anisotropy parameter.

In any case, observational data are not able to allow precise measurements of the mass–to–light ratios, least of all to construct detailed mass models. However, a straight application of the Poveda formula to a sample of about 200 galaxies (see Sect. 2.2) give values which have a relatively small spread (0.21 in log), which, taking into account measurements errors, indicate an intrinsic broadening of only 30%, fully accounted for by differential shape and anisotropy effects. Therefore, the

M/L ratio should change by less than a factor ten over four orders of magnitude in luminosity. Of course, these measurements refer to the inner regions (say inside the effective radius) of the galaxy, thereby they do not are influenced by the presence of dark matter is it has a much shallower distribution than the luminous matter.

The evidence of the presence of dark matter comes from non–stellar kinematic indicators that are sometime available on a large scale, such as X–rays (see Sect. 8.6.4) or HI. Other evidences of dark matter come from stellar kinematic observations of some cD galaxies (Dressler 1979), in which the velocity dispersion is seen to rise from the center to about 470 km s^{-1} at $\sim$ 100 kpc. If the velocity dispersion is assumed to be isotropic and constant over the $10 \div 100$ kpc range, at $\sim$ 450 km s^{-1}, this implies that M/L rises as $\sim r^{0.4}$ in this range.

The use of stellar disks to measure the M/L ratio of S0 galaxies is discussed in Sect. 5.5.

1.7 The Luminosity Function of E and S0 galaxies

The Luminosity Function (LF) of different morphological types are widely different, and the total LF over all types is the sum of many single, mostly bell–shaped curves. The total LF shows humps and bumps according to the underlying type–specific LFs, and often it can not be modelled by a simple function, such as the Schechter function.

The type–specific LFs are found to be the same in the field and in clusters; however, owing to the variation of the type mixture as a function of the environment, there can not be universal total LF.

We can study the LF of both E and S0 looking at the Virgo Cluster, for which a thorough and detailed study of the LF of all Hubble types has been carried out by Sandage, Binggeli and Tammann (1987). The LF of both E and S0 galaxies have a maximum and decreases toward zero at magnitude brighter than $M_B \sim -15$ (Fig. 1.9).

The LF of E galaxies is skewed toward faint magnitudes, being shallow at the bright end but with a sharp cutoff at the faint end. The opposite holds for S0 galaxies, whose LF is skewed toward bright magnitudes, with a steep rise at the bright end and a shallow decline at the faint end. The global E + S0 LF then is a nearly symmetric bell–shaped curve.

This result has been discussed by Capaccioli & Caon (1991), who pointed out that the LF of E + S0 galaxies posses a secondary maximum at a very high luminosity ($M_B \simeq -21.5$, Fig. 1.10). This maximum reflects the fact that, for the brightest objects of the galaxy sample studied by Caon, Capaccioli and Rampazzo (1990; thereinafter CCR), they measured total luminosities which are systematically in excess of the values currently found in the literature.

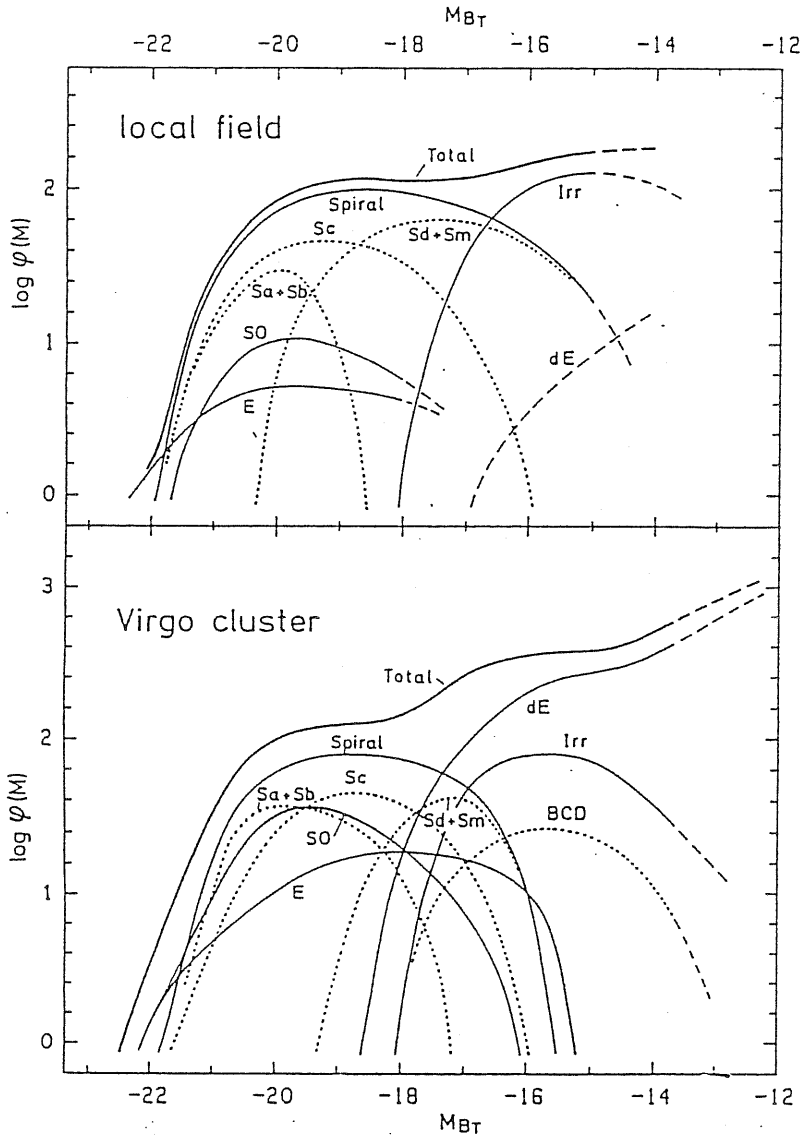

Figure 1.9: The luminosity function of field galaxies (top) and Virgo cluster members (bottom). The zero point of log $\phi(M)$ is arbitrary. The LFs for individual galaxy types are shown. Extrapolations are marked by dashed-lines. From Binggeli, Sandage, & Tammann (1988).

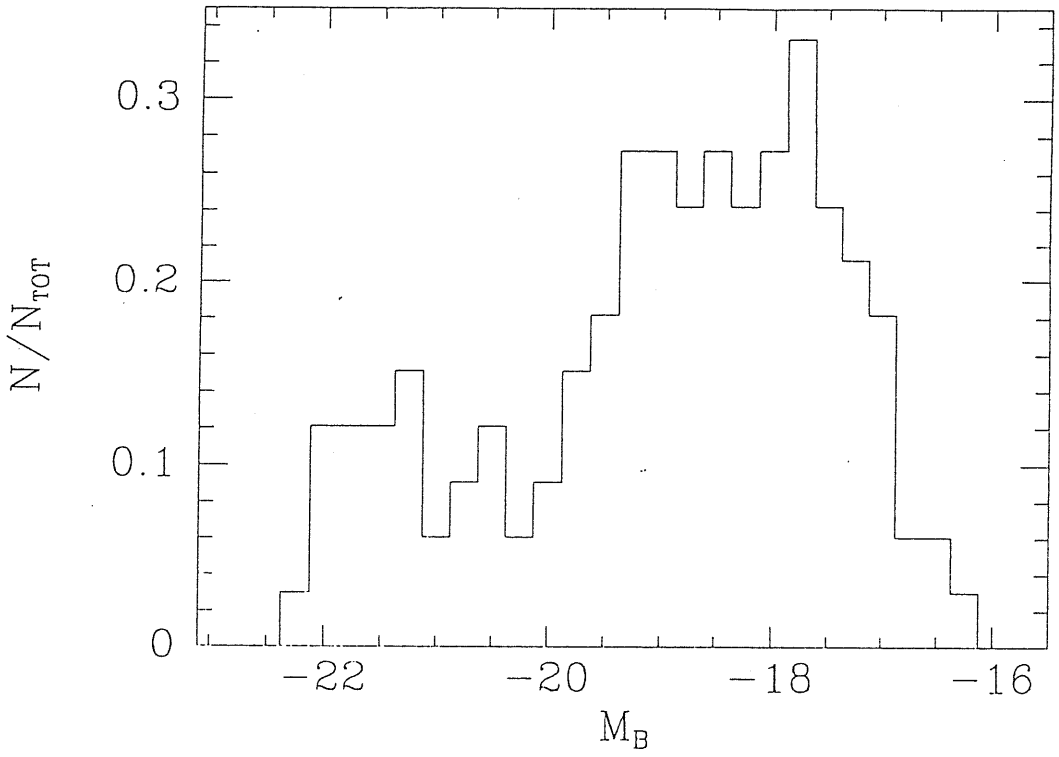

Figure 1.10: The luminosity function for the 33 E and S0 galaxies belonging to the Virgo cluster sample. Raw data have been smoothed by a running window 1.0–mag wide, moved in steps of 0.25 mag.

Chapter 2

The manifold of elliptical galaxies

2.1 Parameters correlations and scaling laws

The main astrophysical use of surface photometry and kinematic data is the study of parameter correlations and scaling laws. On one side, they contain valuable information about galaxy formation and evolution; on the other side, correlations between distance–dependent and distance–independent quantities are essential for the mapping the large scale structure and velocity fields.

It has long been recognized that galaxies can not be describe as a one–parameter family, that is there is no single parameter (for instance, the luminosity) upon which all the other parameters (effective radius and effective surface brightness, mass, etc.) depend univocally.

Herein lies the problem of the "minimal manifold of galaxies" (Brosche 1973), that is, how many and which physical quantities are necessary and sufficient to describe a family of normal galaxies? Knowledge and understanding of the minimal manifold of galaxies would provide a benchmark for the theories of galaxy formation, and dynamical models of elliptical galaxies.

Many, but not all, properties of early–type galaxies correlate with luminosity (see Kormendy 1982). The best known of these is the Faber–Jackson (1976) relation: $L \propto \sigma^n$. The slope is $n \simeq 4$, but with a real variation depending on the sample definition. However, in almost all cases there is a residual scatter, not accountable by the measurements errors, which is indicative of one, or more, hidden parameters; but there was no clear understanding or agreement as what the second parameter may be. For instance, Terlevich *et al.* (1981) proposed that the second parameter in the Faber–Jackson relation is metallicity, measured by the Mg_2 index; their results were challenged by Tonry and Davis (1981), and then readdressed by Efstathiou & Fall (1984). de Vaucouleurs & Olson (1982), on the contrary, suggested that the hidden parameter was the surface brightness. The poor data set available at that time did not permit a resolution of the problem.

Multi–parameter correlations were discovered through studies of correlated residuals from relation such as the Faber–Jackson, a method known as multibi-

variate statistics. In practice, first a linear least–square fit is performed on two quantities, then possible correlations of the residuals with other parameter are searched for. In the positive case, a linear combination of that quantity and one of the previous two is made, and the fit is optimized again. The fit quality is judged on the bases of the χ^2 values and linear regression coefficients. This approach is preferred to more sophisticated statistical tools like Principal Component Analysis (PCA) (*e.g.* Brosche 1973, Efstathiou & Fall 1984, Murtagh & Heck 1987), as astrophysics can get lost in too many eigenvectors (Djorgovski 1987).

2.2 The Fundamental Plane of elliptical galaxies

The multibivariate statistical method was applied by Djorgovski and Davis (1987) to a sample formed by about 200 early–type galaxies with surface photometry by Djorgovski (1985), and central velocity dispersion measurements by Tonry and Davis (1981) and the compilation by Whitmore, Mc Elroy, & Tonry (1985). For each galaxy, measurements of radius, magnitude, mean and local surface brightness, slope of the surface brightness profile, ellipticity, ellipticity gradient and isophotal twist, all measured at or within the effective radius (obtained from the fits of surface brightness to the $r^{1/4}$ law), and central velocity dispersions and line strength measurements were available.

They found that the residuals of $L-\sigma$ and $R-\sigma$ relations correlate well with the mean surface brightness $\langle\mu\rangle$, and vice versa, while σ and $\langle\mu\rangle$ do not correlate at all. A linear combination of $\log\sigma$ and $\langle\mu\rangle$ (distance–independent) with logs of L or R (distance–dependent) produce excellent fits, with no residual scatter, that is not accountable by the measurement errors. The new distance–indicator relations, which at the same time are the equations of a plane (the so–called "Fundamental Plane") in the L (or R) – σ – $\langle\mu\rangle$ parameter space, are:

$$M = -8.62(\log\sigma + 0.10\langle\mu\rangle) + 16.14$$

or

$$L \propto \sigma^{3.45}\langle SB\rangle^{-0.86}$$

and

$$\log r_e = 1.39(\log\sigma + 0.26\langle\mu\rangle) - 6.71$$

or

$$R \propto \sigma^{1.39}\langle SB\rangle^{-0.90}$$

where $\langle SB\rangle$ denotes the mean surface brightness in linear flux units, and r_e is measured in pc. The power–law coefficients of σ and $\langle\mu\rangle$ are uncertain by about 10%. The Fundamental Plane of elliptical galaxies is graphically represented in Fig. 2.1.

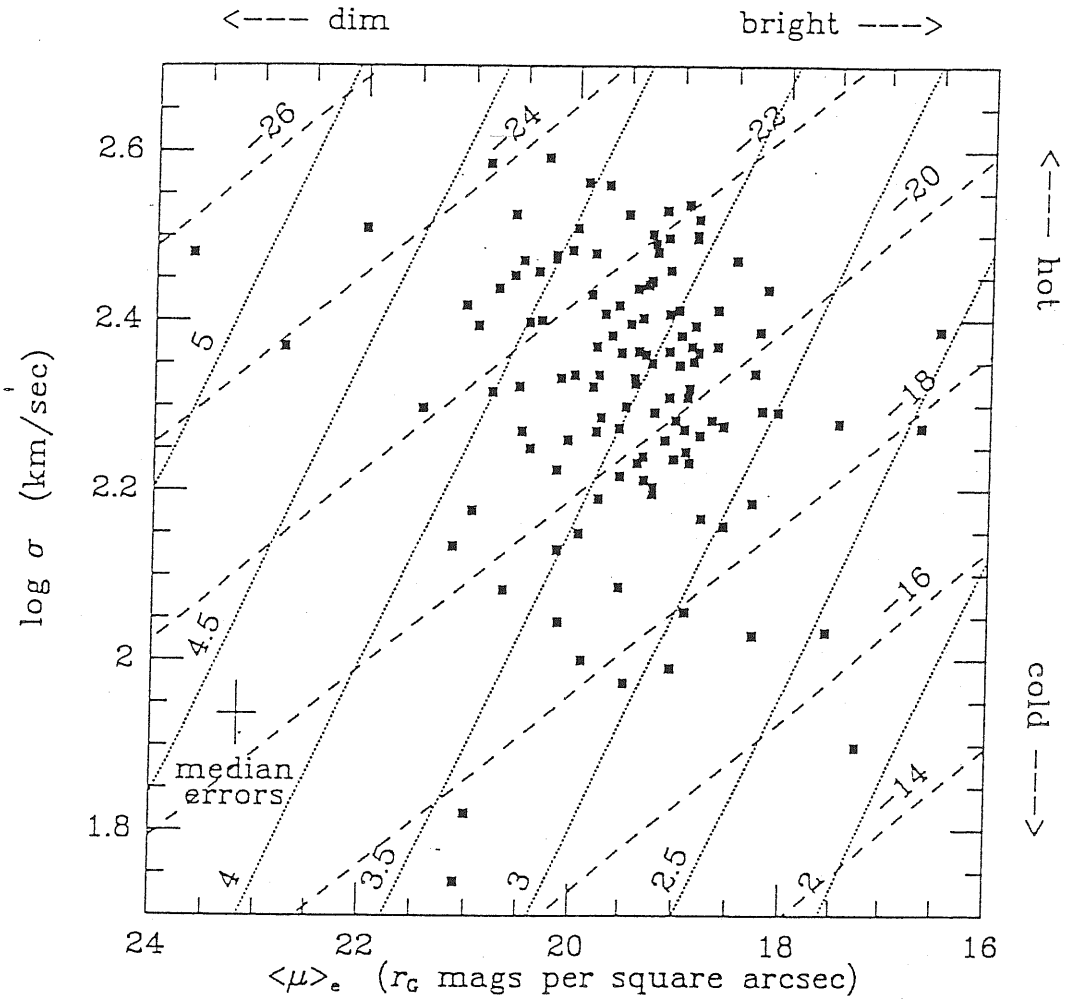

Figure 2.1: The Fundamental Plane of elliptical galaxies, shown trough the observable quantities: the projected central velocity dispersion σ (km s^{-1}) and the mean surface brightness within the r_e isophote $\langle\mu\rangle$, in r_G magnitudes per square arcsec. The dashed lines indicate loci of equal absolute magnitudes, and the dotted line indicate loci of equal semimajor axis r_e in pc, expressed as logarithms (base 10).

Introduction of line strengths and colors do not improve the fits significantly. Beyond this, the residuals of the above relations do not correlate with any other morphological or spectroscopic quantity, indicating that two dimensions provide an adequate and exhaustive description of the global properties of elliptical galaxies.

The Fundamental Plane is remarkably thin, as its thickness is contained in the measurements errors. Furthermore, none of the shape parameters (ellipticity, ellipticity gradients, isophotal twist) correlate with velocity dispersion or any other global quantity related to the Fundamental Plane (luminosity, surface brightness) and, moreover, the shape parameters do not correlate among themselves. Also the kinematic variable $(V/\sigma)^*$ does not correlate with any of the photometric parameters.

We may ask whether the FP is flat. One physical mechanism which may introduce deviations from the plane could be dissipationless mergers, which may afflict the "bright" end. In any case, the plane appears to be flat within the measurement errors, and any slight curvature should not introduce distance errors larger than $\sim 5 \div 10\%$. it is possible that there are small differences in the tilts and/or intercepts of the Fundamental Plane in different large–scale environments, which could reflect some real fluctuations in the process of galaxy formation; however, such differences are often hard to separate from selection effects (see Djorgovski, de Carvalho & Han (1989).

It is also possible that galaxies in different environments lie on the same plane but populate different portions of it. The analysis of a sample of 50 S0 galaxies shows that their global properties also form a two–dimensional family, and that the equations of their Fundamental Plane are very similar, and possibly identical, to the plane of elliptical. Also in S0's the shape parameters do not correlate with the global properties, which suggests a fundamental continuity between ellipticals and S0's.

We conclude that the elliptical galaxies are a $2 + n$ parameter family, defined by the following observables:

1) velocity dispersion
2) surface brightness
3) a variety of shape parameters

2.3 Other forms for the Fundamental Plane

A nearly equivalent result was achieved independently by Dressler *et al.* (1987), who have applied their solution to the mapping of the large–scale velocity field. They suggested that the Faber–Jackson relation can be made significantly tighter if the new parameter D_n, defined as the circular diameter within which the mean surface brightness reaches a certain fiducial value, *e.g.* $\mu = 20.75$ B–mag arcsec^{-2}, is used in place of the total luminosity. These author show that the $D_n - \sigma$ relation is

equivalent to the Fundamental Plane equations, provided that all elliptical galaxies have brightness profiles of the same shape.

If used as a distance indicator, the FP provide distances to galaxies accurate to about 20%, which makes the FP as good as the best version of the Tully–Fisher relation for spiral galaxies.

Motivated by the observations that colors of early–type galaxies correlate well with velocity dispersion (see Sect. 1.2), and that metallicity should be less affected by the internal dynamics (anisotropy, rotation) than the projected velocity dispersion, de Carvalho & Djorgovski have attempted to substitute colors in place of velocity dispersions in the equations defining the FP. This would have also the advantage that colors are much easier to measure and calibrate than the velocity dispersions, and thus large numbers of galaxies can be surveyed relatively quickly. They found that colors which are fairly metallicity–sensitive, such as $(V-K)$ or the Gunn $(v-r)$ work fairly well, giving relative errors on predicted distances of about $25 \div 30\%$ per galaxy. The scatter reduces to $\sim 15 \div 20\%$ if the Mg_2 index is used; however, the Mg_2 index requires spectroscopy and is thus more expensive to measure and calibrate in terms of observing time.

2.4 The Fundamental Plane and the Virial theorem

The Fundamental Plane can be understood using simple arguments (Djorgovski *et al.* 1989) based on the Virial theorem. For any galaxy bound by the newtonian gravity the following equations holds:

$$\frac{GM}{\langle R \rangle} = k_E \frac{\langle V^2 \rangle}{2}$$

where M is the galaxy mass, G the gravitational constant, $\langle R \rangle$ a suitable mean radius defined so that the left side of the above equation is the potential energy, $\langle V^2 \rangle / 2$ a mean kinetic energy per unit mass, and k_E the virialization constant ($= 2$ for a virialized system). The observational counterparts of M, $\langle R \rangle$ and $\langle V^2 \rangle$ are:

$$R = k_R \langle R \rangle$$

where R is some kind of non–isophotal radius (*e.g.* the effective radius or the core radius of a King model fit), and k_R is a parameter reflecting the density structure of the galaxy;

$$V^2 = k_V \cdot \langle V^2 \rangle$$

where V is some sort of velocity scale, *e.g.* the maximum rotational velocity in spirals and the central velocity dispersion σ_c in ellipticals, and k_V is a parameter

reflecting the kinematical structure of the galaxy (dispersion tensor anisotropies, relative importance of ordered and random motions...);

$$L = M/\Upsilon = k_L I R^2/\Upsilon$$

where L is the total luminosity and I the mean surface brightness of the galaxy, Υ is the global mass–to–light ratio and k_L is a parameter reflecting the luminosity structure of the galaxy, which in general is not the same as the density structure. While k_R, k_V nd k_L depend on the operational definitions of observables, k_E does not, and represents an intrinsic quality of a galaxy.

By defining the combined structural parameters:

$$K_{SR} = k_E/\left(2Gk_R k_L k_V\right)$$

$$K_{SL} = k_E^2/\left(4G^2 k_R^2 k_L k_V^2\right)$$

we obtain the two *generalized distance indicators relations:*

$$R = K_{SR} V^2 I^{-1} \Upsilon^{-1}$$

$$L = K_{SL} V^4 I^{-1} \Upsilon^{-2}$$

By assuming that $K_{SR}\Upsilon^{-1}$ is a power–law function of R, V, or I alone, the above equations translates into the Fundamental Plane relations $R \propto V^a I^b$ and $L \propto V^c I^d$.

All the constituent parameters of K_{SR}, K_{SL}, and Υ depend on the formative and evolutionary histories of galaxies. The environment can play an important role, in that it affects not only the supply of the galaxy–building material, but also the dynamical structure of the final product (for instance, the velocity anisotropies of ellipticals are likely to be the dynamical fossiles of the past mergers), the primordial Initial Mass Function, which determines the stellar mass–to–light ratio, the ratio of the dark to luminous matter, etc. In particular, the mass–to–light ratio is expected to present large–scale variations in many theories of galaxy formation; the mean surface brightness reflects the star formation history of a galaxy, and thus merger–caused starbursts or gas sweeping; the parameter k_E is directly related to the degree of dissipation during the formation of a galaxy; k_R and k_L depend on the luminosity and mass density structure of a galaxy, and can be modified by mergers and tidal encounters; k_V is affected by the anisotropies of the velocity dispersion tensor and the distribution of kinetic energy between the ordered and chaotic motions. Given all this, it may appear astonishing that the FP exists, as this implies that the compound variations in the parameters K_{RS}, K_{SL} and Υ can not be larger than 20%. Therefore, there must be a remarkable uniformity in the ways of manifacturing galaxies, indicating that some as yet undiscovered regulative mechanisms operate in galaxy formation.

2.5 The $\mu_e - R_e$ relation for early–type galaxies

An alternative and independent version of the Fundamental Plane, based on photometric parameters only, has been recently given by Capaccioli & Caon (1991). Using the homogeneous photometric database relative to a luminosity–limited sample of 33 E and S0 Virgo cluster galaxies ($M_B < -17.3$; CCR), these authors have re-examined the correlation between effective radius R_e and corresponding surface brightness μ_e, found for early–type galaxies by Kormendy (1977). For a sample of 29 elliptical in poor clusters, Kormendy (1980) had found the relation:

$$\mu_e = 3.28 \log[R_e\,(kpc)] + 19.45 \qquad \text{(B–mag arcsec}^{-2}\text{)}$$

with a dispersion $\Delta\mu_e \sim 0.3$ mag. This relation has later been confirmed by several studies and shown to hold also for bulges of S0's and early spirals (Hamabe & Kormendy 1987).

2.5.1 The data

For each galaxy in the Virgo sample, luminosity profiles along the main axes, and ellipticity and position angle profiles were used to build up a two–dimensional model of each galaxy (see CCR for details). These models have been used to compute the total apparent magnitude B_T, the semi–axis a_e and b_e of the effective isophote, and the corresponding surface brightness μ_e. The effective parameters used in this work are conform to the original definition of effective isophote as the one encircling half of the total light L_T, and are not the scale parameters of empirical formulae, such as the $r^{1/4}$ law (Sect. 1.1.1). Since all galaxies are practically at the same distance from the observer, the linear values of the effective radii do not suffer from the random errors which afflict samples made with sparse or distance–unconstrained galaxies. For galaxies flatter than $\langle\varepsilon\rangle = 0.3$, it has been possible to measure the geometry of the spheroidal component alone, by applying the 'bulge–fitting' technique (Sect. 3.1.2). For these objects two sets of geometric and photometric parameters have been computed: the first set refers to the spheroid only, the second set to the whole galaxy (the photometric data are listed in Table 1).

2.5.2 The $(\log R_e, \mu_e)$ plane

Fig. 2.2 shows the representative points in the $(\log R_e, \mu_e)$ plane, grouped in four arbitrary luminosity classes designated by different symbols.

The points are very sparsely distributed, and systematically placed below Kormendy's relation. More importantly, there is not a 'unique' relation between R_e and μ_e, but rather a 'set' of parallel relations for the different luminosity classes. With exception of the 6 brightest objects, the galaxies belonging to the same luminosity class lay along a line with slope very close to 5, which is the slope of the

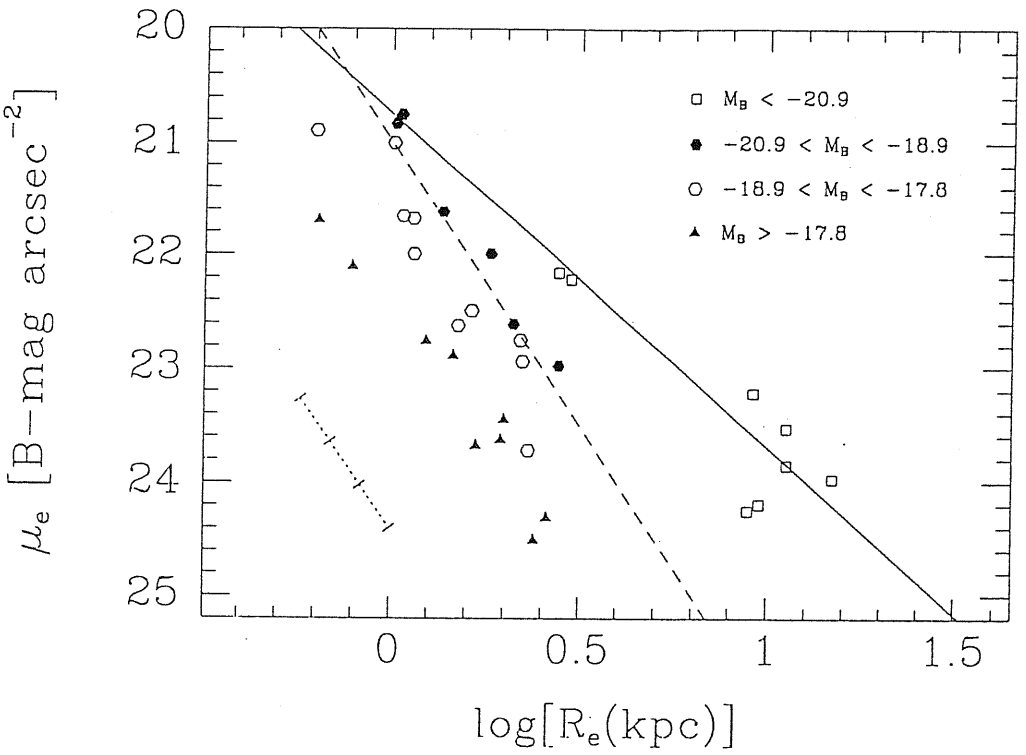

Figure 2.2: Relation between the effective radius R_e (kpc) and the corresponding surface brightness μ_e for a sample of 33 E and S0 galaxies belonging to the Virgo cluster; the adopted distance modulus is 31.3 mag (after Capaccioli *et al.* 1990b). The objects are grouped in four (arbitrary) luminosity classes, designated by different symbols. The solid line is the relation given by Hamabe & Kormendy (1987), scaled to the Virgo distance adopted here and adjusted to the different photometric band assuming $(B-V) = 1.0$. The dotted line represents the shift of a representative point induced by an error δB_T on the total magnitude (see text); the distance between two consecutive ticks corresponds to a $\delta B_T = 0.1$ mag. The locus of the points for galaxies with fixed luminosity L_T and obeying the same scaling law $L_T \propto I_e R_e^2$ is shown as a dashed line.

lines of the scaling law $L_T \propto I_e R_e^2 = \text{const}$ observed by a family of homologous object. Furthermore, there is not patent difference between galaxies classified E and those classified S0, a fact indicating either a physical link between these two classes of objects or the inability of the above relation in discriminating among galaxy types.

The only relevant source of errors on μ_e and $\log R_e$ is the uncertainty δB_T on the computed total magnitude:

$$\delta\mu_e = -3.78\delta B_T$$

$$\delta\mu_e = 4.79\delta \log\ R_e$$

Hence, the error δB_T practically shifts the points along lines of constant luminosity; however, as $\delta B_T \lesssim 0.1$ mag (CCR), its effect is much smaller than the observed variation of μ_e and R_e for each luminosity class. The six brightest galaxies form a distinct group in the $(\log R_e, \mu_e)$ plane, well separated from all the other objects and characterized by a very large effective radius and a faint effective surface brightness. It can not be said whether the empty region between the two groups reflects some physical difference between two distinct populations of early–type galaxies, or, maybe more plausibly, it is peculiar to our sample.

In the M_B–μ_e diagram (Fig. 2.3), galaxies in the same μ_e bin are situated along a line of slope $\simeq 1$, which corresponds to the expected dependence of B_T on μ_e at fixed R_e for a homologous family. It appears also that the intervals in $\mu_e$covered by galaxies with the same luminosity have an amplitude independent of M_B ($\Delta\mu_e \simeq 2.5$ mag); their baricentres instead move towards higher surface brightnesses as the luminosity increases (once more with the exception of the 6 brightest galaxies).

2.5.3 Discussion

The differences between the $(\log R_e, \mu_e)$ diagram constructed with the Virgo cluster galaxies and those previously reported in the literature are probably due to the different composition of the Virgo sample with respect to the others. In fact, in most cases the (μ_e–R_e) relation has been built with samples containing only BCGs and/or intrinsically bright normal ellipticals (for instance, the faintest galaxy in Kormendy's (1977) sample has $M_B = -20.3$). The influence of this bias can be judged by performing a least–square fitting on the more luminous galaxies in the Virgo sample, say galaxies with $M_B \leq -20.0$. For this restricted group the μ_e–R_e relation has a slope $\simeq 2.7$, even smaller than that of Kormendy's relation.

The results of this work rule out the existence of a direct functional dependence of μ_e on just R_e alone, the relation found by Kormendy being merely the upper envelope of a more complex distribution. More importantly, at a fixed luminosity scale parameters vary over a rather broad range, $\Delta\mu_e \simeq 2.5$. This variations can not be due to measurements errors, as said previously, neither to inclination effects

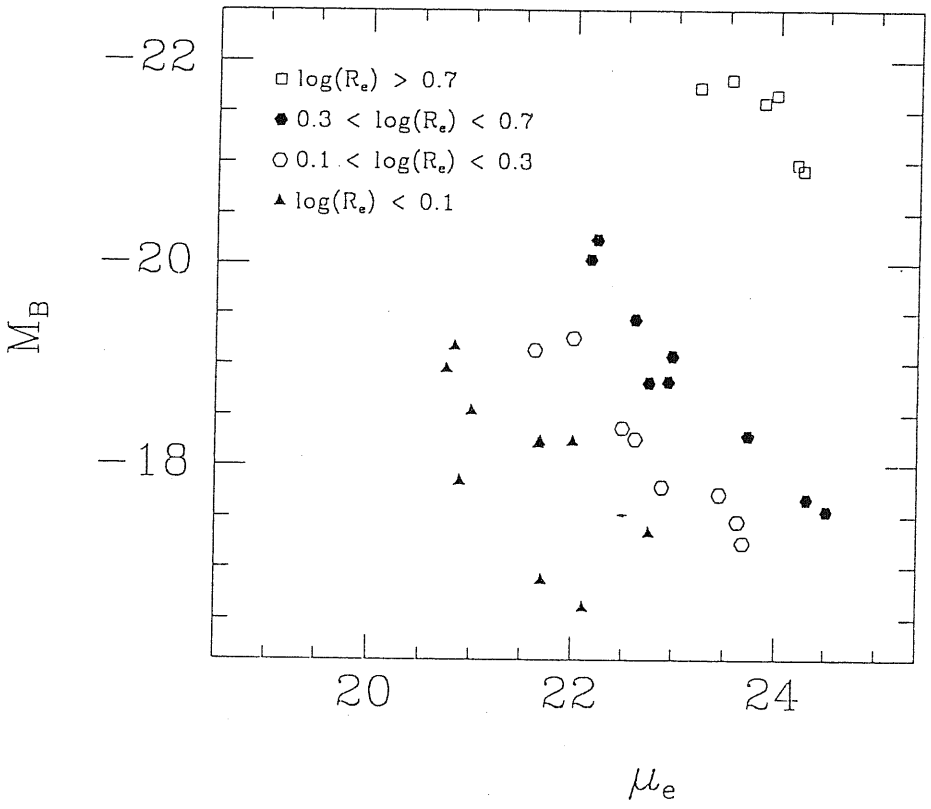

Figure 2.3: Relation between M_B and μ_e. Galaxies are grouped according to the values of log R_e.

only. We expect that, for a group of self–similar galaxies seen under random view angles, μ_e and ε_e (the ellipticity of the effective isophote) are either correlated or anticorrelated according to whether galaxies have either oblate or prolate shapes (see Capaccioli, Fasano & Lake 1984). However, a plot in the plane (ε_e,μ_e) is very noisy and does not show any clear correlation among galaxies pertaining to the same magnitude interval. In any case, the inclination effect can not be so strong to account for the observed spread in μ_e: were it due entirely to inclination effects, it would imply intrinsic axial ratios of ~ 0.1, far too small for E galaxies and S0 bulges (which are at most as flat as $b/a = 0.3$).

Thus, the spread of μ_e and R_e for objects with a same total magnitude is largely an intrinsic property of early–type galaxies. This can explain why intrinsic shape tests for E galaxies based on photometry (Sect. 6.1) fail to provide any definitive answer, even when the dependence of μ_e on total luminosity is accounted for.

The μ_e–R_e relation is fully consistent with the Fundamental Plane of early–type galaxies. A least square fit of the relation:

$$-2.5 \log\, L_T = M_B = \alpha\mu_e + \beta \log R_e + \gamma$$

to the subset not containing the 6 brightest galaxies (their inclusion however does not alter the results) gives $\alpha = 1.05 \pm 0.05$, and $\beta = -5.97 \pm 0.3$. By using the classical Virial theorem: $\sigma^2 \propto M/R$ (see Sect. 2.4), under the assumption that the mean velocity dispersion account for the whole kinetic energy, the following relation can be obtained:

$$L_T \propto I_e^{-0.76} \sigma^{3.44} \Upsilon^{-1.7}$$

which compares quite well with Djorgovski & Davis's (1987) relation

$$L_T \propto \langle SB \rangle^{-0.86} \sigma^{3.45}$$

if the mass–to–light ratio Υ is almost independent of L_T.

TABLE 1: Basic data

Ident.	B_T [mag]	μ_e [mag/arcsec^2]	R_e [arcsec]	ε_e
IC 3468	13.63	24.31	29.3	0.15
IC 3540	14.69	22.11	8.9	0.12
IC 3653	14.43	21.70	7.2	0.12
IC 3773*	13.75	24.51	27.0	0.59
NGC 4168	12.23	22.98	31.3	0.11
NGC 4200*	13.96	22.76	14.0	0.34
NGC 4352*	13.51	22.89	16.5	0.53
NGC 4374	9.71	23.85	126.6	0.03
NGC 4387	13.09	21.66	12.1	0.41
NGC 4406	9.63	23.97	167.5	0.37
NGC 4415	13.58	23.45	22.4	0.09
NGC 4417*	11.87	22.61	23.7	0.55
NGC 4431*	13.86	23.63	22.0	0.39
NGC 4434	13.07	22.00	12.9	0.05
NGC 4436*	14.06	23.68	19.0	0.58
NGC 4452*	13.01	23.72	26.1	0.59
NGC 4458	12.93	22.49	18.4	0.10
NGC 4459	11.26	22.16	31.3	0.20
NGC 4464	13.46	20.89	7.1	0.27
NGC 4473*	11.06	22.22	33.8	0.44
NGC 4474*	12.48	22.94	25.1	0.44
NGC 4476*	13.04	22.62	17.0	0.33
NGC 4478	12.36	20.75	11.9	0.19
NGC 4486	9.48	23.53	126.4	0.16
NGC 4550*	12.77	21.00	11.4	0.59
NGC 4551	13.07	21.68	12.9	0.27
NGC 4552	10.38	24.25	100.6	0.12
NGC 4564*	12.05	22.00	20.6	0.53
NGC 4578*	12.49	22.75	24.8	0.27
NGC 4621*	10.32	24.19	107.8	0.19
NGC 4638*	12.17	21.62	15.4	0.41
NGC 4649	9.56	23.22	103.7	0.22
NGC 4660*	12.14	20.83	11.5	0.35

* Data are for the 'bulge' component only.

Chapter 3

The isophotal properties of elliptical galaxies

3.1 The detection of isophotal patterns

3.1.1 The Fourier isophotal analysis

The Fourier analysis of the isophotes of elliptical galaxies has been introduced only about 12 years ago in papers by Williams & Schwarzschild (1979) and Young *et al.* (1979), and further developed, described and applied to fair samples of early-type galaxies by several authors among whom Djorgovski (1985), Lauer (1985), Jedrzejewski (1987) and Bender & Möllenhoff (1987).

This technique aims at describing the deviations of the real isophotes from the best fitting ellipse through a Fourier series expansion of the intensity residual or of the radial residuals. These two methods can be briefly summarized as follows:

Intensity residual method: Let I_0 and $I_f(E)$ be the (constant) intensity of a given isophote and the intensity at the point identified on the best fitting ellipse by the eccentric anomaly E:

$$I(E) - I_0 = \sum_{k=1}^{N} [A_k \cos(kE) + B_k \, sin(kE)]$$

The A_k and B_k coefficients are normalized by dividing by the local slope of the intensity profile.

Radial residual method: Let r_{isof} be the radial coordinate of the isophote of intensity I_0 and $R_{ell}(E)$ the radial coordinate of the best fitting ellipse:

$$r_{isof}(E) - r_{ell}(E) = \sum_{k=1}^{N} [A_k \cos(kE) + B_k \, sin(kE)]$$

The A_k and B_k coefficients are normalized by dividing by the semi-major axis length.

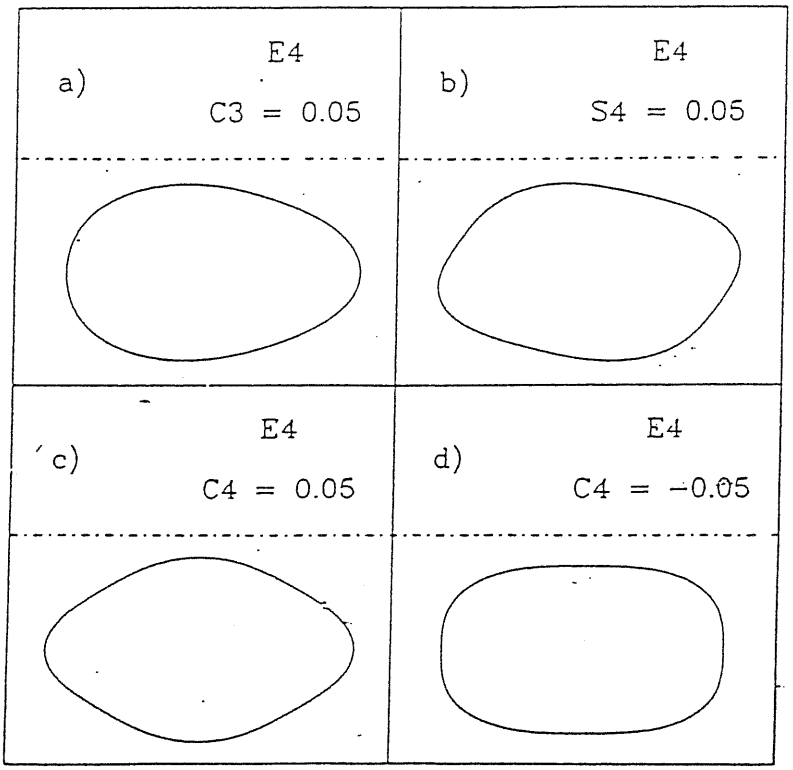

Figure 3.1: Isophotes of model galaxies with non–zero high order Fourier terms. Several E4 model ellipticals are shown with 3θ and 4θ terms with amplitude 0.05 ($5 \div 10$ times higher than typical values for E galaxies) added to the model. The shape in the panel (c) is characteristic of the 'pointed' isophotes, while that in panel (d) correspond to a 'boxy' isophote. Notice that a non–zero $\sin 4\theta$ value produce a 'skewed' isophote. From Peletier *et al.* (1990).

The best fitting ellipsis can be computed through a standard least square fitting (see Capaccioli 1989) or using the same Fourier analysis, the ellipsis parameters being those which makes A_1, A_2, B_1 and B_2 all equal to zero. Of course, since the Fourier orders are all orthogonal, this does not constrain the amplitudes of the higher order terms.

The most important Fourier coefficient has turned out to be A_4. If $A_4 > 0$ the isophote results more "pointed" than the best fitting ellipsis, as if were stretched along the major axes, resembling a lemon (from which the term "lemon–shaped"); if $A_4 < 0$, the isophote is "boxy", looking like an athletics track, consisting of curved ends connected by long 'straigths' (see Fig. 3.1.).

Some objects present other Fourier coefficients which dominate over A_4. Strong odd Fourier terms indicate a generally irregular isophotal shape, the presence of a significant B_4 term points to a disk inclined against the major axis of the bulge or a light excess only along one diagonal of the isophotes (see Bender 1990).

3.1.2 The 'bulge–fitting' technique

A simpler and more direct strategy than the Fourier analysis to parametrize the deviations of the isophotes from pure elliptical shape is the so–called 'bulge fitting' technique (see Capaccioli & Caon 1989, CCR, and references therein).

It is based on the assumptions that early–type galaxies are dominated by a component (bulge) whose isophotes are very closely elliptical. Under favourable inclination and under favourable disk–to–bulge ratio and scale–length ratio (see Sect. 3.1.4 for a detailed discussion of this point), an underlying disk is expected to stretch the isophotes along (or close to) the apparent major axis. Hence, each isophote is interpolated twice, *(a)* using the entire contour, *(b)* removing from the contour that part at the extremes of the major axis which might be influenced by the presence of a hidden disk. If the disk is present, the ellipticity curve $\varepsilon(r)$ given by case *(a)* is expected to stay over that of case *(b)* (see, for instance, the standard S0 NGC 3115 studied with this technique by Capaccioli *et al.* 1987). On the contrary, if the disk is absent or undetectable (unfavorable inclination and/or sub–threshold disk–to–bulge ratio), the two ellipticity curves are expected to coincide or to produce an 'inverse effect' ($\varepsilon(r)$ in *(a)* staying over that in *(b)*) if the isophote is boxy. This method is arbitrary in that it relies on some personal judgment to establish which fraction of an isophote represents the bulge alone; however, as pointed out by CCR, the results are little depending on this fraction, so that this method is rather robust in providing the parameters of the dominating component.

3.1.3 The percentage of disky and boxy ellipticals

The application of the Fourier isophotal description has led to the discovery that about 80% of the galaxies classified as ellipticals show systematic deviations from the perfectly elliptical shape, at the present detection limit ($\sim$ 0.5% of the isophotal diameter), while the remaining 20% posses irregular isophotes. Moreover, in a few cases there is a radial transition from inner pointed to outer boxy isophotes and vice versa.

The percentage of disky and boxy galaxies is not well determined. While from a magnitude limited sample of northern galaxies Bender (1988) find about 1/3 of objects with boxy isophote and an equal amount of pointed ones, Jedrzejewski (1987) report on a higher percentage of pointed objects, 50 %, and only 20% boxy galaxies.

Capaccioli, Caon and Rampazzo (1990) find a percentage of 55% of pointed Es among their sample of elliptical galaxies in the Virgo Cluster, complete to $M_B \sim -17.3$. The authors interprets this finding with the fact fainter E's tend to be pointed (Sect. 3.2), so that a different composition of the samples is likely to be the origin of the discrepancies on the percentages reported in different studies.

3.1.4 The detectability of faint disks in ellipticals

Assuming that, as indicated by several pieces of evidence, pointed ellipticals are composed of a flat disk component superposed on a truly spheroidal bulge, a morphology similar to that of S0's, Rix and White (1990) have studied the 'visibility' of the disk investigating how observables such as the luminosity profile $I(r)$, the ellipticity profile $\varepsilon(r)$ and $A_4(r)$ relate to physical parameters such as the disk–to–spheroid ratio L_D/L_B, disk inclination i, and the ratio of the scale lengths of spheroid and disk r_{exp}/r_{eff}.

They have constructed models composed by an $r^{1/4}$ spheroid with constant ellipticity and an exponential disk, which explore the space of physical parameters, and projected the models into the plane of observable parameters performing the surface photometry on the models.

While there only a weak dependence of A_4 on the scale length ratio r_{exp}/r_{eff} and the bulge flattening, A_4 depends strongly on L_D/L_B and cos i. However, from the $A_4(r)$ profile alone it is not possible to disentangle the effect of the inclination from that of the disk–to–bulge ratio; in other words, keeping all the other parameters fixed, the same $A_4(r)$ profile can be obtained from a faint disk seen at high inclination and from a substantially brighter disk but seen more face–on. This means that ti is incorrect to assume that most observed elliptical galaxies with pointed isophotes have weak, nearly edge–on disks.

Adopting the following criteria for detecting the disk:
1) A_4 greater than 1%, or
2) The rms deviation $\langle \delta I \rangle$ of the major axis profile from an $r^{1/4}$ law is larger than 0.1 mag,
Rix and White (1990) show that for many interesting parameters combinations the disks are practically undetected. For cos $i > 0.6$ there is no detectable A_4 signature in the isophote shapes for any L_D/L_B; deviations from a perfect $r^{1/4}$ law are also difficult to detect for most galaxies with $L_D/L_B < 0.25$ (see Fig. 3.2).

The cos i axis can be regarded as a probability axis, since for random viewing angles, cos i is uniformly distributed between 0 and 1. So, from Fig. 3.2, for random viewing angles and for disk–to–spheroid ratios of less than 1/4, fewer than 50% of disks can be detected by photometric means.

3.2 Correlations between isophotal shapes and global parameters

The isophotal shape of elliptical galaxies is by far more than a simple morphological features. In fact, as first evidenced by Bender *et al.* (1989), there are striking relations between the isophote shapes and global optical, radio and X–ray properties, and kinematic behaviour. We shall limit to concisely describe the main results found by Bender *et al.* (1989), referring to this paper for a complete description

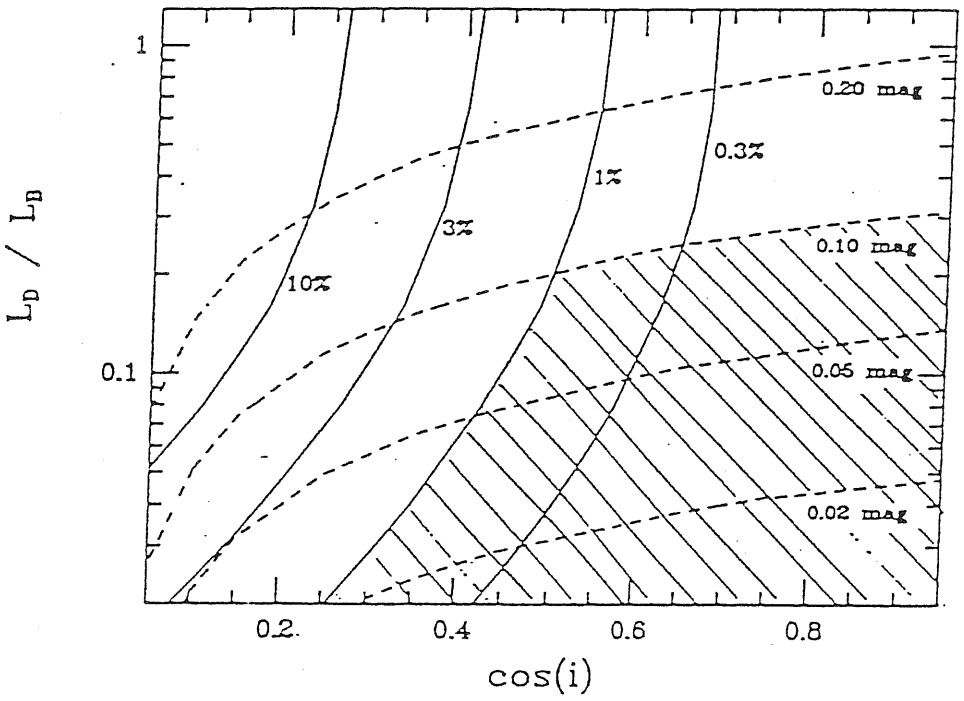

Figure 3.2: Impact of a disk component on the isophote shape and the radial profile in the $(L_D/L_B, \cos i)$ parameter plane. Loci of constant $A_{4,max}$ (solid lines) and constant deviation $\delta I$from an $r^{1/4}$ law (dashed lines) are indicated. The shaded area represents the region of the parameter plane in which disks are undetectable, adopting $A_4 > 1\%$ and $\delta I > 0.1$ mag as detection criteria (see text).

of the sample used (which is essentially a magnitude–limited sample), of how the various parameters into play are defined, and for a more detailed discussion of the results.

Global optical parameters:

- Elliptical galaxies with large effective radii ($R_e \geq 5$ kpc) more frequently show boxy isophotes (Fig. 3.3). Since the correlation is weakened by projection effects influencing the value of A_4, it is likely that the underlying physical relation between isophote shape and effective radius is stronger.

- A similar effect is found plotting A_4 versus the total blue luminosity L_B. Elliptical galaxies having luminosity $\log L_B \geq 11.1$ preferentially exhibit nearly elliptical or boxy isophotes. At the low luminosity end the opposite effect is present.

- Isophotes of round ellipticals show smaller deviations from pure ellipses than the isophotes of flattened ellipticals. This is easily explained by the fact that the probability of detecting weak disks is higher in flattened objects; in a similar way strong boxiness does not appear in round objects, but mostly in those with $0.15 \leq \varepsilon \leq 0.45$. Furthermore, all objects with $\varepsilon \geq 0.3$ shows deviations from perfectly elliptical isophotes, suggesting that, if seen edge–on, all elliptical galaxies show either box–shaped or disk–shaped deviations from pure elliptical isophotes.

- Boxy elliptical are on average rounder (their mean ellipticity is $\varepsilon = 0.25$) than ellipticals with pointed ones ($\varepsilon = 0.33$).

Kinematics:

- Most elliptical galaxies with pointed isophotes are simple oblate rotators with isotropic or nearly isotropic velocity dispersion, resembling the behaviour of S0 galaxies (Fig. 3.4).

- Massive elliptical galaxies showing box–shaped isophotes show a large variety of kinematical behaviour, ranging from almost rotationally flattened rotators to highly anisotropic galaxies. Notice that boxiness in rotating and highly anisotropic systems has different origins, as we shall see in Sect. 3.3.

Radio emission:

- Objects showing pointed isophotes are in general radio–quiet, again similarly to S0 galaxies. In contrast, elliptical galaxies with box–shaped isophotes are frequently radio–loud (Fig. 3.5).

- Radio loud objects predominantly have $\log L_B \geq 10.5$; above this limit, there is a range in luminosity where both radio quiet and radio–loud objects are present; at the highest luminosities $\log L_B \geq 11.$ nearly all galaxies are radio–loud.

- The two–fold dependence of radio emission on absolute luminosity and isophote shape is evidence by the fact that, in the range $10.5 \leq \log L_B \leq 11.0$ where radio–loud and radio–quiet objects are found in equal number, radio–loud galaxies have mostly boxy isophotes, whereas radio–quiet ones are predominantly disky.

- There exists no direct dependence of the radio luminosity on the value of A_4; only the sign is of significance in this context.

X–ray emission:

- There is a strong correlation between isophote shape and X–ray luminosity, after subtraction of the contribution of discrete sources. Halo X–ray emission is nearly confined to galaxies with box–shaped isophotes, while objects with pointed ones show no X–ray emission in excess of the discrete source contribution (Fig. 3.6).

- As in the case of radio–emission, also for X–ray emission there is a two–fold dependence on luminosity and on isophote shapes.

- The strong relation between boxiness/luminosity and radio emission on the one hand, and boxiness/luminosity and X–ray emission on the other is fully consistent with the correlation between radio and X–ray emission in early–type galaxies.

Mass to light ratio

- The mean mass–to–light ratio (computed using the Poveda formula, see Sect. 1.6) of boxy ellipticals is 11.5 ± 0.9, while the mean value of ellipticals with pointed isophotes is 6.4 ± 0.6 (Fig. 3.7).

- From these results, it is expected that the relations between L_X, L_R and M are tighter than those with L_B, as indeed is the case.

- As a consequence, the mass overlap between the radio–quiet and radio–loud galaxies is much smaller than their luminosity overlap.

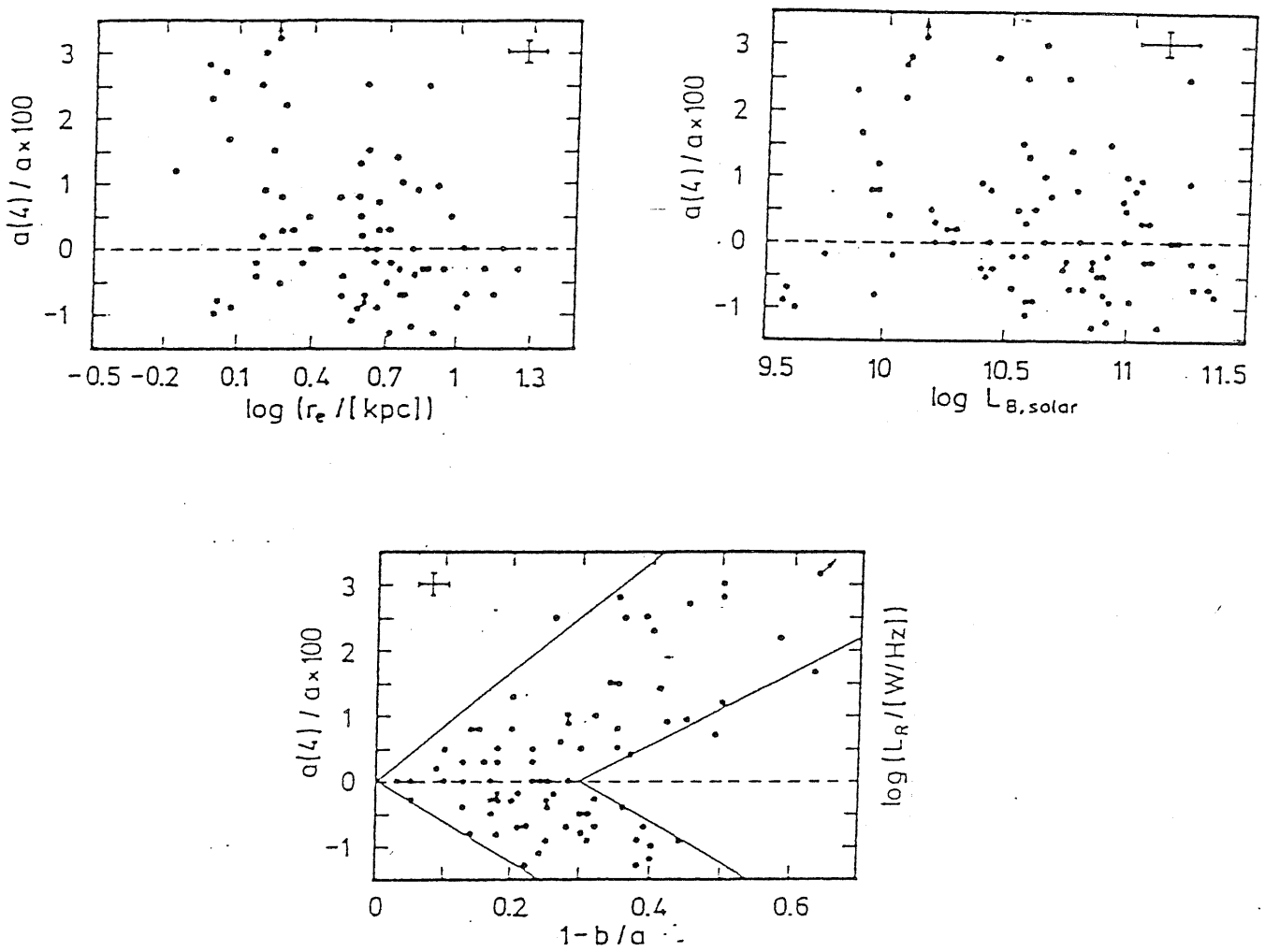

Figure 3.3: The isophote shape parameter A_4 plotted against the effective radii R_e, the blue luminosities L_B, and the ellipticities $\varepsilon = 1 - b/a$ of the sample of Bender *et al.* 1989. The crosses represent the median error on the plotted quantities.

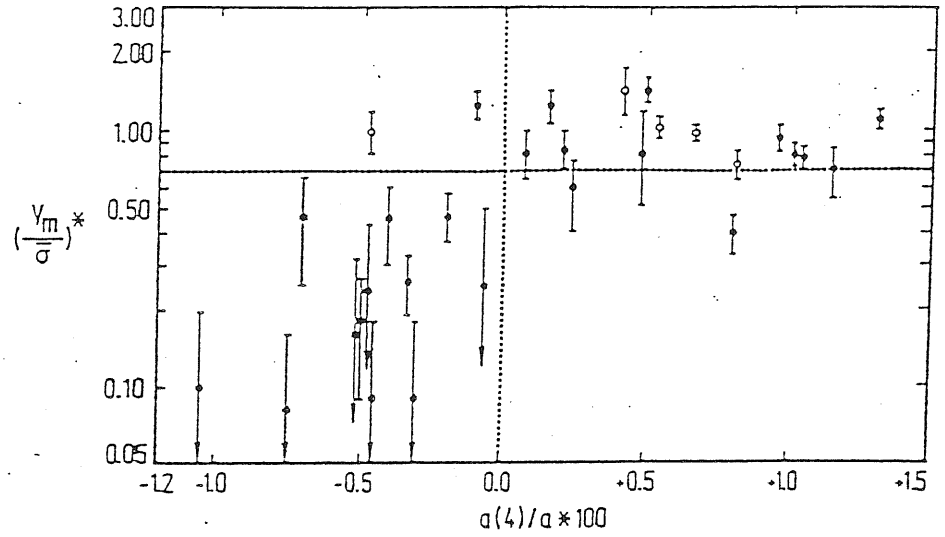

Figure 3.4: The anisotropy parameter $(V/\sigma)^*$ against the Fourier coefficient A_4. Weak ellipticals ($M_B > -20.5$) are denoted by open circles, luminous elliptical ($M_B > -20.5$) by filled circles. From Bender 1988.

3.3 Types of boxiness in elliptical galaxies

As previously reported, boxy ellipticals show a variety of kinematic properties, ranging from rotationally flattened, isotropic galaxies to highly anisotropic objects with nearly no rotation (Bender 1988). This suggest that boxy E's do not form a an homogeneous group.

Nieto & Bender (1989) has identified three kinds of boxiness, corresponding to different subgroups where properties of different types (kinematics, radio emission A_4 profile) strongly correlate.

- **Pure boxiness in massive, anisotropic galaxies:** All galaxies in this class have a A_4 negative throughout, present a remarkable amount of anisotropy, and are the brightest (most massive) objects in the boxy group. The slow rotation indicate that low angular momentum orbits could be responsible for the boxy isophote shape. Some of them present signatures of merging, like shells or misaligned kinematical axes of cores and main bodies. This suggest that merging processes are responsible of the characteristics of this class.

- **Pure boxiness in companion to massive galaxies:** In these galaxies also A_4 is negative throughout. These low luminosity/mass objects have $(V/\sigma)^*$ values $\lesssim 1$, indicating that they are close to rotationally flattened objects. They show no radio emission nor sign of merging signatures; they are closely

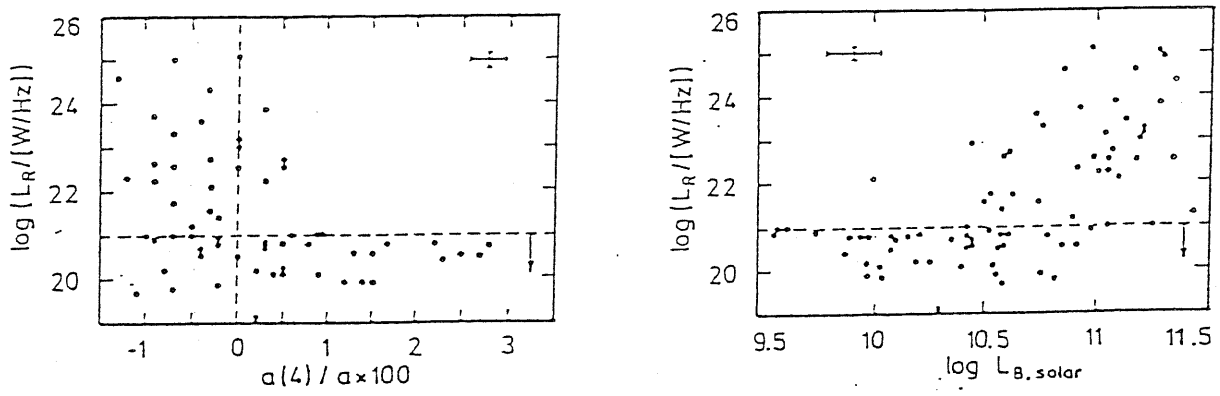

Figure 3.5: The radio luminosity at 1.4 GHz plotted against A_4 and against the blue luminosity L_B. For $L_R \leq 10^{21}$ W/Hz (dashed line) the data points are either detections or upper limits.

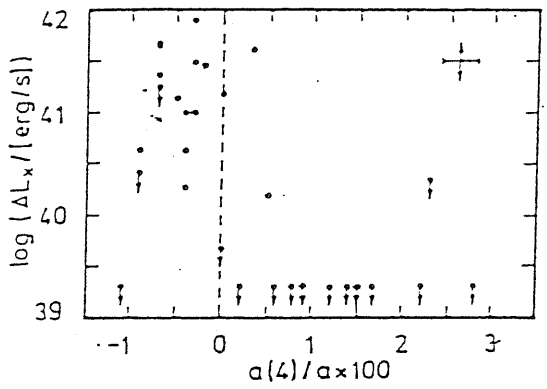

Figure 3.6: The X-ray luminosity ΔL_X obtained by subtracting the contribution due to discrete sources to the total X-ray luminosity, plotted against A_4.

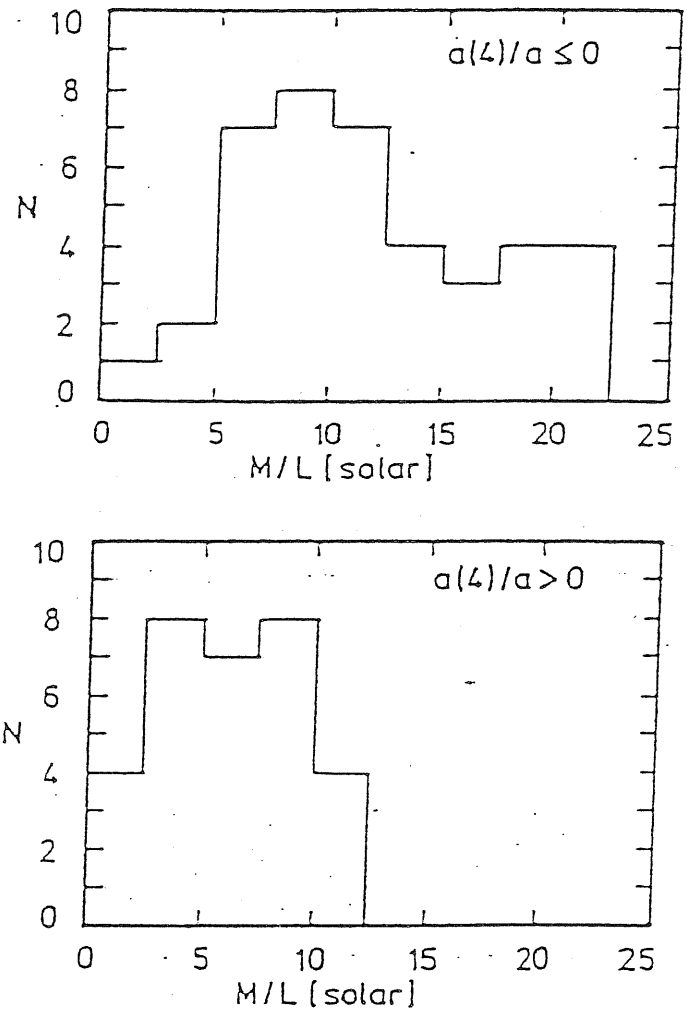

Figure 3.7: Histograms of the blue mass-to-light ratio for galaxies with box-shaped or elliptical isophotes (top) and galaxies with pointed isophotes (bottom).

interacting with more massive objects. These data suggest that objects in this group have once been boxy disk–systems where the faint disk has been stripped or heated by tidal interactions, so that only a boxy bulge is left. An alternative explanation (May *et al.* 1985) attributes boxiness to strong tidal torques of a nearby massive galaxy.

- **E's with weak disks and boxy spheroid:** The fact that E's with weak disks may have a boxy bulge is most obvious in galaxies with inner pointed isophotes and outer boxiness. These objects are rotationally flattened, and their properties (radio activity, X–ray emission etc.) indicate that they belong to the class of disk–E's, except that their bulge is boxy instead of elliptical. The outer boxiness is only visible because the disk vanishes in the outer parts; it is likely that in some disky E's the boxy bulge can not be recognized because the disk dominates the isophotal deviations over the whole range observed. The high rotation and the lack of merging signatures attached to this type of objects tend to play against an origin for boxiness from merging or accretion.

- **E's with inner boxiness and outer pointed isophotes:** Outer disk or any kind of cD–like tidal extension could produce such effects. These galaxies do not form however a homogeneous group, presenting individual peculiar characteristics.

3.4 Isophotal shapes in galaxian cores

The central regions of the galaxies are probably the most interesting and the most rich of information on the formation and evolution of galaxies, but at the same time they are the most difficult to study, due to the limited resolution we can achieve.

Looking at the galaxian cores, insights can be gained into the nature of the supermassive black holes, bursts of star formation, recurrent nuclear activity, violent relaxation, or signatures of merging processes.

3.4.1 Effect of the seeing on central profiles

Since the seeing is the factor that limits our ability to study, both photometrically and spectroscopically, inner regions of galaxies, and indeed it has been the principal reason why only now we are starting understanding the nuclear properties, it is necessary, before going ahead, to study what are the effects of the seeing.

The first to deal with this subject in a quantitative way was Schweizer (1979), who pointed out that the low central surface brightness of giant ellipticals studied by King (1978) is due to the effect of the seeing. Convolving with a realistic PSF an $r^{1/4}$ galaxy model, he was able to reproduce the flat–topped profile of E's. However, the brightest galaxies of the sample appeared resolved, in the sense that

the apparent core radius was larger that that obtained by a seeing–convolved $r^{1/4}$ law. As Schweizer (1979) demonstrated, a King profile (see Sect. 1.1.2) convolved by seeing is still a King profile, but with an apparent core radius $r_{c,app}$ larger than the intrinsic core radius $r_{c,int}$, with obvius relations linking this two quantities with the dispersion $\sigma_\star$ of the PSF. The adoption of the King profiles as representing the central regions of early–type galaxies was motivated both by a lack of any alternative model or scenario, and by the easy derivation of the central mass–to–light ratio M/L (see Sect. 1.6), and of the phase–space density (Carlberg 1986). The only problem was the correct derivation of $r_{c,int}$ from $r_{c,app}$ and $\sigma_\star$.

Non–isothermal cores (i.e. central regions not fitted with a King profile) would thus either reveal a nuclear black hole (see the case of NGC 3379 in de Vaucouleurs & Capaccioli 1979), or indicate the signature of a merger (NGC 1316, see Schweizer 1981).

Using CCD frames obtained in superb seeing conditions at the CFHT ($\sigma_\star \simeq 0.35$ arcsec), Kormendy (1985) compared his seeing corrected core radii with those of Lauer (1985), computed from deconvolutions of CCD images collected in ordinary seeing conditions. He realized that if $r_{c,app}/\sigma_\star < 3$, the seeing correction are to large to give a reliable measure of the intrinsic core radius; only for $r_{c,app}/\sigma_\star > 5$ the seeing correction is modest and $r_{c,int}$ can be accurately derived.

3.4.2 Systematics of cores

Analysing his high–resolution images, Kormendy (1985) showed that, apart from the very brightest E's whose central profiles are well described with King profiles, all elliptical galaxies depart from the King law, and these departures increase as the total luminosity decreases.

Bulges of disk galaxies also show departures from a King profile, rising more steeply toward the center. Anyway, making the assumption that galaxian nuclear regions are described by a King law, Kormendy searched for correlations between core parameters (core radius and central surface brightness) and with total luminosity. He found that the most luminous galaxies have the largest core radii, lowest surface brightness and highest central velocity dispersions (Fig. 3.8).

Also the central M/L ratio (computed according to the isothermal model) turns out to correlate with luminosity. These results would be of paramount importance for the problem of galaxy formation, but the fact that cores are not isothermal means that it is incorrect to assume that the core radius and corresponding surface brightness reflect the physical state of the nuclear regions.

A more thorough study of cores in E and S0 galaxies has been recently performed by Nieto and collaborators (Nieto, Bender & Surma 1991; Nieto *et al.* 1991), aiming at looking for whether the distinction between boxy and disky galaxies manifests also in the core properties. They analysed the CCD images of a sample of 75 early–type galaxies, collected at the CFHT and ESO 2.2m telescopes under good seeing conditions. They classified the shape of the central profile of the galaxies

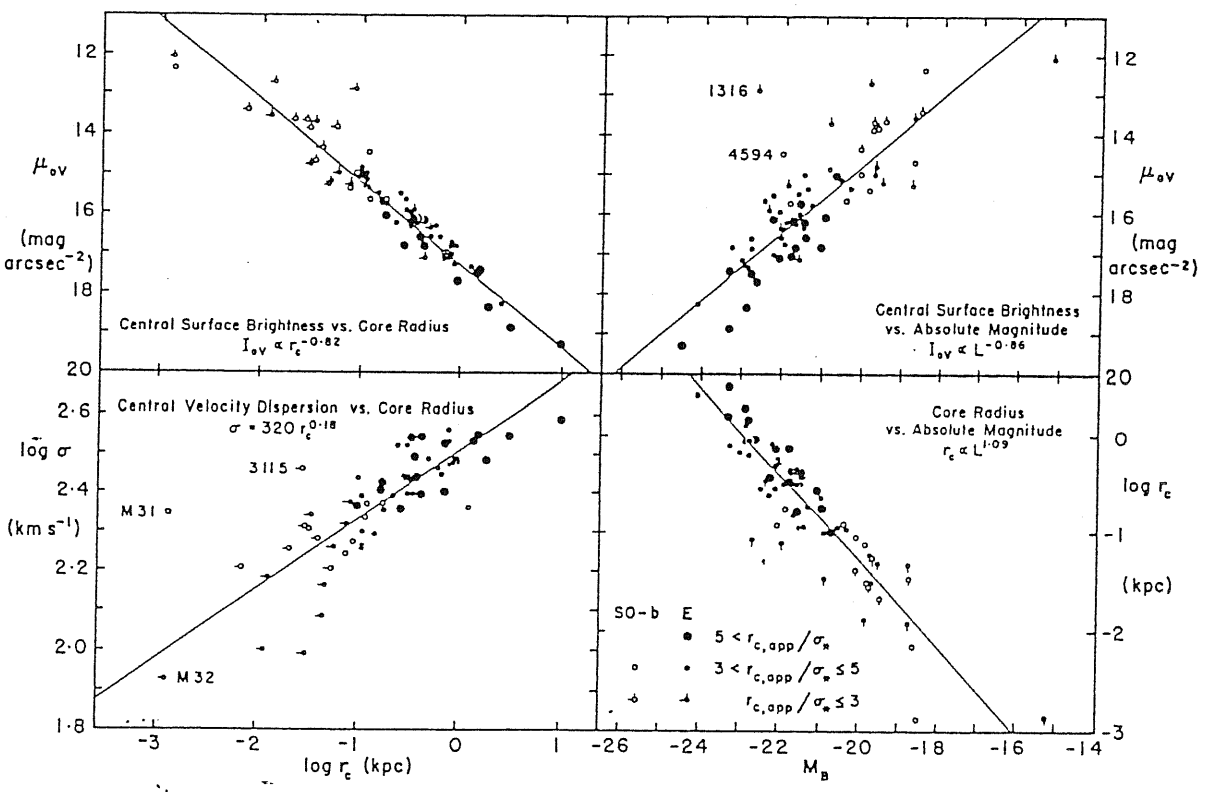

Figure 3.8: The parameter correlations for bulges (open circles) and elliptical galaxies (filled circles). Larger points imply better resolution for the core. The straight lines are least–squares fits. From Kormendy (1987).

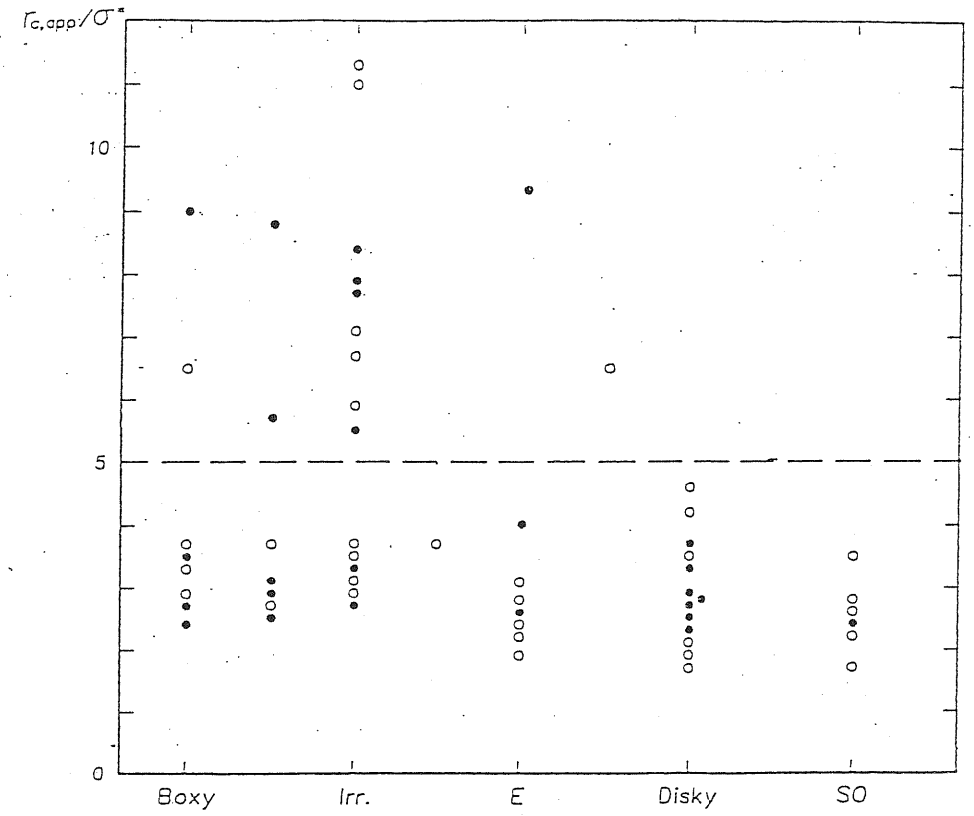

Figure 3.9: The $r_{c,app}/\sigma_*$ values are plotted against isophotal class (boxy, irregular, disky or S0). Solid circles stand for galaxies falling within the common luminosity range of boxy and disky E's.

by the quantity $f = r_{c,app}/\sigma_*$. Galaxies with $f > 5$ are said 'well resolved', while galaxies with $f < 3$ are said 'not resolved'; situations where $3 < f < 5$ are intermediate. The main result is that central characteristics correlate with isophotal shape. In fact:

- Disky ellipticals have peaked central profiles and are unresolved ($f < 5$ for all of them); the same holds for central regions of S0 galaxies
- The only ellipticals having well resolved, flat profiles ($f > 5$) are either boxy or irregular galaxies (Fig. 3.9)
- The central profile shape – isophotal shape correlation is not an artefact of a primary correlation of central shape with luminosity (boxy ellipticals tend to be brighter than disky ones), as it still holds in a restricted magnitude range ($19.4 < -M_B < 21.0$) where boxy and disky galaxies overlap

This leads to two consequences:
1) disky ellipticals and S0 are physically similar also in their nuclear properties, which adds further support to the interpretation of disky ellipticals as the natural

continuation of the sequence of S0 galaxies toward decreasing disk–to–bulge ratios. 2) isophotal shapes must reflect evolutionary and structural differences between two physical families of galaxies. Disk E's, having very small cores, in turn have higher phase space densities, and then must form with higher dissipation than the other E's. So it is likely than disk E's are formed by dissipative collapse, while boxy and irregular are the result of strong merger or accretion processes.

Furthermore, in one third of the sample a kind of 'geometrical decoupling' has been found, in the sense that features in the ellipticity, orientation and the a_4 parameter, correlates with each other, suggest the presence of a separate central entity. In most of these objects, these nuclear components are of disk type, being characterized by a positive a_4 and a higher ellipticity than the main body of the galaxy. The geometrical decoupling appears in $\simeq$ 55% of boxy and irregular galaxies, and in $\simeq$ 28% of disky E's. They are seen essentially in luminous galaxies, but also a few low–luminosity galaxies show such sub–structure. Interestingly, all galaxies with $f > 5$ show either geometrical decoupling or contain dust that prevents a clear analysis; it is therefore expected that a larger number of galaxies will exhibit such separate entities as the resolution increases.

We also notice that kinematically decoupled cores always show geometrical decoupling as well, while the contrary is not true; the reason is that probably photometric sub–entities are easier to detect than kinematic ones. Both phenomena are indicative of a merging or accretion process. Of course, the existence of distinct stellar bodies in the galaxian cores rule out the possibility that they are isothermal systems, so their fitting with a King profile and the derivation of related parameters can not have any physical meaning.

3.5 The classes of elliptical galaxies

Although it is clear that elliptical galaxies do not constitute a homogeneous family, but split into two main distinct physical classes, namely the disky ellipticals and the massive, boxy ellipticals, the cosmological interpretation of this finding is still open. The two classes are likely to reflect a different formation history and different historical pasts in terms of interaction with the environment (Bender *et al.* 1989).

Disky E's, together with S0's and spirals, belong to a continuous sequence in disk–to–bulge ratio, indicating that there is a unique regulating mechanism that controls the final morphology of a protogalaxy. Disky E's can be actually thought of as S0's characterized by a very small disk–to–bulge ratio, which prevents the disk detection by galaxian morphologists and requires sophisticated techniques, such as the Fourier isophotal analysis, in order to recognized the presence of the two distinct components. Thus it may appear incorrect to speak of 'disky E's', as they are nothing but S0; this definition is only related to the fact that such galaxies are classified E in the galaxy catalogs. The same holds for the two subclasses of

boxy galaxies in which a boxy bulge coexist with a stellar disk, or in which a stellar disk has been removed or heated by tidal encounters, leaving a boxy bulge. We know that boxy (and sometimes peanut–shaped) bulges are relatively common in lenticular and spiral galaxies.

In any case, since the frequency of morphological types depends on the density of the environment (Dressler 1980), the discovery of the disky E's is expected to give new insights on the relations among D/B ratio, the environment, and the process of acquiring angular momentum during the primordial collapse phase (see Barnes & Efstathiou 1987). If galaxies form by collisionless collapse of stars, followed by a slow accretion of leftover gas which will eventually settle into a disk, then the morphological sequence can be explained as due to different efficiency in star formation, spirals being the least efficient (Gott & Thuan 1976). Furthermore, the comparison of the disk properties along the D/B sequence is important in order to understand the mechanisms driving the formation of disks; there are suspects that disk properties (exponential decline and same central surface brightness μ_0 for all objects) are independent of the disk–to–bulge ratio (Capaccioli & Vietri 1988).

It is not clear how the theory that all ellipticals are formed by merging of smaller spirals can accomodate both the above continuity and the survival of these small disks to the disruptive events following the merging. It is unlikely that such small disks, such as those found in 50% of E's, can withstand a merging event, when the much larger disks of spirals can not do that. The only way out for the merging hypothesis would be to postulate that disks were formed after the merging event; this is possible provided that accretion of gas onto the parent galaxy is not completely disrupted by the merging itself. The validity of this hypothesis can be checked looking at the colors of the disks, which may provide a lower limit on their age. In fact, were the disk found to be nearly as old as the bulge, a merging event in the past of the elliptical galaxy could be ruled out, as the rate of merging increases steeply with time.

Unlike disky galaxies, whose structure seems to be the product of initial conditions, boxy E's re probably the result of recent violent mergings, even it can not be safely excluded that boxy E's just represent extreme examples of environmental evolution at early phases of galaxy formation. In this respect the analysis of the galaxian interstellar medium is essential for understanding the formation and present day evolution of boxy ellipticals.

3.6 cD and brightest cluster galaxies

The most luminous galaxies in rich cluster are ellipticals; some of them are classified as D, possessing a large and diffuse envelope, or cD, extra–large cD. The importance of brightest cluster members (BCM) is twofold: on one side, they can be used as standard candles for cosmological studies, on the other side thay are the sites of interesting evolutionary phenomena, such as dynamical friction, galactic

cannibalism, interactions with the intracluster medium, etc.

cD are identified by having an extra envelope, which can be recognized as a inflection in their outer luminosity profile. They are always found in local density maxima, even if they are not the brightest or central cluster members; however, cD halos do not occur in poor clusters (Schombert 1986). It is still unclear whether the cD envelope belongs to the galaxy or is formed by the parent cluster, independently of whether there is a galaxy at the bottom of the cluster potential well.

Mergers are the most natural candidate for the formation of cD galaxies, even if other options are possible, such as gradual accumulation of cluster tidal debris (Malumuth & Richstone 1984), or star formation or cooling flows (Sarazin 1986). In particular, the homologous merger picture is the preferred scenario (see White 1982, and references therein). In this picture, the kinetic energy per unit mass is preserved; then, if the orbital structure of the cannibal galaxy stays the same, its projected central velocity dispersion does not change, even though the mass and luminosity increase. This means that the merger product should deviate from the Faber–Jackson relation by being too luminous for its velocity dispersion, as found by Malumuth & Kirshner (1985). It is also expected that more luminous merger remnants have shallower profiles, as confirmed by observations (Hoessel & Schneider 1985), and that they are too blue for their luminosity. The latter prediction is not confirmed, as integrated colors and color gradients in the envelopes of cD galaxies are similar to those of normal ellipticals.

Schombert (1988) performed a systematic study of cD envelopes. By subtracting template profiles of ellipticals from those of cD galaxies, he found that envelope luminosities are comparable to those of the central galaxies, and correlate with parent galaxy luminosity. They also correlate with cluster richness and with the cluster X–ray luminosity. Further connections between cDs and their cluster include alignment effect: in clusters with defined orientation cDs isophote tend to align with cluster major axes (see Djorgovski 1987). Porter (1988) finds that cD tend to have larger ellipticities and ellipticity gradients and smaller isophote twists than normal ellipticals.

All these correlations suggest that cD envelopes are products of their clusters, and are probably the accumulated debris of all tidal interactions: further support to this interpretation is given by the observation that the projected velocity dispersion of cDs increase with radius and approach the cluster velocity dispersion (Dressler 1979).

Chapter 4

Study of Virgo and Fornax galaxies

In this chapter we present new original data concerning the isophotal properties of a complete sample of early–type galaxies belonging to the Virgo and the Fornax Cluster. This must be considered a first account, as a more detailed and thorough analysis will be done as soon as the global photometric analysis of all the galaxy sample is completed.

4.1 The galaxy sample

The Virgo Cluster sample is formed by the 33 E and S0 galaxies studied by CCR, complemented by another 20 galaxies in the Southern part of the Virgo Cluster, for which the derivation of all the relevant photometric and geometrical parameters is in progress (Trevisani 1991).

The Fornax Cluster sample comprises about 30 E and S0 galaxies, selected from the compilation by Ferguson (1989), brighter than $B_T = 15.0$. Complete reduction of the CCD and Schmidt plate material for this sample, and extraction of all the relevant geometrical and photometric parameters is in progress.

From these galaxies, a sample complete down to $M_B = -17.3$ has been formed by selecting all the E and S0 galaxies brighter than $B_T = 14.0$ and $B_T = 13.85$ in Virgo and Fornax respectively, assuming a distance modulus of $\mu = 31.3$ for Virgo (Capaccioli *et al.* 1990b) and of $\mu = 31.15$ for Fornax (Fornax is about 0.15 mag closer than Virgo, according to Bothun, Caldwell & Schombert 1989).

A complete description of the techniques used for the photometric and geometrical study is out of the scope of this chapter. We shall refer to the paper by CCR, and references therein, for a detailed account; here we shall limit to only a coincise description of the main steps involved in the isophotal Fourier analysis (which is described in Sect. 3.1.1)

4.2 Fourier isophotal analysis

The isophotal analysis has been performed on the B–band CCD frames of all the galaxies in the final sample.

After the reduction of CCD frames, following the standard procedures (bias level and dark current removal, flat fielding, etc.), interfering stars and other cosmetic defects have been detected and removed. In the Fourier analysis program, kindly provided by R. Bender, these regions are replaced by their symmetric counterparts with respect to the galaxian center. Every isophote is defined by 128 sample points. The coordinates of the sample points are fixed up to fractions of pixel by linear interpolation. Generally about 75 isophotes per image are analysed, with a 0.1 magnitude step in surface brightness.

The Fourier analysis is carried out on the radial deviations, as described in Sect. 3.1.1. The output consists of the ellipticity, position angle and Fourier coefficients radial profiles.

4.3 Definiton of the characteristic parameters

In order to permit correlation analyses between morphological and non–morphological properties, characteristic parameters were derived for each galaxy:

1. *total B–band magnitude:* for the Virgo sample, they have been taken from CCR, and from Trevisani (1991), while for the Fornax galaxies they are those listed in the compilation by Ferguson (1989).

2. *morphological type:* it is taken from the Virgo Cluster Catalog (Binggeli, Sandage & Tammann 1985) for the Virgo galaxies, from Ferguson (1989) for the Fornax galaxies.

3. *isophotal classification:* five types of isophotal pattern has been recognized:
   1) disky: $\cos 4 > 0.5$ over a significant radial range;
   2) boxy: $\cos 4 < 0.5$ over a significant radial range;
   3) unclassified or irregulars: no disky or boxy pattern is detected, either because the $\cos 4$ term keeps close to 0 everywhere, or because the radial run is too noisy, as happens for the faintest galaxies;
   4) inner boxy, outer disky: $\cos 4$ increases from negative to positive; we shall refer to this class as boxy→disky;
   5) inner disky, outer boxy: $\cos 4$ decreases from positive to negative. No such trend is present in any of our galaxies.

4. *peak value of* $\cos 4$*:* positive or negative; it is defined for boxy or disky galaxies only.

5. *peak value of ellipticity curve:* it has been directly computed from the ellipticity curve, taking care of excluding those regions where ellipticity variations seem to be produced by noise rather than be real.

6. *shape of ellipticity curve:* five types of the radial trend of the ellipticity profiles can be recognized:
   A) flattening monotonically increases with radius;
   B) flattening reaches a maximum at intermediate radii;
   C) flattening is constant or has an irregular behaviour;
   D) flattening decreases with radius;
   E) flattening presents a minimum;

7. *twist angle:* is computed as the maximum excursion in the position angle. Points in the inner 5 arcsec are not considered, as the roundening of isophotes by the seeing and guiding errors may cause spurious position angle variations.

4.4 Results and discussion

Our 64 galaxies form an unbiased and statistically significant sample on which to search for possible correlations among geometrical and photometric parameters. The key point here is the completeness of the present sample, which includes all galaxies belonging to the Fornax Cluster and to the Virgo Cluster brighter than a fixed limiting absolute magnitude; therefore it is not biased toward intrinsically bright objects, as it happens for magnitude–limited samples as the one studied by Bender *et al.* 1989. Furthermore, since galaxies belong to a cluster, the absolute magnitude do not suffer from the (sometime large) random errors which afflicts samples made of sparse and/or distance–unconstrained objects.

We do not consider other global properties such as X–ray emission, radio luminosity, or kinematic properties, as there are not enough data to allow meaningful investigations. Neither it is possible to check whether there are systematic differences among the isophotal properties of the Virgo and of the Fornax galaxies, due to the different environment, because of the too small number (15) of Fornax galaxies retained in the sample.

Fig. 4.1 represents the luminosity functions (LF) of the four groups of galaxies defined by the isophotal shape. We can recognize the following points:

- No disky galaxies populate the brightest magnitude bin, while they are more abundant in the range $M_B = -19.5 \div -17.75$. The disky LF decreases sharply at the low luminosity end; however, part of this could be due to the increased difficulty of detected disky/boxy isophotal signature in faint galaxies with a poor signal–to–noise ratio, for which the radial run of the Fourier coefficients is quite noisy.

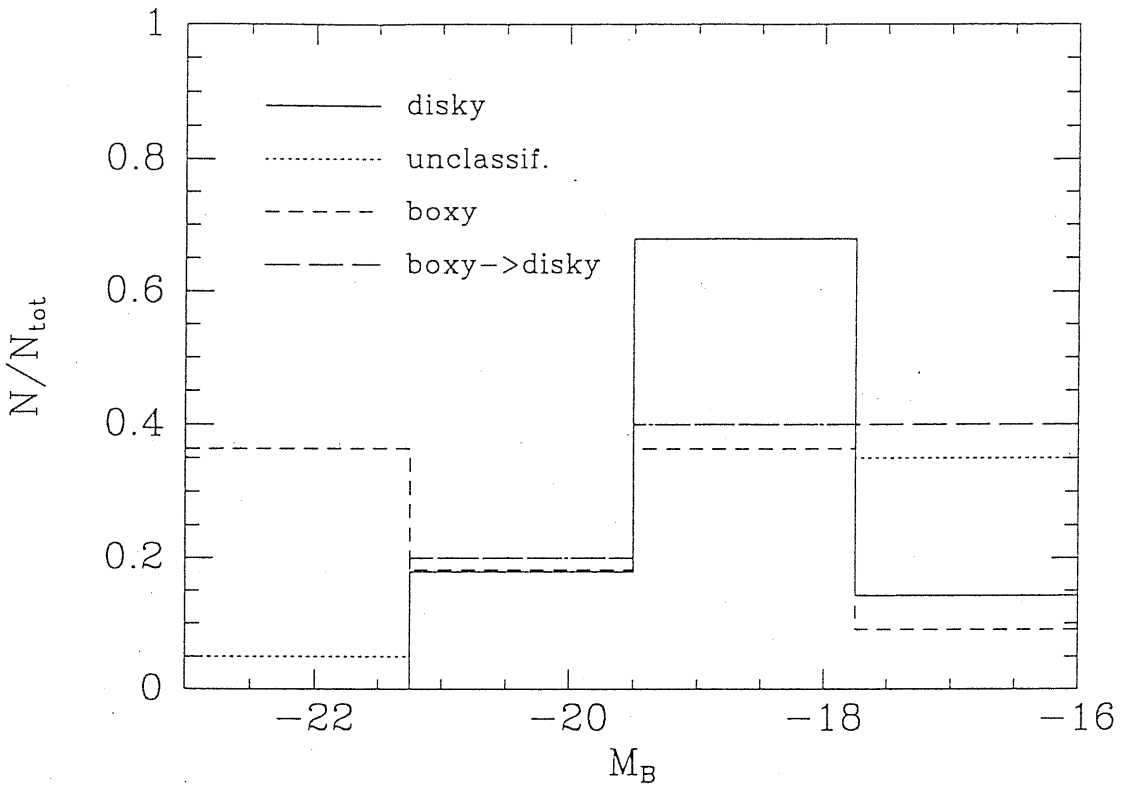

Figure 4.1: The (normalized) Luminosity Functions of the disky, boxy, unclassified and boxy→disky galaxies in our sample. Luminosities have been grouped into four (arbitrary) magnitude bins: $M_B < -21.25$, $-21.25 < M_B < -19.5$, $-19.5 < M_B < -17.75$, $M_B > -17.75$.

- Boxy objects populate mainly the brightest magnitude interval and the range $M_B = -19.5 \div -17.75$, while the decrease at the faint magnitude bin can be due to the same reason as above. However, we must be aware that boxiness has a different physical interpretation for bright and for faint objects, as discusses in Sect. 3.3.

- Galaxies in which isophotes are boxy in the inner region and become pointed outwards are absent among the brightest objects, and their LF is skewed toward the fainter magnitudes.

- The LF of galaxies for which the isophotal pattern can not be classified increases as the magnitude gets fainter; we remark once more on the possibility that this behaviour is due to the impossibility of detecting positive or negative value of the cos 4 term when its radial run is quite noisy.

Fig. 4.2 represents the distribution of galaxies in the four isophotal shape groups (disky, unclassified, boxy, boxy→disky) according to their absolute magnitude. We can see that:

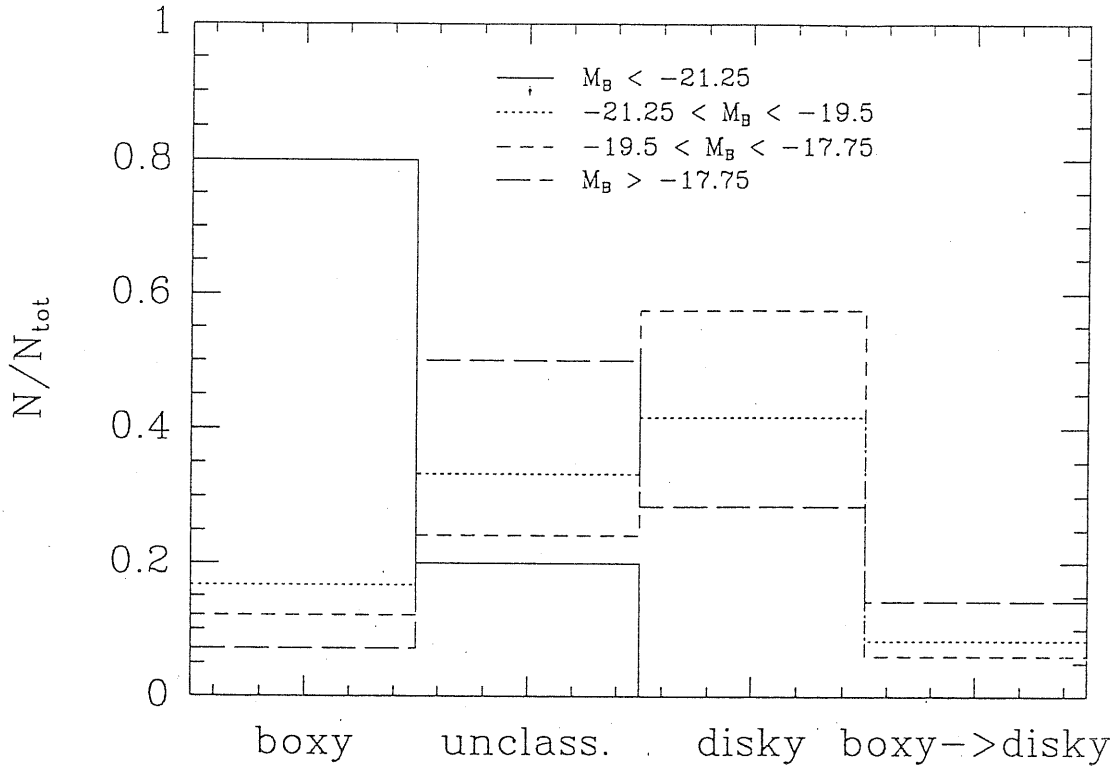

Figure 4.2: The distribution of our galaxies in the four isophotal shape groups according to their absolute luminosity. Galaxies are divided into the same four magnitude intervals as defined in the previous figure.

- Galaxies belonging to the brightest magnitude bin are either boxy or unclassified; none is disky or boxy→disky.
- Galaxies with luminosity within the range $M_B = -21.25 \div -17.75$ are mainly either disky or unclassified. Only few of them are boxy or boxy→disky.
- The faintest galaxies of our group are predominantly unclassified (as already discussed) or disky.

Fig. 4.3 shows the values of the maximum ellipticity as a function of the radial trend of the ellipticity curve, while Fig. 4.4 plots the ellipticity peak value versus the absolute magnitude. We can notice what follows:

- Most of the objects possess an ellipticity curve characterized by a steady increasing whit the radius (type A) or a maximum at intermediate radii (type B). These shapes are not limited to highly flattened objects, but also to nearly round ones.
- Ellipticity curves which are constant or irregular (type C), or decreases (type D) or have a minimum (type E) mostly belong to disky or unclassified galaxies with small flattening.

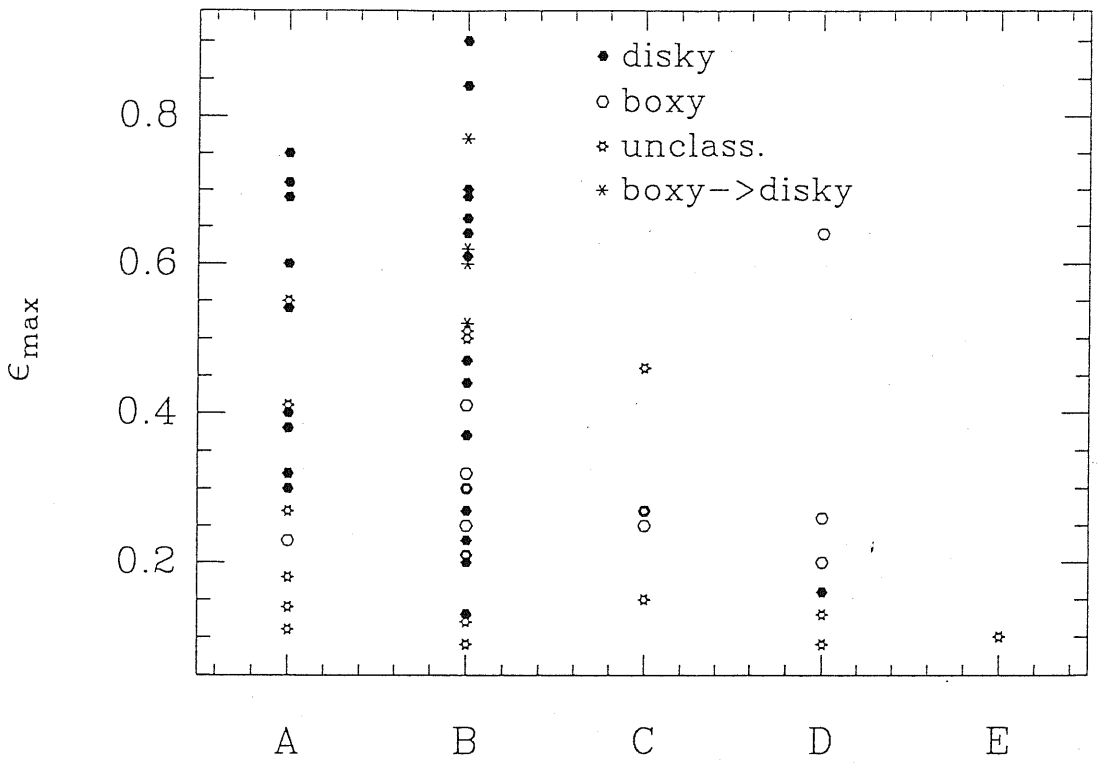

Figure 4.3: The maximum ellipticity as a function of the ellipticity curve shape, coded as follows: A, ellipticity steadily increasing with radius; B, ellipticity presenting a maximum at intermediate radii; C, ellipticity constant or with an irregular behaviour; D, ellipticity decreasing with radius; E, ellipticity with a minimum. Different symbols are used to indicate different isophotal behaviours.

- Only one boxy galaxies and two unclassified galaxies exist with maximum flattening larger than 0.5.
- In the luminosity range $M_B \gtrsim -19.5$, the number of disky objects overwhelms that of the other kinds for $\varepsilon_{max} > 0.4$, while the contrary happens for $\varepsilon_{max} < 0.4$.
- For galaxies with luminosity brighter than $M_B \lesssim -19$, the maximum flattening is a function of the luminosity; actually, there seems to be an upper envelope on the ellipticity distribution. This appears to remain true even considering only the disky galaxies or the boxy + unclassified galaxies. If real, this would suggest that the intrinsic flattening galaxies is an increasing function of the ellipticity.

Fig. 4.5 shows the dependence of the peak value of A_4 on the ellipticity maximum value. There is a correlation between the two quantities, as expected: $(A_4)_{peak}$ increases with ellipticity, and for $\varepsilon_{max} \gtrsim 0.65$ only very high values of A_4 are found.

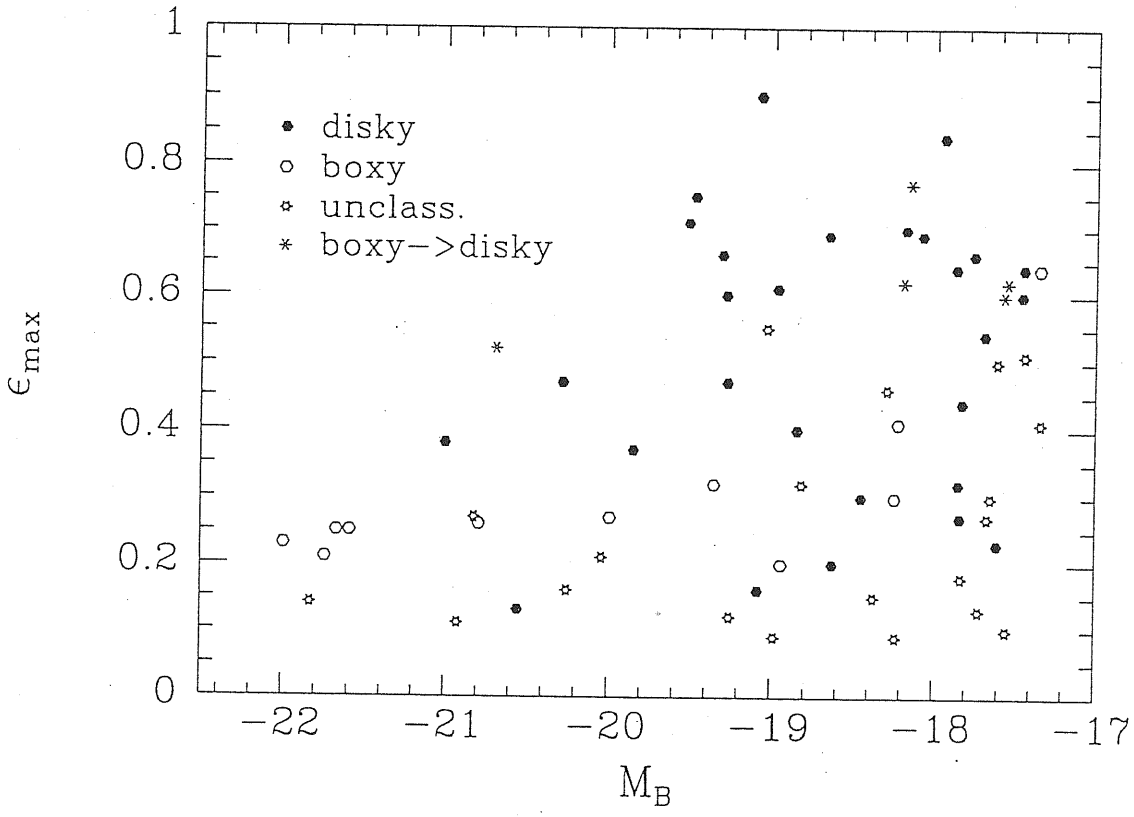

Figure 4.4: The peak value of the ellipticity curve plotted against the absolute magnitude. Different symbols are used for galaxies according to their isophotal classification.

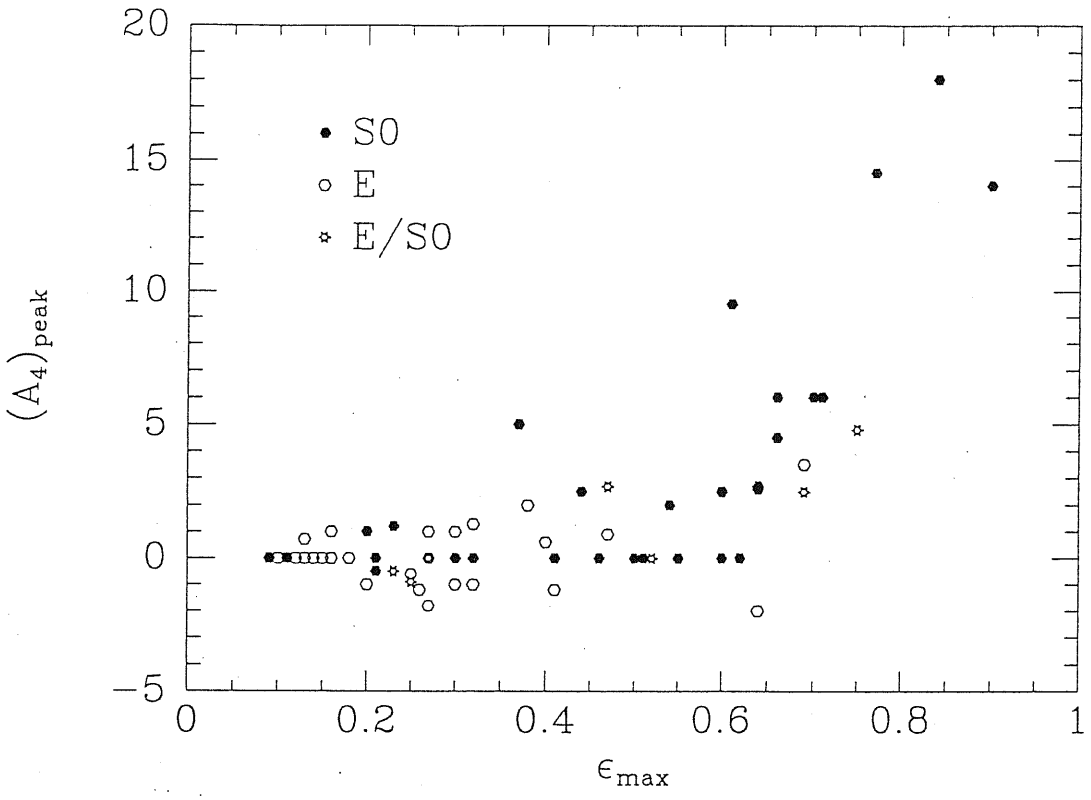

Figure 4.5: The peak value of A_4 plotted versus the maximum value of the ellipticity. For unclassified galaxies an arbitrary value of $(A_4)_{peak} = 0$ has been taken. Objects with the boxy→disky morphology have not been considered.

On the other hand, there are unclassified objects up to $\varepsilon_{max} = 0.55$. This is consistent with what found by Bender *et al.* 1989b, taking into account that they consider a mean ellipticity rather than the peak value.

TABLE 2: Geometrical parameters

Ident.	Morph. type	B_T	isoph. shape	$(A_4)_{peak}$	ε_{max}	ellipt. code	twist	cluster
NGC 4168	E2	12.22	D	1.0	0.16	D	20	V
NGC 4200	S0(4)	13.96	U		0.41	A	4	V
NGC 4215	S0(9)	13.10	D	6.0	0.70	B	2	V1
NGC 4255	S0(6)	13.61	D	2.0	0.54	A	10	V1
NGC 4261	E2	11.31	B	-1.8	0.27	C	15	V1
NGC 4268	S0(6)	13.73	B/D		0.60	B	11	V1
NGC 4269	S0(2)	13.69	D		0.23	B	16	V1
NGC 4270	S0(6)	13.11	B/D		0.62	B	8	V1
NGC 4281	S0(6)	12.27	U		0.55	A	1	V1
NGC 4339	S0(0)	12.32	U		0.09	D	20	V1
NGC 4342	S0(7)	13.54	D	4.5	0.66	B	1	V1
NGC 4352	S0(8)	13.43	D	2.7	0.64	B	4	V
NGC 4360	E2	13.47	U		0.18	A	15	V1
NGC 4365	E3	10.51	B	-1.2	0.26	D	18	V1
NGC 4370	S0(6)	13.69	U		0.50	B	20	V1
NGC 4374	E1	9.71	B	-0.6	0.25	C	30	V
NGC 4377	S0(3)	12.67	D	1.0	0.20	B	25	V1
NGC 4387	E5	13.08	B	-1.2	0.41	B	4	V
NGC 4406	S0(3)/E3	9.63	B	-0.9	0.25	B	15	V
NGC 4415	d:E1,N	13.58	U		0.13	D	10	V
NGC 4417	S0(7)	11.78	D	6.0	0.71	A	2	V
NGC 4431	dS0(5),N	13.86	U		0.51	B	10	V
NGC 4434	E0/S0(0)	13.07	U		0.09	B	25	V
NGC 4452	S0(9)	12.22	D	14.0	0.90	B	2	V
NGC 4458	E1	12.93	U		0.15	C	10	V
NGC 4459	S0(2)	11.26	U		0.21	B	15	V
NGC 4464	E3	13.46	D	1.0	0.27	B	3	V
NGC 4472	E2/S0(2)	9.31	B	-0.5	0.23	A	10	V1
NGC 4473	E5	11.02	D	0.9	0.47	B	1	V
NGC 4474	S0(8)	12.33	D	9.5	0.61	B	2	V
NGC 4476	S0(5)	13.01	U		0.46	C	15	V
NGC 4478	E2	12.36	B	-1.0	0.20	D	16	V
NGC 4486	E0	9.47	U		0.14	A	40	V

TABLE 2: cont.

Ident.	Morph. type	B_T	isoph. shape	$(A_4)_{peak}$	ε_{max}	ellipt. code	twist	cluster
NGC 4526	S0(6)	10.61	B/D		0.52	B	8	V1
NGC 4550	E7/S0(7)	12.64	D	2.5	0.69	A	2	V
NGC 4551	E2	13.06	B	-1.0	0.30	B	7	V
NGC 4552	S0(0)	10.38	U		0.11	A	15	V
NGC 4564	E6	12.02	D	2.5	0.60	A	3	V
NGC 4570	S0(7)/E7	11.82	D	4.8	0.75	A	3	V1
NGC 4578	S0(4)	12.48	U		0.32	A	5	V
NGC 4600	S0(6),N	13.47	D	2.5	0.44	B	30	V1
NGC 4621	E4	10.30	D	2.0	0.38	A	2	V
NGC 4623	E7	13.22	D	3.5	0.69	B	2	V1
NGC 4636	E1/S0(1)	10.48	U		0.27	A	15	V1
NGC 4638	S0(7)	11.99	D	6.0	0.66	B	10	V
NGC 4649	S0(2)	9.56	B	-0.5	0.21	B	20	V
NGC 4660	E3/S0(3)	12.03	D	2.7	0.47	B	6	V
IC 3468	E1,N	13.63	U		0.27	C	15	V
IC 3773	d:S0(9)	13.84	D	2.5	0.60	A	3	V
NGC 1336	E4	13.30	D	1.3	0.32	A	40	F
NGC 1339	E4	12.70	D		0.30	A	4	F
NGC 1351	E5	12.30	D	0.6	0.40	A	3	F
NGC 1374	E0	11.90	U		0.12	B	8	F
NGC 1375	S0(cross)	13.60	B/D		0.62	B	4	F
NGC 1380	S0/a	11.30	D	5.0	0.37	B	3	F
NGC 1380A	$S0_2$(9)(cross)	13.20	D		0.84	B	3	F
NGC 1381	S0(9)(boxy)	13.00	B/D	14.5	0.77	B	1	F
NGC 1399	E0	10.60	D	0.7	0.13	B	18	F
NGC 1404	E2	10.90	U		0.16	D	10	F
NGC 1419	E0	13.60	U		0.10	E	120	F
NGC 1427	E4	11.80	B	-1.0	0.32	B	6	F
NGC 1428	E5(boxy)	13.80	B	-2.0	0.64	D	100	F
FCC 255	$S0_1$(6)N	13.70	D	2.6	0.64	B	4	F
IC 1919	$dS0_{1/2}$(5),N	13.50	U		0.30	B	18	F

Notes to the table:

isoph. shape: D: disky;
B: boxy;
D/B: inner boxy, outer disky;
U: unclassified

ellipt. code: A: ellipticity monotonically increasing with radius;
B: ellipticity reaching a maximum at intermediate radii;
C: ellipticity monotonically decreasing;
D: ellipticity constant or with an irregular radial run;
E: ellipticity reaching a minimum at intermediate radii.

cluster: V: Virgo sample from CCR
V1: Virgo sample from Trevisani (1991)
F: Fornax sample

Chapter 5

Disks in early–type galaxies

5.1 Evidences of disky E's

Several facts, independent of the use of the Fourier isophotal analysis, suggest that a large fraction of ellipticals contain faint disks, and are therefore misclassified S0's galaxies.

Michard (1984) was first to suggest that quite a few E galaxies behave like S0, pointing out the striking similarity of the ellipticity profile of the isophotes of some elongated E's with those of S0's close to edge–on view. Further support came from the occasional discovery of faint disks in otherwise *bona fide* E's, such as NGC 4125 or NGC 4697 (Capaccioli 1987, Carter 1987).

Comparing the distribution of frequencies among the Hubble types of the Southern Galaxy Catalogue (SGC; Corwin, de Vaucouleurs, & de Vaucouleurs 1985), based on deep material, and of the older RC2, it is found that in the former there is a significantly smaller percentage of elliptical galaxies. This can be interpreted as due to the better quality of the material used in the SGC, which has allowed a more reliable morphological classification of E's and S0's.

Van den Bergh (1990a) has inspected the Djorgovski's (1985) and Jedrzejewski's (1987) CCD data in order to see whether the morphological classification as S0 or E manifest on major axis profiles and flattening profiles. He found that the photometric characteristics are only loosely correlated with their E or S0 classifications by galaxy morphologists; in fact:

- galaxies classified S0 in the Shapley–Ames catalog (Sandage & Tammann 1981) fit a de Vaucouleurs law just as frequently as do those classified as ellipticals.

- galaxies whose major axis profile can be fitted by an exponential over more than 2/3 of the radius for which photometry is available are more common among S0 than E; however, there is no one–to–one correspondence between photometric evidence for an exponential disk and the E versus S0 classification

- galaxies with a flattening radial run $\varepsilon(R)$ characterized by a single maximum at intermediate R are almost all classified as ellipticals, while $\varepsilon(R)$ increasing monotonically with R are found in the same percentage in S0 as in E.

- a almost pure sample of E galaxies can be formed by selecting those galaxies which exhibit no exponential disk and whose ellipticity curve has a single maximum; a sample formed by S0's can be obtained selecting only those galaxies that exhibit both an exponential disk and in which $\varepsilon(R)$ keeps increasing with radius.

Further confirmations to the blurring among E and S0 galaxies stem from the examination of the flattening distribution as a function of the luminosity of E and S0 galaxies in the Shapley–Ames catalog (van den Bergh 1990b). In fact, among E's fainter than $M_B = -20.0$ 56% are flattened objects of types E4÷E7, while only 29% of all ellipticals brighter than $M_B = -20.0$ are of types E4÷E7; this suggests that the Shapley–Ames sample of faint Es has been heavily contaminated by disk systems. Vice versa, the flattening distribution of S0 fainter then $M_B = -20.0$ appear significantly skewed toward high values compared to the sample of luminous S0's; this is likely due to the fact that most close–to–face–on faint lenticular galaxies are misclassified as ellipticals.

5.2 Measuring the disk

The concept of photometric decomposition of galaxies into distinct components probably had its origin in Hubble's (1926) classic work on galaxy morphology, where different galaxy types are situated along a sequence of decreasing importance of the central concentration. Baade (1944) showed that this can be considered in terms of the relative importance of two major stellar components (Populations I and II). The first to present a quantitative photometric decomposition was de Vaucouleurs (1959), who described the brightness profile of M32 as the sum of an $r^{1/4}$ spheroid and an exponential disk.

All the decomposition techniques conceived till now are based on more or less unjustified assumptions. For instance, the spheroidal components do not necessarily follow the $r^{1/4}$ law, nor they have constant flattening; near the center, the behaviour of the bulge may be very different from galaxy to galaxy, and there can be additional small features (see Sect. 3.4). Moreover, many bulges show departures from elliptical isophotes (box– and peanut–shaped bulges). As for the disks, many show an inner cutoff (the type II disks of Freeman 1970), others outer cutoffs at few effective radii. The nature of the thick disk as an intermediate component is still a matter of debate (see Wyse and Gilmore 1988). The luminosity profiles or 2–D maps are disturbed by superimposed features, such as dust lanes, lens, bars, rings, which must duly avoided or interpolated across when performing the model fitting.

Most methods to decompose a disk galaxy into its photometric components work well only if the disk–to–bulge ratios are not too small; therefore specific strategies have been conceived to tackle the more difficult problem of disentangling small disks from much brighter bulges as in 'disky' E's.

In the following we shall outline the decomposition methods used to model the galaxy as the sum of two or more components, briefly reporting on their basic assumptions, methodology, input and output data.

de Vaucouleurs (1959) and Kormendy (1977) method.

Assumption: bulge and disk light profiles are idealized by a $r^{1/4}$ and an exponential law respectively:

$$\mu(r)0 = \mu_e + 8.33 \times \left[1 - (r/r_e)^{1/4}\right]$$

$$\mu(r) = \mu_0 + 1.09 \times \alpha r$$

Input data: major axis or equivalent luminosity profile.

Output data: scale parameters for the adopted models, *e.g.* effective surface brightness and radius, μ_e and r_e, for the bulge, and peak brightness and scale–length, μ_0 and α^{-1}, for the disk. They are used to compute bulge and disk total magnitudes and the disk–to–bulge ratios.

Method: iterative. Firstly, the observed surface brightness is plotted against the linear radius to identify by eye, and then fit by a straight line, the range dominated by the exponential disk. The guess of the disk profile is extrapolated to the entire radial range and subtracted from the global light profile. The result is fitted by a $r^{1/4}$ formula which is in turn subtracted from the global profile, and the difference is again fitted by a straight line, and ... The loop is repeated until some convergence criterium is fulfilled. Alternatively — and more objectively — some non-linear fit algorithm is applied to the whole radial domain and solved directly for the bulge and disk parameters. This procedure, firstly devised by van Houten (1961), works well when neither bulge or disk dominate.

Kent (1984) method.

Assumption: bulge and disk each have elliptical isophotes of constant flattening (different for the two components). No *a priori* knowledge of or assumption on the radial run of the surface brightness is required.

Input data: luminosity profiles along both the major and the minor axis, $I_{maj}(r)$ and $I_{min}(r)$, and fixed major–to–minor axis ratios for bulge and disk, f_B and f_D (estimated from the run of the ellipticity with radius).

Output data: light profiles of the bulge and the disk separately, $I_B(r)$ and $I_D(r)$.

Method: using the above notation it is

$$I_{maj}(r) = I_B(r) + I_D(r)$$
$$I_{min}(r) = I_B(f_B \times r) + I_D(f_D \times r) \quad (5.1)$$

Defining the '*observable*' $D(r)$ as

$$D(r) = I_{min}(r) - I_{maj}(f_D \times r) = \quad (5.2)$$

one gets

$$I_B(r) = D(r/f_B) + I_B\Big[(f_D/f_B) \times r\Big] \quad (5.3)$$

Provided $f_D > f_B$, this equation is used to determine iteratively the bulge profile. In the first iteration I_B is set equal to D and substituted into the right-hand side of eqn. 5.3 to compute an improved version of I_B. The process is repeated until convergence is achieved. I_D is then determined using one of eqns. 5.1.

Capaccioli *et al.* (1987) method.

Assumption: the bulge possesses purely elliptical isophotes and the disk is affecting only a narrow strip of the galaxy image about the major axis (i.e., it must be nearly edge–on). No *a priori* knowledge of the dependence on radius of the light profiles of the two components is required.

Input data: two–dimensional (2–D) light distribution of the galaxy.

Output data: 2–D light distributions for disk and bulge separately.

Method: firstly, the flattening profile of the bulge is obtained. Ellipses are fitted to a set of galaxy isophotes cleaned of those parts (about the major axis) judged to be altered by the disk. The geometrical information (ellipticity and twisting) is then coupled to the complete minor–axis light profile — which, except near the center, is assumed to be unaffected by the disk — to build a 2–D photometric model of the bulge. Subtracting this from the original image of the galaxy, the 2–D light distribution of the disk is obtained.

Kodaira *et al.* (1986) method.

Assumption: as in Kormendy's method, bulge and disk profiles are interpolated by the $r^{1/4}$ and exponential formulae.

Input data: the so–called generalized profile and three global parameters, D_{26} (diameter at $\mu_B = 26$ mag arcsec^{-2}), SB (mean surface brightness within the $\mu = 26$ isophote), and $X1(P)$ (mean concentration index; see Kodaira, Watanabe, & Okamura 1983).

Output data: scale parameters of bulge and disk light profiles.

Method: a grid of models with different combinations of the above scale parameters is generated, and for each the 3 global parameters are computed. Then 10 models are selected for which the distance D between model and observed parameters

$$D^2 = \Delta\Big[\log(D_{26}/\sigma_D\Big]^2 + \Big[\Delta SB/\sigma_{SB}\Big]^2 + \Big[\Delta X1(P)/\sigma_X\Big]^2$$

is minimum. Lastly, a search is made among these models to identify that one giving the best fit to the observed generalized profile.

Simien and Michard (1990) method 1.

Assumption: there is a one-to-one correspondence between (a) the deviation of an observed isophote from the best–fitting ellipse, and (b) the local luminosity of the disk, which is assumed to be substantially fainter than the disk.

Input data: the total 2–D light distribution and the disk flattening profile, $q_D(r)$, estimated/guessed from the total flattening profile.

Output data: bulge and disk 2–D light distributions.

Method: the deviations from the best–fitting ellipses, in terms of a difference from their major–axis dimensions, are converted into brightness differences through the gradient of the luminosity profile, and assigned to the disk. A model of the disk is then computed and subtracted from the original image, and the isophote shape analysis is carried out again. The process is iterated, adding up the disk values to those of the preceding steps, until convergence is reached. The residual image gives then the light distribution of the bulge.

Simien and Michard (1990) method 2.

Assumption: bulge isophotes are elliptical. The bulge flattening q_B must be smaller than q_D anywhere.

Input data: major and minor axis light profiles, $I_{maj}(r)$ and $I_{min}(r)$, and the flattening profiles of bulge and disk, $q_B(r)$ and $q_D(r)$, estimated/guessed from the flattening profile of the galaxy isophotes.

Output data: bulge and disk major–axis light profiles, $I_B(r)$ and $I_D(r)$.

Method: it is

$$\begin{aligned} I_{maj}(r) &= I_B(r) + I_D(r) \\ I_{min}\Big[r \times q_B(r)\Big] &= I_B(r) + I_D\Big[u_1(r)\Big] \end{aligned} \quad (5.4)$$

with $u_1(r)$ such that $u_1(r) \times q_D\left[u_1(r)\right] = r \times q_B(r)$. Defining a set of N functions u_i $(i > 1)$ by the relation $u_i(r) = u_1\left[u_i(r)\right]$, it can be shown that:

$$I_B(r) = \sum_{i=1}^{N} \left\{ I_{min}[u_i(r) \times q_D(u_i[r])] - I_{maj}\left[u_i(r)\right] \right\} + \epsilon$$

where $\epsilon = I_B[u_N(r)]$ is a residual which can be neglected when N is large enough. The disk luminosity is then given by the first of eqns. 5.4. Several trials can be made with different runs of $q_D(r)$ and $q_B(r)$ in order to seek the best–fit.

Shaw and Gilmore (1990) method.

Assumption: the bulge has elliptical isophotes and a $r^{1/4}$ light profile. The disk is exponential along the major axis, while the orthogonal cross–sections follow a sech^2 law (*cf.* van der Kruit and Searle 1982).

Input data: 2–D light distribution.

Output data: scale parameters of the components, namely:
1) μ_e, r_e, and $q = b/a$ for the $r^{1/4}$ bulge, and
2) μ_0, α^{-1}, and h_z for the exponential/sech^2 disk.

Method: an iterative non–linear least–squares algorithm is used, which minimizes the sum of the squares of the residuals, or the reduced χ^2, between the observed two–dimensional luminosity distribution of the galaxy and that of the model.

Scorza and Bender (1990) method.

Assumption: bulge isophotes are perfectly elliptical and the disk light profile is exponential.

Input data: the 2–D light distribution.

Output data: scale parameters of the model profile, inclination and center coordinates of the disk, and position angle of the photometric line of nodes.

Method: 2–D exponential disk model are subtracted from the galaxy image, each time exposing the difference to the isophotal shape analysis. The best model is the one producing a residual image (bulge) with perfectly elliptical isophotes (Fourier coefficients nearly null anywhere). In general different parameters influence different Fourier coefficients.

5.3 Two emblematic cases: NGC 3115 and NGC 3379

The 'obvious' general opinion that faint disks can be revealed only when they are seen under a favourable inclination has been clearly put into evidence and justified

in a quantitative way by Capaccioli, Held, & Nieto (1987) and Capaccioli *et al.* (1990a).

These authors, on the bases of a detailed photometric study of the 'standard' S0 galaxy NGC 3115 using both CCD and photographic material, performed the bulge–disk decomposition, deriving the bulge and disk photometric parameters. Reconstructing the luminosity profile the galaxy would have if were seen face–on, they were able to show that the disk (which contributes to only $\simeq 6\%$ of the total light) would escape detection, so that the galaxy would appear as a 'classical' elliptical.

On the other hand, the same authors succeeded in demonstrating that the standard galaxy NGC 3379 actually is a misclassified S0. There already existed some pieces of evidence: the flattening profile is similar to that of edge–on S0's and flat E's; the luminosity profile presents radial modulations mimicking the behaviour of the usual absorption features in close–to–face–on disks, and the trend of the color along the minor axis is similar to that of classical S0 galaxies; the A_4 term is small, < 0.1 but definitely positive. However, there were no real stringent proofs of the presence of a faint disk.

The photometric behaviour profile of the bulge of NGC 3379 has been modelled by the minor–axis profile $\mu_1(b)$ of NGC 3115, adjusted for both the radial scale and the intensity scale factors. The minor–axis profile of NGC 3379 is therefore given by:

$$\mu(b) = -2.5 \log \left[\mathrm{dex}\{-0.4[\mu_1(\rho b) + \Delta\mu]\} + \mathrm{dex}\{-0.4\mu_2(b)\}\right]$$

where

$$\mu_2(b) = \mu_2(0) + (2.5 \log e)\alpha_b b$$

is the classical exponential law, and ρ and $\Delta\mu$ are the scale parameters, computed by fitting the above formula to the actual minor–axis profile of NGC 3379.

Since NGC 3115 is very close to the edge–on view, its very thin disk affects the minor–axis light profile only at very small galactocentric distances. The use of real profile instead of the standard $r^{1/4}$ model is justified by the fact that the light profile of bulges do not follow exactly the $r^{1/4}$ law, being marked by a change of slope which makes the profile shallower outward (Capaccioli 1985) and occurs at about the effective radius (see Capaccioli 1990). This subtle difference with the $r^{1/4}$ law becomes important when trying to disentangle a faint disk from a bright bulge, as is the case of several low disk–to–bulge ratio disk galaxies. The same procedure, applied to the NGC 3379 major axis profile (where the bulge contribution is taken as the bulge minor–axis profile rescaled to the major–axis according to the observed ellipticity curve), allow the derivation of the disk scale length α_a along its major axis (see Fig. 5.1).

The photometric parameters of the exponential disk are robust to variations of the model scale factor, confirming the validity of the procedure. In particular, the central surface brightness is very close to the average value for disks (see van der Kruit 1987).

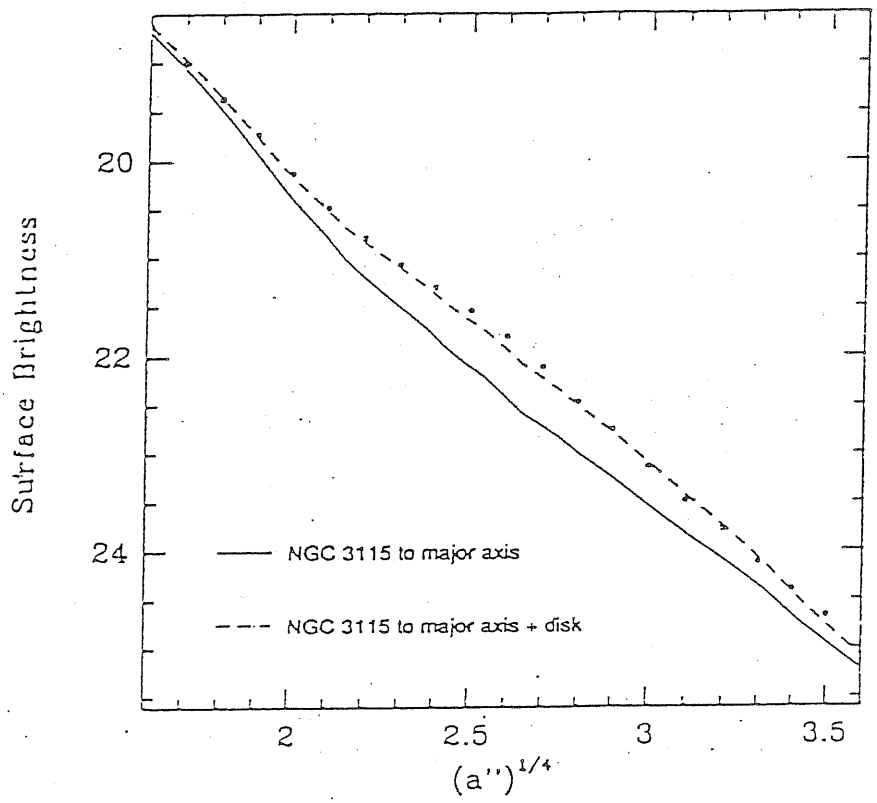

Figure 5.1: The photometric decomposition of the major–axis profile of NGC 3379 (circles) as the sum of a bulge plus an exponential disk.

5.4 Properties of stellar disks in E and S0 galaxies

The investigation of the luminosity profiles of the disks in S0 and disky ellipticals have shown that they can be well described by exponential laws, whit scale lengths varying between 1 and 4 kpc, and central surface brightness values clustering around $\mu_0 = 21.65$ mag arcsec^{-2}, just like disks of spiral galaxies (Capaccioli and Vietri 1989). The practical constancy of μ_0 and of the circular velocity in the host galaxy (which must be the rotational velocity of the cold disk) seem to suggest that the total mass and angular momentum of a disk depend on just one parameter only: the disk's scale length. This fact and the large range in bulge–to–disk ratio values may help constraining the mechanisms with which galaxy components acquire angular momentum (Capaccioli & Vietri 1989).

Still debated is the color of E and S0 disks, which, as metallicity and/or age indicators, are very important for understanding the formation history of galaxies. While most S0 have disks that are bluer than the bulge by 0.1 mag in $U - V$, in NGC 3115 the difference is about 0.5 mag (Silva *et al.* 1989), to be compared with the typical values for Spirals, $0.5 \div 0.75$ mag (Caldwell 1983). This suggests that the disk of NGC 3115 has a a mean age intermediate between the disks of typical S0's and those of Spirals.

As for the thickness of disks, there are controversial results on the trend of the scaleheight with radius. Shaw and Gilmore (1989) find that, in a sample of 10 disky galaxies, the scaleheight h_z turns out to be constant; at variance, Capaccioli *et al.* (1987) present evidences that in the disk of NGC 3115 h_z increase sharply in the inner part, levels off in a intermediate region, and increase again in the outer part (Fig. 5.2).

The question is further confused by the suspected presence, in some S0's, of a third component, the so–called 'thick disk' (Burstein 1979). While a thick disk, that is a disk whose scaleheight is significantly larger than that typical of ordinary disks, $\simeq 200$ pc, has been recognized in a few cases (see Jensen and Thuan 1982), its presence has been ruled out for most of edge–on lenticulars studied so far. In any case, it is not clear whether the thick disk must be considered as a real third component (besides the bulge and the thin disk), or it is merely the response of the bulge to the disk's gravitational field (Freeman 1983).

At least in disky E's the dynamical importance of the disk is negligible, given the very low disk–to–bulge ratio. However, even faint disks can affect the kinematical measurements in a systematic way. When applied to multi–component systems, the methods for measuring rotation and velocity dispersions, such as the Fourier quotient and the Cross Correlation technique, give more weight to the narrow–lined, thus more rapidly rotating component (see, *e.g.*, Whitmore 1980, and Franx & Illingworth 1988). This, in turn, can lead to an overestimate of the ratio v/σ. On the other hand, also the ellipticity measurements are affected by the disks, so

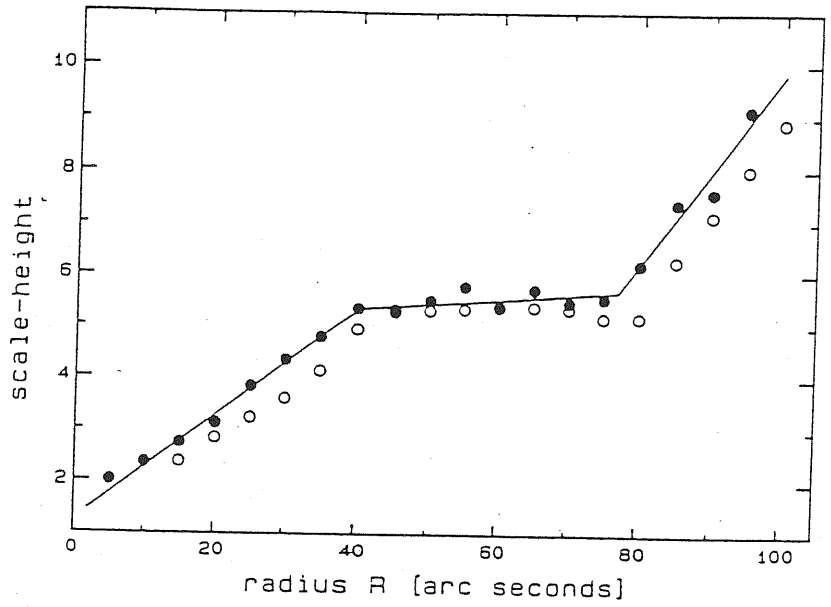

Figure 5.2: The radial run of the scale–height h_z of the disk of NGC 3115. Closed circles are average measurements, open circles are deprojected values. A schematic interpolation is plotted as a solid line.

that an appropriate allowance must be made for these effects (see Sect. 1.3).

5.5 Stellar disks and galaxian properties

Stellar disks can be effectively used as diagnostics of the galaxian structure. For instance the radial trend of the scale–height of the disk of the standard edge–on S0 NGC 3115 has been applied to compute the ratio M/L of the disk itself by Capaccioli, Vietri, and Held (1988). They noted that, by assuming that the flare–up of the disk's scale–height marks the radius at which external gravity begins to dominate over self– gravity, it is possible to compute the disk's M/L ratio, which turned out to be about 7. The fact that the figure applying to a flat component is almost identical to the global M/L within the same radial range of about 5 kpc (or $\sim 1r_e$) was taken as a negative indication of a contribution to the field by a dark halo.

On the other hand, by deep spectroscopy along the major axis of the same galaxy, Cappellaro, Capaccioli, & Held (1990) were able to show that the rotational velocity of the bulge of NGC 3115 remains flat out to $r \sim 2r_e$, a fact implying at least $M/L = 15$ and thus a significant growth in the contribution by Dark Matter.

Chapter 6

Intrinsic shape of elliptical galaxies

The first attempts to investigate the three–dimensional shape of elliptical galaxies have been based on the deprojection of the observed flattening distribution under the assumptions that elliptical galaxies are axisymmetric oblate spheroids, randomly oriented in space (Hubble 1926, Sandage, Freeman, & Stokes 1970). However, the discovery that many ellipticals are supported by the anisotropy of the velocity dispersion tensor rather than by ordered rotation, and the observations of features such as isophotal twist and ellipticity variations, unexplainable by the simple oblate model, opened the possibility that the most general shape of elliptical galaxies is the triaxial one, with oblate and prolate shape as limiting cases. Two lines can be followed to investigate the intrinsic shape of a spheroid. The first makes use of the statistical properties of a large sample: assuming that objects are randomly oriented in space, it follows that certain of the observable properties depend in a predictable way on the intrinsic shape. The second consists in deducing the 3–D shape of a single object by carefully analysing all the photometric and kinematic data, in particular when the presence of subcomponents such as gaseous disks can put strong constraints on the intrinsic shape.

6.1 The statistical analysis

Binney and de Vaucouleurs (1981) performed a statistical analysis of about 200 elliptical galaxies taken from the RC2 catalogue, and pointed out that the RC2 flattening distribution is consistent with both prolate and oblate hypothesis, while for the triaxial shape the consistency with the observed flattening distribution is easily obtained due to the increased number of free parameters.

A similar analysis has been recently carried out on an equally large sample of objects with detailed CCD photometry collected from the literature by Fasano & Vio (1991). These authors found out that the apparent flattening distribution of

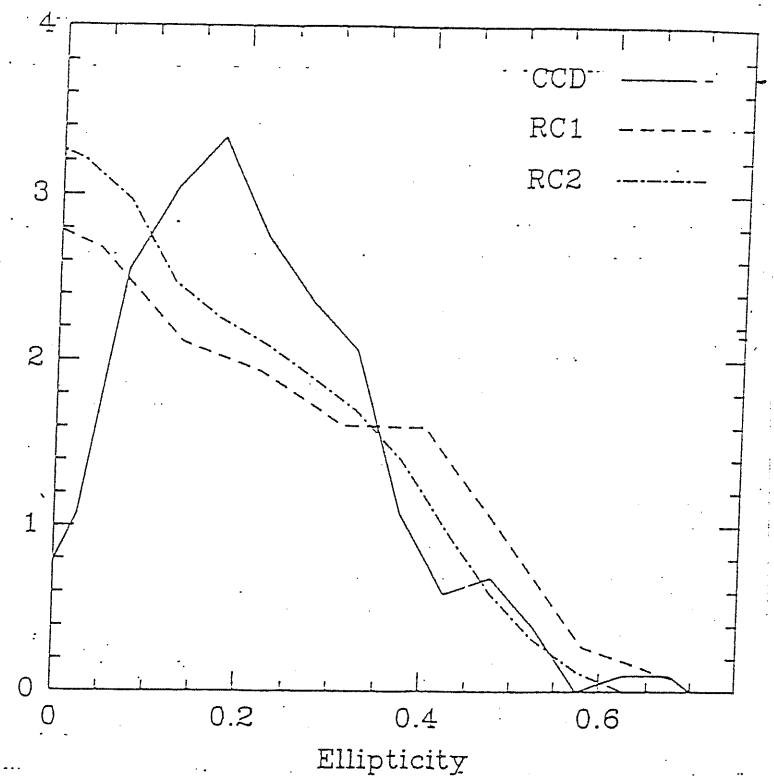

Figure 6.1: The ellipticity distribution of the Fasano & Vio (1991) sample compared with the distributions used by Sandage *et al.* (1970) (from RC1), and by Binney & de Vaucouleurs (1981) (from RC2).

the objects of their sample shows a marked deficiency of round object, compared with the sample of Binney & de Vaucouleurs (Fig. 6.1). This fact renders the flattening distribution incompatible with a purely oblate or prolate galaxy population, suggesting that galaxy must be triaxial, even if the triaxiality can not be too strong, which would give rise to a distribution systematically shifted toward high ellipticities. Moreover, there is a weak hint that the intrinsic distribution is bimodal, so that two different galaxy populations (one whose intrinsic flattening distribution is peaked around 0.55, the other formed by moderately triaxial objects whose c/a flattening distribution is peaked around 0.7) are mixed in the sample.

This result can be easily interpreted in the context of the morphological classification of E galaxies as disky and boxy. Fasano revised and applied some tests on the intrinsic shapes to separately boxy and disky ellipticals of the same sample with detailed CCD photometry. We shall briefly describe these tests; a comprehensive and critical discussion can be found in Merrit (1982) and Fasano (1991).

6.1.1 The MO test

The Marchant and Olson test (1979) looks at the statistical correlation between mean surface brightness within the effective isophote and apparent flattening of spheroid. If such correlation exists, the correlation is expected to be positive or negative in the prolate and oblate configuration respectively. However, an intrinsic correlation between polar surface intensity within the effective isophote and the true axial ratio can exist: $I_e^{(0)} \propto q^{\alpha}$, with $q > 1$ for prolate and $q < 1$ for oblate objects. If most of the scatter in the (I_e, p) plane, where p is the apparent flattening, is due to random orientations, then analysis of the mean slope of the observed relation, combined with the degree of correlation, is capable of determining both the galaxies' intrinsic shape and the dependence of I_e on the intrinsic ellipticities. However, if even a small part of the scatter is due to additional effects, such as measurement errors or to intrinsic variations of I_e among galaxies of equal true flattening and equal luminosity (as discussed in Sect. 2.5), than the test loses much of its power.

6.1.2 The GL test

This test, proposed by Lake (1979), looks at the statistical correlation between central velocity dispersion v_c and apparent flattening. The correlation is expected to be positive or negative in the oblate and prolate configuration respectively. Also in this case an intrinsic correlation between polar velocity dispersion and true axial ratio can exists: $v_c^{(0)} \propto q^{\beta}$ The same considerations made for the (I_e, p) plane apply also to the (v_c, p) plane.

6.1.3 The GF test

The GF test (Fasano 1987) is based on the following properties of elliptical galaxies. Varying the line of sight, any elliptical isophote enclosing a given fraction of the total galaxy luminosity keeps unchanged his degenerate axis (the major or minor depending on whether the galaxy is oblate or prolate respectively), while an isophote corresponding to a given value of the surface brightness does not: depending on whether the galaxy is oblate or prolate, a fixed level isophote becomes larger or smaller respectively as the galaxy projection moves from pole–on to edge–on. The test looks at the statistical correlation between the apparent flattening and the ratio $R = r_\mu / r_e$, where r_μ is the degenerate axis of the isophote at surface brightness $= \mu$, and r_e the same quantity for the effective isophote. This correlation is expected to be positive or negative in the oblate and prolate hypothesis respectively. In analogy with the previous tests, an intrinsic correlation between the polar value of R and true axial ratio may exist: $R \propto q^{\gamma}$.

6.1.4 Results of the statistical analysis

The method used by Fasano (1991) uses the data from the literature to populate the planes (ε, μ_e), $(\varepsilon, \log v_c)$, and $(\varepsilon, \log R)$, ε representing the observed ellipticity, and to compare the resulting distribution with Montecarlo simulations which scan the spaces of parameters $(\alpha, \sigma(\mu_e))$, $(\beta, \sigma(\log v_c)$, and $(\gamma, \sigma(\log R))$, where the σ's take into account the observational scatter.

The results for the sample of boxy ellipticals are contradictory, the oblate and prolate configuration being only marginally consistent. The conclusion is that boxy elliptical are probably moderately triaxial.

In the case of disky ellipticals, the oblate shape is indicated by all the tests, the prolate hypothesis requiring an implausibly strong correlation between R and I_e and intrinsic flattening. Therefore, disky ellipticals are probably oblate, sharing a rather wide interval of intrinsic flattenings.

Furthermore, the two samples of disky and boxy galaxies are statistically disjointed, that is the two samples are not drawn from the same parent population.

In any case, the vagueness of the answers provided by the statistical tests can be attributed to the failure, or at least to the weakness, of the assumptions on which they are based. For instance, the effective surface brightness μ_e covers an interval of about 2.5 mag for spheroids of the same total luminosity and with light profiles all following roughly the same law, as discusses in detail in Sect. 2.5. The spread is mainly intrinsic, as we expect inclination factors to alter the effective surface brightness by at most a factor of 2, with obvious consequences on the reliability of photometric shape tests.

6.2 Intrinsic shape from gas kinematics

Gas disks are valuable tracers of the gravitational potential in elliptical galaxies; the geometrical and kinematic properties of the gas, coupled with the geometrical and photometric data relative to the galaxy, are used to put constraints on the intrinsic shape of the underlying galaxy. We shall describe this method following a very detailed paper by Bertola *et al.* (1991) concerning the elliptical galaxy NGC 5077.

NGC 5077 is an elliptical galaxy with a disk of ionized gas along its minor axis, with the rotation axis displaced by 23 ± 5 degrees from the apparent major axis of the galaxy. The gas velocity field is consistent with circular orbits in a plane, but a fit with a spherical model gives a very implausible run of the mass–to–light M/L ratio, which decreases from 7.5 in the outer regions to 1 or less in the innermost few arcseconds. This is due to the fact, observed also in other elliptical and spiral galaxies, that the gas velocity curve exhibits a very slow rise in the inner part. Also an axisymmetric shape can be ruled out: in this case the gas, if is in an equilibrium configuration, settles on the equatorial plane. Since the gas lie along the minor axis, the galaxy should be prolate, but then the line of zero velocity of the gas

must coincide with the observed major axis of the light distribution. Therefore the only model allowed is the triaxial one.

In a triaxial potential, there are two equilibrium configuration, corresponding to the gas settling on the plane perpendicular to either the major axis or the minor axis. The gas orbits are no longer circular, but become elliptic, with their major axes aligned with the galaxy's shortest axis in the gas plane.

There are four unknowns when observing a triaxial galaxy: the two axial ratios b/a and c/a, the inclination angle θ of the gas disk, assumed to lie on the (x,y)–plane (since it has an elliptical configuration, its apparent flattening can not be used to derive θ), and the azimuthal angles ϕ in the plane of the disk, that is the angle formed in the plane of the gaseous disk by the bulge major axis (if the gas lies in the principal plane orthogonal to the bulge shortest axis) or the bulge minor axis (if the gas lies in the principal plane orthogonal to the bulge longest axis) and the line of nodes.

There are two knowns: the apparent flattening ε of the galaxy, and the angle $\Theta_\star$ between the major axis of the projected surface brightness of the galaxy and the projected z–axis, that is the misalignment angle between the gas rotation axis and the apparent galaxy major axis. As showed by de Zeeuw and Franx (1989), the relations $\Theta_\star = \Theta_\star(b/a, c/a, \theta, \phi)$ and $\varepsilon = \varepsilon(b/a, c/a, \theta, \phi)$ can be inverted to give b/a and c/a explicitly as functions of θ, ϕ, ε and $\Theta_\star$. A further constraint is that $c/a > 0.3$, as no ellipticals are observed flatter than this limit. Moreover, since the gas orbits become nearly circular at large radii, the outer flattening of the gas disk is directly related to the inclination angle θ; however, some uncertainties are introduced by the unknown run of the gas emissivity with radius and by the possible presence of substructure or slight warps in the gaseous disk.

Fig. 6.2 shows all the allowed configurations. It can be seen that both the prolate and the oblate shapes are consistent with the data.

We shall notice that the triaxial model can explain the slowly–rising gas velocity, as the gas orbits are seen broadside, that is the tangential point is observed nearly at the apocenter. In principle, the details of the gas velocity field should further constrain the viewing angles, and hence the range of possible models. However, the quality of the data is not good enough to discriminate between different triaxial models.

In a sample of elliptical galaxies oriented at random, we expect to see some with slowly–rising rotation curves and some with rotation curves which rise faster than predicted by the $r^{1/4}$ model with constant M/L ratio.

6.3 Photometric evidences for triaxial bulges

There are two possible manifestations of a non–axisymmetric structure of the bulges:

1) a misalignment of the isophotal major axes of bulge and disk, as pointed out

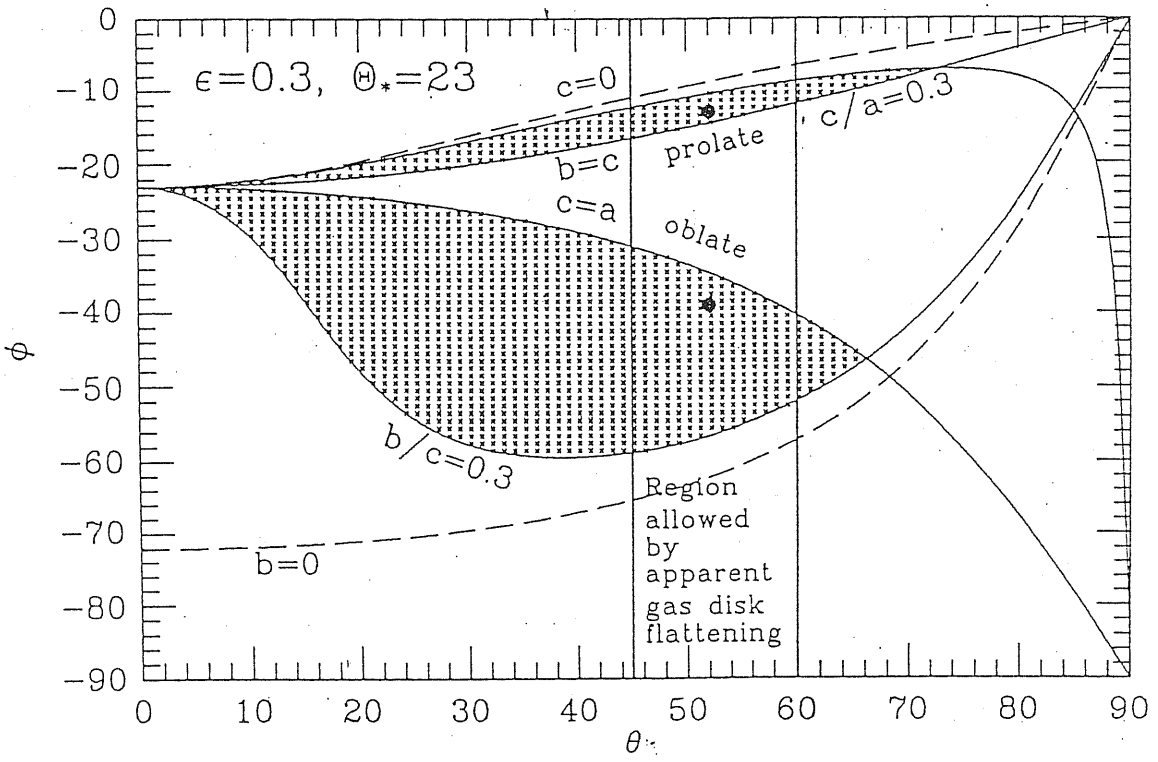

Figure 6.2: Plane of possible viewing angles for the triaxial model of NGC 5077. The hatched areas show the two regions allowed by the observed configuration. The range of θ consistent with the observed flattening of the disk is bounded by the two vertical solid lines.

for the first time by Lindblad (1956) for M31;
2) the presence of non–circular motions in the inner gaseous disk induced by a triaxial potential, as indicated by Gerhard and Vietri (1986).

As the theoretical bases and the various steps involved in studying the triaxiality of bulges by means of kinematic observations are the same as for elliptical galaxies with gaseous disks, here we limit ourselves to the photometric evidences of triaxiality.

Analysing photometrically a sample of 32 non–barred S0 and early spirals, Bertola, Vietri, & Zeilinger (1990) find that in the majority of the objects there are significant differences between bulge and disk major axis, and that bulges often present intrinsic variations of position angle and ellipticity. There is also a tendency for the bulge values to align in the outer regions with those of the disk. These results suggest that a large fraction of bulges are triaxial. The determination of a distribution function of intrinsic axial ratios require the investigation of a much larger sample, with photometric data complemented by kinematic ones.

A different approach has been followed by Capaccioli *et al.* (1991). They postulate, on the basis of the strong similarity in the bulge and disk photometric parameters of NGC 3115 and NGC 3379 (see Sect. 5.3), that the two galaxy have homologous structure, and that NGC 3379 is just a different projection of NGC 3115. This allow to determine the bulge axial ratio under the hypotheses that the intrinsic figure is a triaxial spheroid, and that the minor axis of the bulge and of the disk are coincident, justified by the fact that there are no major disalignments seen in edge–on spirals and S0's. As seen in the previous Section, there are four free parameters in the projection of a triaxial ellipsoid on the plane of the sky: two axial ratios, b/a and c/a, and two Euler angles ϕ and θ, corresponding to the direction in which the true major axis of the ellipsoid points. There are three observational constraints: the apparent axial ratio of the bulge; the inclination angle under which the galaxy is seen, as derived by the disk apparent axial ratio, and the angle γ between the apparent bulge major axis and the lines of nodes (individuated by the disk major axis). Using these three constraints, one can nearly completely deproject the bulge: what is missing is the position angle ϕ of the long axis of the bulge in the plane of the disk, counted clockwise from the line of nodes. In this way, for every value of ϕ, one obtains a unique set of axial ratios appropriated to the observed configuration.

In the assumption that the two galaxies are equal, the correct axial ratios are found at the intersection of the two curves which represents b/a and c/a as function of ϕ, keeping fixed the other observed parameters, for the two objects (Fig. 6.3). As γ varies with radius in both galaxies, two solutions have been actually found, for the inner and the outer regions. The galaxy has a roughly constant c/a ratio, $c/a = 0.5$, while b/a changes from 0.9 in the inner region to 0.75 in the outer one; thus the galaxy is oblate close to the center, and triaxial further out.

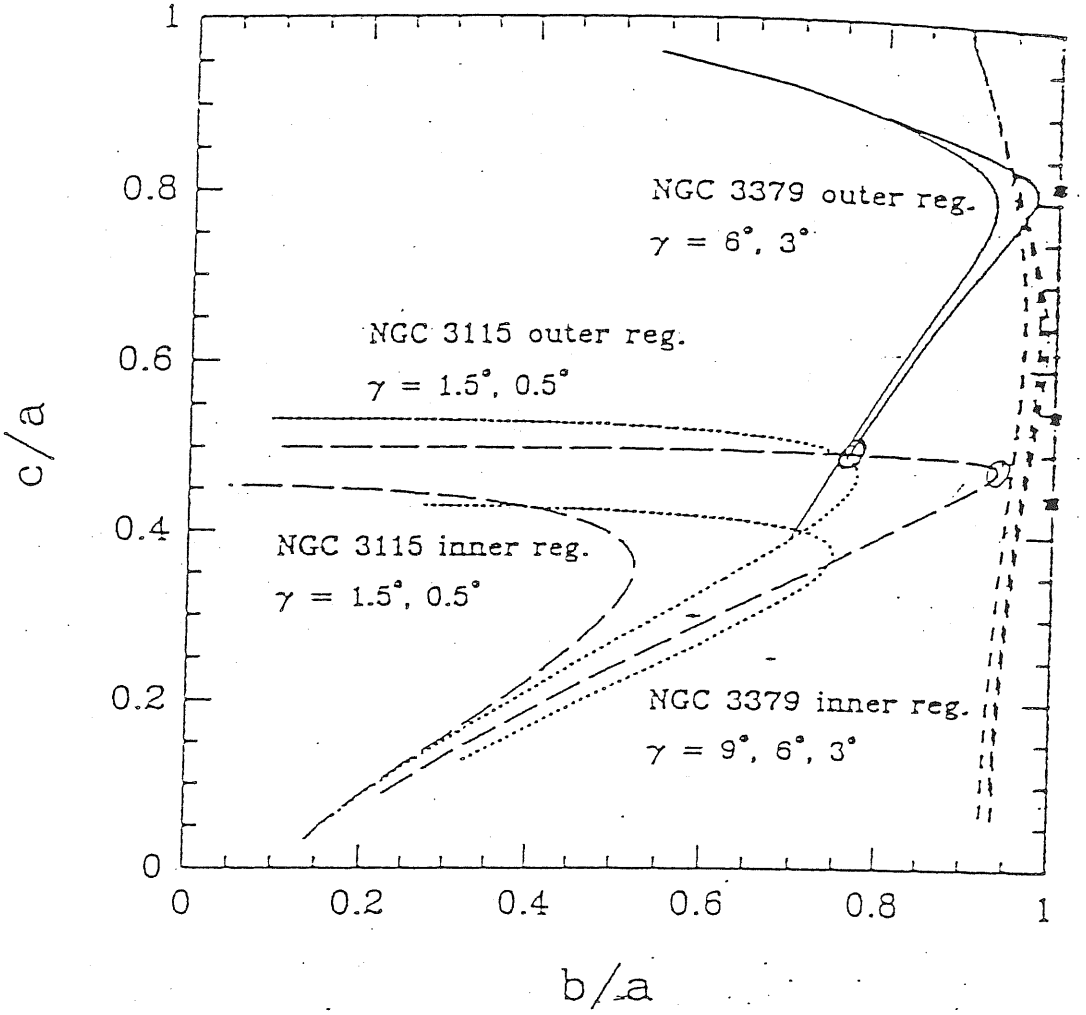

Figure 6.3: Axial ratios from deprojections for NGC 3379 and NGC 3115. Solid lines: solutions for the outer region of NGC 3379, with $\gamma = 6.^\circ 0, 3.^\circ 0$ from left to right; dotted lines: NGC 3115, outer regions, $\gamma = 1.^\circ 5, 0.^\circ 5$, from top to bottom; short dashed lines: NGC 3379, inner regions, $\gamma = 9.^\circ 0, 6.^\circ 0, 3.^\circ 0$ left to right; long dashed lines: NGC 3115, inner regions, $\gamma = 1.^\circ 5, 0.^\circ 5$, top to bottom.

There are a number of theoretical explanations that make this shape change plausible, ranging from the incompleteness of violent relaxation in the outer regions of the galaxy (see White 1987), to the presence of a black hole, or a central cusp in the mass distribution (Gerhard & Binney 1985). It must be noticed it is the triaxiality degree of NGC 3379 and NGC 3115 which increase with radius, not the bulge flattening, as the intrinsic axial ratio c/a keeps constant. Consistently with the small mass and size measured for the disk, this fact rules out any dynamical role that the faint flattened component have in determining the ellipticity of the bulge.

Chapter 7

Components of external origin

7.1 Dust lanes

The discovery of dust lanes in normal ellipticals has undergone a great progress with the advent of CCDs and the use of digital techniques such as the 'unsharp masking'. This consists in dividing the image by a model of the overall brightness distribution without the fine structure; the model can be a smoothed version of the original image, a synthetic image using the best–fitting elliptical isophotes, or an image taken in a redder bandpass. The discovery of a dust lane depends:

1) on one side on the viewing angle: since the dust is usually in well defined, nearly edge–on disks, many face–on dust distributions are going undetected;
2) on the seeing conditions: in fact higher detection rates have been shown by observations at Mauna Kea, and even in such excellent seeing many dust lanes are barely detected; many more may await discovery with the Space Telescope.

Therefore present detection rates are actually lower limits, and can be as high as $40 \div 50\%$ (see the catalog by Ebneter & Balick 1985).

The most convincing evidence that many large–scale dust distributions are accreted from outside is kinematic: dust, as well as the associated cold gas, are usually in disks rotating at random orientations with respect to the optical major axis (see Bertola 1987). Minor–axis dust lanes rotate at right angles to the stars, while about 50% major–axis dust lanes counterrotate with respect to the stellar body (Bertola, Buson, & Zeilinger 1988). Furthermore, at large radii dust–lanes often show S–shaped warps or transitions from regular disks to irregular distributions, as expected for material just settling into equilibrium: since orbital clock run slower at larger radii, the gas settles to a preferred plane at small radii but still remember the merger geometry in the warp. Small dust lanes are more common than large–scale dust distributions, and are usually well defined rings or disks near the center, often oriented parallel to the major axis.

7.2 Shells and ripples

Shell and ripples are faint, arc–shaped structures seen in galactic halos. They are likely to result from the accretion of small galaxies, as suggested by Schweizer (1982, 1983), and confirmed by numerical simulations (see Quinn & Hernquist 1987, Hernquist & Quinn 1987, 1988). Supporting the interpretation that shell are formed by cold material sloshing back and forth in the gravitational potential of the galaxy are the observations that:
1) shells are made of stars similar in color to or slightly bluer than the underlying elliptical
2) shells at successive increasing radii alternate on opposite sides of the center
3) their outer edges are sharp and often edge–brightened, like folded sheets.
These structures form when a small accreted galaxy falls almost radially into a smooth and and stationary potential.

The detection rates of shells in field ellipticals range between 17% (Malin & Carter 1983) and 44% (Schweizer & Ford 1985), and must be considered as lower limits, as not all encounter geometries and viewing angles produce visible shells; this suggests that a typical elliptical has experienced one or more accretion events. Disks galaxies also contain shells, but less often than ellipticals (Schweizer & Seitzer 1988); this is likely due to the fact that the flattened potential of the disk can prevent the cold material from forming ordered shells (Dupraz & Combes 1986).

Shells may give information on the galaxy shapes. Dupraz & Combes (1986) suggest that:
1) when shells are short arcs bisected by the major axis, the elliptical is likely to be prolate and edge–on
2) when shells align with the minor axis, the elliptical is oblate and edge–on
3) when the shell are randomly distributed in azimuth and the galaxy is nearly round, it is likely to be oblate and face–on.

7.3 Polar rings

In a 'polar ring' configuration, the material is located in a plane perpendicular to the disk. It is a ring of (ionised) gas, dust, and blue stars (indicating active star formations). In S0's, rings are generally rotating in a plane perpendicular to the rotation plane of the stars in the S0, and the geometrical centers of the ring and of the main body coincide very well, so that there are two disks, one gaseous, one stellar, orbiting at nearly right angles (Whitmore, Mc Elroy, & Schweizer 1987a). Polar rings do not only appear in S0's, but also in elliptical galaxies, as is the case of AM2020–5050 (Whitmore, Mc Elroy, & Schweizer 1987b): its photometric profile follows quite well an $r^{1/4}$ law, and it is dominated by random motions ($V/\sigma \simeq 0.4$).

Polar rings are difficult to understand in terms of the collapse of a single galactic cloud. As in the case of E's with dust and gas kinematically uncorrelated with the stars, an acquisition of material from outside is the most likely origin of the polar ring. It can be produced by the transfer of mass from a companion galaxy or be the result of the merging of the host galaxy with a gas–rich companion (Schweizer 1987).

Chapter 8

Interstellar medium in elliptical galaxies

8.1 Ionized gas in elliptical galaxies

Investigation on the presence and amount of ionized gas in early–type galaxies, measured through gas emission lines, has revealed that about 55% ÷ 60% of all normal E and S0 galaxies contain a significant amount of ionized gas, down to an equivalent width of $\geq$ 0.5 Å(Phillips *et al.* 1986). Usually, either [NII]λ6584 or $H\alpha$ lines are used in searching for ionized gas, the former being preferred because it is the strongest line on average in the red spectral region (see following section), and because it is unaffected by the strong absorption that underlies $H\alpha$. Detection rates coming from survey of [OII] emission (Caldwell 1984) are consistent with the values quoted above.

In this section we will deal with global properties of the ionized gas and correlation with other quantities; the use of the ionized gas for tracing the galaxy potential and the galaxy intrinsic shape is described in Sect. 6.2.

8.1.1 LINER–like galaxies

Most of the galaxies in which ionized gas has been detected present relatively broad emission lines (200 ÷ 600 km s^{-1} FWHM), with [NII]λ6584/$H\alpha$ $\gtrsim$ 1, and $H\alpha$ luminosities in the range $5\,10^{38} \div 5\,10^{40}$ erg s^{-1}. The same type of spectrum is often found in early spirals, but is much less common in late spirals. In the galaxies with the largest [NII]λ6584 equivalent widths, the [SII] $\lambda\lambda$6716, 6731 lines are visible, and in a good fraction also [OII]λ6300 can be distinguished. In general, the overall characteristics of the emission line spectrum are very similar from galaxy to galaxy, suggesting that the same basic ionization and excitation mechanism is at work in all of the galaxies. In particular, spectra closely resemble those of LINER (Low Ionization Nuclear Emission–line Region) galaxies, a class defined by Heckman (1980) and characterized by:

- Spectra are dominated by lines arising from low ionization states; forbidden lines are moderately strong relative to the permitted recombination lines
- emission line luminosities are modest, with $L_{H\alpha}$ in the range $10^{38} \div 10^{40}$ erg s^{-1}
- emission line widths are comparable to those in the Narrow Line Regions in Seyfert galaxies, with FWHM ranging between 200 and 1000 km s^{-1}

The emission line luminosity correlates with the absolute luminosity, while there seems to be no correlation with global galaxy color, nor with the presence of shells or ripples. Also the ratio [NII]λ6584/$H\alpha$ correlates with total luminosity, getting higher as the galaxy gets brighter: this would reflect abundance differences of the ionized gas or possible variations in the gas excitation, as happens in spiral galaxy nuclei. In the former case, this would provide further independent evidence for the correlation between color (metallicity) and total luminosity.

As for the correlation with other global properties, it turns out that radio galaxies are more likely to have emission lines than non–radio galaxies of the same stellar luminosity. Correlation between presence of dust and ionized gas has been found: while Caldwell (1984) shows that elliptical with dust almost always have ionized gas but there are many with ionized gas and no dust, Bettoni and Buson (1987) found that occurrence of dust features in galaxies with ionized gas is higher than in other galaxies.

There is no correlation with far infrared emission or with UV luminosity, neither with the dust content, even if Caldwell found that $H\alpha$ luminosity correlates with the gaseous X–ray emission, as measured by the L_X/L_B ratio: galaxies with a larger hot gas content have on average a stronger line emission, but the scatter is larger than observational errors, which could indicate that there is not a direct dependence of the line emitting warm gas on the very hot one. An interesting result is that high $L_{H\alpha}$ is found only in 'boxy' galaxies (Trinchieri & di Serego 1991; see Fig. 8.1). This suggest that the shape and/or the depth of the gravitational potential are important parameters for determining the characteristics of the interstellar medium in early–type galaxies.

Lastly, it has been discovered that the percentage of emission lines galaxies in cluster is over 4 times less than the value observed in the field (Bettoni & Buson 1987).

8.1.2 Mass and spatial distribution of the ionized gas

Line emission in most cases peaks on the galaxy nucleus, and is in general more concentrated and has a steeper radial gradient than the continuum light; this could be an indication that the gas tends to fall in the potential well of the galaxy (Trinchieri & di Serego 1991). It is generally extended on scales of several kpc, and its morphology is to first approximation similar to that of the continuum light:

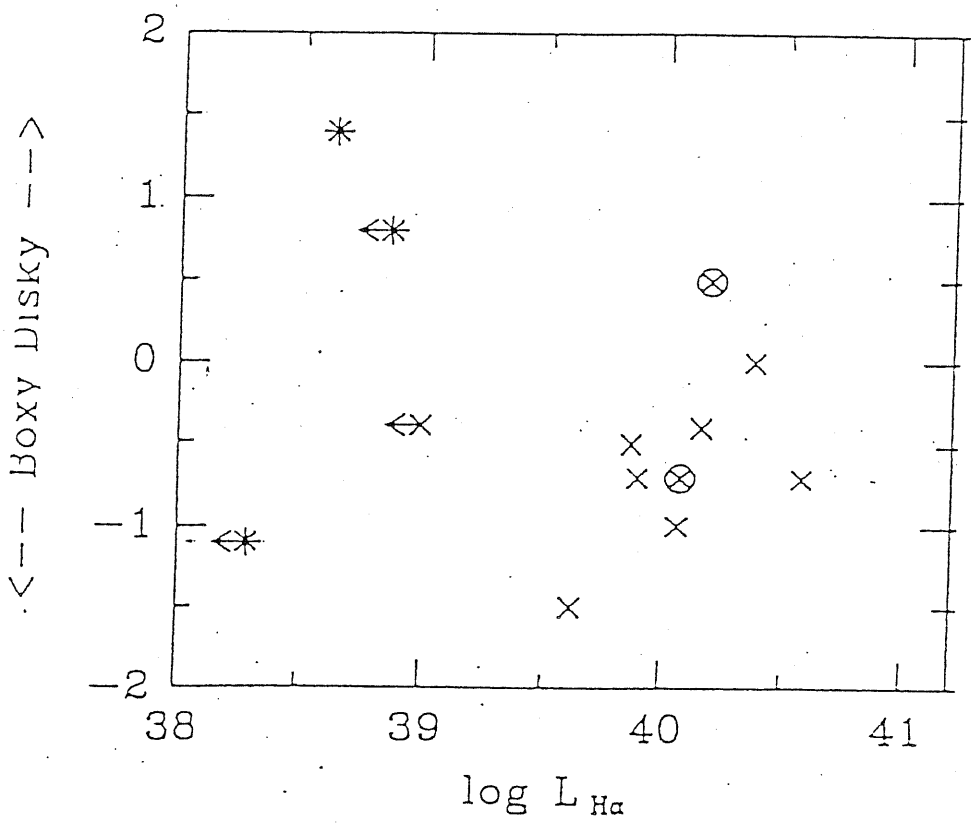

Figure 8.1: Boxyness parameter versus $H\alpha$ luminosity for the galaxies in the sample of Trinchieri & di Serego (1991) (crosses and asterisks) and from the literature (circled symbols).

inner isophotes are fairly regular and are oriented along with the continuum. In a few objects some irregularities, such as filaments and other substructures are present.

The ionized gas mass can be measured essentially in two ways:

1. From simple theory of recombination spectra: the mass is given by the formula

$$M_{\text{ionized gas}} = (L_{H\alpha} m_H / N_e)/(4\pi j_{H\alpha}/N_e N_p) \tag{8.1}$$

where $j_{H\alpha}$ is the emissivity of $H\alpha$, and the meaning of the other symbols is obvious. Since the term within the second couple of parentheses is nearly insensitive to changes in N_e in the range $10^2 \div 10^6$ cm^{-3}, and to temperature changes in the range $10000 \div 20000$ K, the mass is given mainly by $L_{H\alpha}$ and N_e. Assuming $N_e = 10^3$ cm^{-3} and $T = 10^4$ K, the resulting mean value of the warm gas mass lies between 10^3 and 10^4 $M_\odot$.

2. From X–ray data, in the assumption that the ionized matter is in pressure equilibrium with the hot, X–ray emitting gas:

$$n_X T_X \approx n_{H\alpha} T_{H\alpha} \tag{8.2}$$

Since the temperature ratio is known, $T_X/T_{H\alpha} \sim 10^3$, the $H\alpha$ gas density can be derived directly from the X–ray gas density. For NGC 4696, a galaxy for which a detailed X–ray surface brightness profile is available, it turns out $n_{H\alpha} = 65$ cm^{-3} in the innermost 200 kpc, and $n_{H\alpha} = 10$ cm^{-3} at 1 kpc from the center. Total gas mass of NGC 4649 is $M \sim 10^6$ $M_\odot$.

Several ionization mechanisms have been proposed, but none has been definitively shown to be the correct one: photoionization by active nuclei should be important in powerful radio sources, but not in normal ellipticals showing no signs of nuclear activity; photoionization from young massive stars, is expected to produce clumpy $H\alpha$ emission, at variance with what is observed; PAGB stars are a viable source of photoionization, but this should give rise to a UV flux–emission line luminosity correlation, not present in the data. In any case, it is likely that the observed range in $H\alpha$ luminosity is determined by the amount of cold gas present in these systems, rather than by the radiation field needed to ionize it.

From radial–velocity measurements of the [NII] and $H\alpha$ lines, it results that a high percentage of LINER–like galaxies show evidence of rotation in a disk–like configuration. Moreover, the [NII] linewidths have a marked increase near the nucleus, suggesting that the velocity dispersion of the gas in this region is strongly influenced by the central gravitational potential of the galaxy; the central velocity dispersion of the gas tends to be less than or equal to that of the stars. Decoupled kinematic or counter–rotation of gas and stars has been observed in dusty E's as well as in ellipticals having no dust (*e.g.* Caldwell, Kirschner, & Richstone 1986). All these facts suggest that the gas represent a second event in the history of these

E or S0 galaxies and has an external origin from an infall of a gas cloud or a gas–rich system.

8.1.3 HII–like galaxies

The emission line spectra found in low luminosity galaxies is of a very different kind, characterized by a small (≤ 0.4) [NII]λ6584/$H\alpha$ intensity ratio and narrow line widths (FWHM $\leq$ 200 km s^{-1}). Emission lines are quite strong and very extended; the gas is extended over a region $0.5 \div 1.0$ kpc in diameter, and is not in rapid rotation (Phillips *et al.* 1986).

These galaxies show abnormally blue color. Their spectra are most like those of normal galactic HII regions, and, along with the blue colors, are likely due to the presence of a young population of hot stars. Therefore, these galaxies are normal (red) low luminosity ones hosting star formation activity, as suggested also by the fact that most of them are also IRAS detection.

8.2 Neutral hydrogen in early–type galaxies

It has long been known that the morphological type of a galaxy correlates with the amount of interstellar neutral hydrogen (HI) it contains, later types having larger relative gas content.

Early–type galaxies are by far gas poorer, as they are not detected in the HI line, even at sensitivity levels of about one tenth of the HI content of large spirals.

This means that observations with large radiotelescopes (such as the Arecibo 305 m) are needed, and that statistical studies must be carried on using the survival analysis technique, which takes into account both detection and upper–limit data. Up to now, 15% of E's, 25% of S0's, and 40% of S0/a's have been found to contain an observable amount of HI gas (Knapp, Turner, & Cunniffe 1985, Wardle & Knapp 1986).

8.2.1 Neutral hydrogen content in E's and S0's

It has been found that, for elliptical galaxies, there is no correlation between the HI mass to blue total luminosity ratio M_{HI}/L_B and the total luminosity L_B itself. M_{HI}/L_B is distributed as a power law, ranging from $10^{-3}\ M_\odot/L_\odot$ to 0.3 $M_\odot/L_\odot$ (corresponding to a gas mass between $10^7 \div 10^9\ M_\odot$), most ellipticals having $M_{HI}/L_B < 10^{-3}\ M_\odot/L_\odot$ (Wardle & Knapp 1986). This means that in E's gas and stellar content are uncorrelated. In comparison, spirals have a neutral hydrogen mass to blue luminosity ratio nearly constant, with a distribution, in a log – log scale, close to a gaussian with a mean value of $M_{HI}/L_B \simeq 0.5 \div 1$.

In E galaxies, HI can often be detected beyond the Holmberg radius, and it is roughly arranged in a disk or ring; such disks often look perturbed and have

occasionally appendices reminescent of tidal tails. Moreover, there appears to be an environmental effect, E's in Virgo and Pegasus cluster having very little HI. The specific angular moment of the gas is much greater than that of stars, and it appears to be rotationally supported; however, non circular motions of the HI are apparent in the inner regions of some E's.

As for S0's, their HI content is intermediate between that of ellipticals and of early spirals. However, like E's, there is no correlation between M_{HI}/L_B and L_B (except S0/a, which conform to the relation defined by spirals, making them more similar to Sa than S0).

Many S0's present tilted outer HI rings, while some have inner rings. Furthermore, SB0s exhibit central holes in the HI distribution, which can be as large as three times the size of the bar; often they have also outer HI rings or pseudorings.

8.2.2 Origin of the cold gas

The evolutive scenarios concerning the origin of neutral hydrogen in early–type galaxies can be divided into two classes, according to whether the gas is produced inside the galaxy or is acquired from outside. We can briefly described the theories in the first class as follows (see van Driel & van Woerden 1991):

- *burnt–out disk* This model applies to lenticular. It states that lenticular galaxies are former spirals which have used up their gas in a efficient process of star formation; so the gas we observe in S0's is primordial gas not transformed into stars. While this model can explain the outer HI rings observed in most gas–rich S0's (star formation is a very inefficient process at very low surface densities, so gas is totally consumed in the inner regions, but not in the outer ones), it can non account for such features as central condensations, tilted rings, HI tails.

- *mass loss from evolving stars* It is well known that mass loss from stars is able to produce 10^9 $M_\odot$ in a galaxy of 10^{10} $L_\odot$ in a Hubble time. Since the amount of gas observed in E's and S0's is generally by far less than this, there must be some mechanism which removes the gas from the galaxy. However, mass loss from stars is expected to form filled gaseous disks, which are found in spirals but not in S0's. In order to explain the formation of the observed inner and outer rings, a suitable mechanism for the redistribution of the gas is needed.

- *Redistribution by bars* It is known that bars profoundly affect the orbits of stars and gas. They are able to remove the gas from the inner regions, producing the observed holes, and to accumulate gas on periodic orbits on, or near, the various resonances caused by the bar itself, producing the rings. However, they can not give rise to the observed warps in the outer HI distribution, and sometimes outer rings are found also in non–barred galaxies.

- *Stripping* The gas in a galaxy can be removed through an external process, such as by ram pressure of the hot intergalactic medium. However, this should cause truncated HI disks, instead of the central holes, and can not act on isolated galaxies.

The M_{HI}/L_B ratio of S0 and E galaxies does not correlate with the properties of the stellar component: this fact may point towards an external origin for the HI gas. Provided a sufficiently large external source of HI gas, such as a small or a dwarf spiral, has been available, accretion in the not too recent past (the gas must have the time to settle in a regular–looking distribution and in a well–ordered rotation) may account for the observed properties of early-type galaxies.

An alternative possibility is that the HI gas is the result of the condensation in neutral clouds of the hot ambient medium, which is the dominant component of the interstellar medium in X–ray luminous galaxies. This should be the case of NGC 4406 (Bregman & Roberts 1990), where an enhancement of the HI intensity is found in correspondence of the X–ray tail.

8.3 Molecular gas in early–type galaxies

8.3.1 CO as a tracer for H_2

Observations of ^{12}CO $1 \rightarrow 0$ emission are used to estimate the molecular mass in galaxies. In fact, the molecular hydrogen itself has a small moment of inertia and no permanent electric dipole moment (molecule is made up of two identical nuclei), and therefore has no permitted radio frequency transitions. The rotational transitions ($J = 2 \rightarrow 0$, $\lambda = 28$ μm; $J = 4 \rightarrow 2$, $\lambda = 12$ μm), rotation–vibration band at $\lambda = 2$ μm, and electronic transitions (in the Lyman and Werner bands) are either too faint or occurs in a spectral region of poor atmospheric transmission or detector sensitivity to be used for studying molecular gas in outer galaxies. The validity of using CO to trace molecular gas in galaxies is grounded on both theoretical and empirical basis (see Scoville & Sanders 1987). The $J = 1 \rightarrow 0$ fundamental transition at 115 GHz is excited by collision with H_2, even in clouds at very low kinetic temperature. The analysis of the CO–H_2 collisions shows that the constant of proportionality between the molecular gas mass and the CO luminosity scales as $M_{H_2}/L_{CO} \propto \rho^{1/2} T_{CO}^{-1}$. The same constant can be obtained empirically by estimating the molecular gas mass independently of the CO emission. For instance, M_{H_2} can be derived from the measure of the visual extinction in nearby dark clouds, or by computing the virial masses of molecular clouds using the CO and ^{13}CO line widths and cloud sizes, or by estimating the total column density of nucleons derived from gamma–ray observations. The agreement of these totally independent methods and of applications to different areas of the galaxy, suggest that global mass estimates for H_2 are probably correct to a factor of two, and

that global gradients in metallicity or physical conditions of the gas clouds do non significantly affect the CO emissivity per unit mass of H_2.

However, as we have seen, the conversion factor between the CO flux and the H_2 mass depends on the average H_2 density and on the average gas kinetic temperature T_{kin}. If T_{kin} is proportional to the dust temperature, it varies over about a factor of 2 among galaxies (the observed range of dust temperatures), introducing a factor of 2 uncertainty in the mass determination. If the ultraviolet radiation density is much higher than in the disk of the Milky Way, the CO emission can be dominated by gas at temperatures much higher than T_{kin}, so use of standard CO–H_2 conversion factor could overestimate the molecular mass by a large amount. Also potential errors associated with variations in the average gas density are significant.

8.3.2 Properties of the molecular gas

CO observations of E and S0 galaxies have shown that their molecular gas content is an order of one magnitude lower than in Spirals; the same holds also for the far–IR luminosity (Wiklind &Henkel 1989). Using the latter quantity as a measure of the current star formation rate (SFR), the typical SFR for early–type galaxies is found to be 1 $M_\odot$ yr^{-1} or less. However, E and S0 galaxies have the same far–IR colors (determined from the ratio between IR fluxes at 60 and 100 μm), and conform to the relation between $M(H_2)$ and L_{FIR} exhibited by spirals (Fig. 8.2).

This suggest that the Star Formation Efficiency (SFE), that is the star formation rate per unit mass of H_2 is nearly equal in early–types and in spirals, that is SFE is independent of the galaxy morphology. In passing, this would indicate that spiral density waves are not a necessary condition for the formation of massive stars, nor for the formation of massive molecular clouds.

Also the ratio L_{FIR}/L_B between far–IR and blue luminosity is close to the mean value of spirals. Taking the first term as a measure of the star formation rate in the latest few 10^6 yr, and the second as the measure of the star formation rate in the latest few 10^9 yr, the constancy of L_{FIR}/L_B with Hubble type indicates that SFR is low on average in E and S0, but it has been relatively constant when averaged over approximately 10^9 yr.

A further evidence of the strong similarity of the molecular ISM component in early-type galaxies and spirals is given by the $J = 2 \rightarrow 1/J = 1 \rightarrow 0$ intensity ratio, which, being $\simeq 0.5$, is interpreted as a very cold ($T_{kin} < 10$ K) gas.

The average $M(H_2)/M_{\rm HI}$ ratio is instead about 0.7, to be compared with the value of 3 in our galaxy.

Detailed mapping of a number of early-type galaxies has revealed that the molecular gas tends to be distributed in a disk, with kinematical properties of normal disk rotation, i.e. a steeply rising rotation curve in the inner parts and flat in the outer ones.

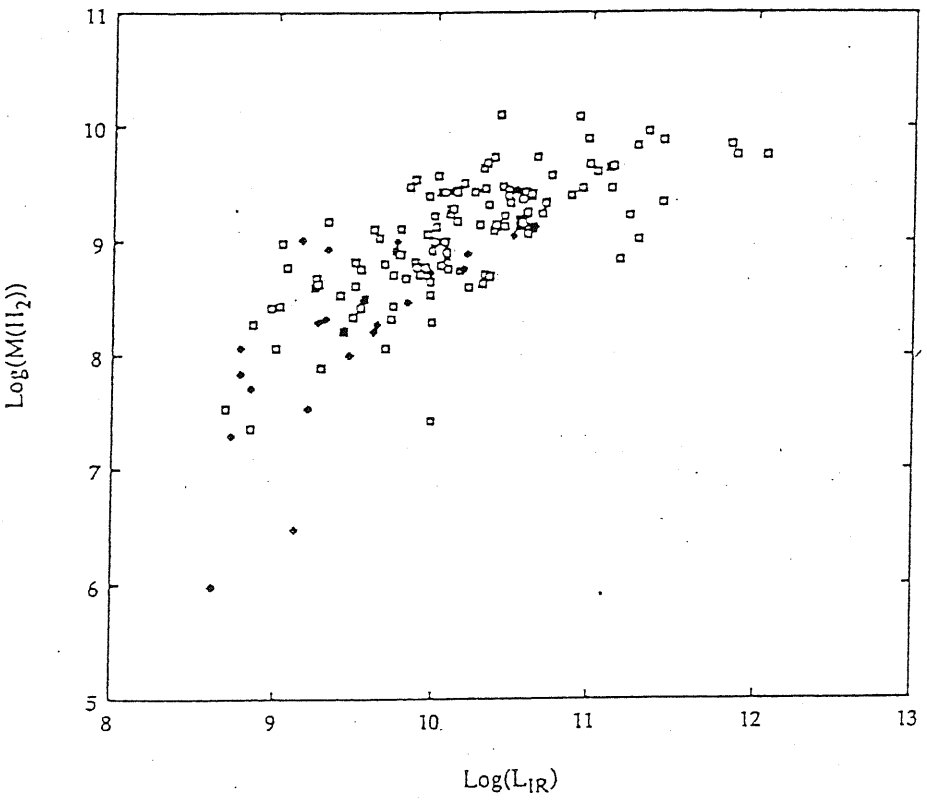

Figure 8.2: The correlation between the mass of molecular hydrogen and the far-IR luminosity. Open squares represent spiral galaxies, filled diamonds represent early-type galaxies.

8.3.3 Origin of the molecular gas

There are four possible sources for the molecular gas observed in early–type galaxies, following Wiklind (1991):

- **remnant gas** If the observed ISM in early–type galaxies is remnant from the epoch of galaxy formation, the star formation activity has to be intermittent (as happens in dwarf galaxies). In fact, continuous star formation during 10^{10} years would give broad band colors inconsistent with those observed.

- **Stellar mass loss** The stellar velocity dispersion in elliptical galaxies is high enough to heat the gas expelled from stars to temperature of 10^6 to 10^7 K, thus direct conversion of stellar mass loss to molecular gas is not possible. However, this source of molecular gas can not be ruled out in S0's, due to the much lower stellar velocity dispersion.

- **Gas capture** So far, the only indications of discrepant kinematics between the old stellar population and the molecular gas are found in Cen A. However, since for both neutral hydrogen and ionized gas there is a general consensus that they are the results of gas capture, it is likely that the same holds for the molecular gas. On the other hand, it is not clear how this can be applied also to the several apparently isolated systems.

- **Cooling flows** If cooling flows are refueling the ISM of early-type galaxies, there should be a correlation between X–ray and molecular as well as far–IR properties. No such correlation has been found.

8.4 Far infrared emission from early–type galaxies

The IRAS (Infrared Astronomical Satellite) all–sky survey covered over 96% of the sky with a completeness limit of 0.5 Jy at 12 μm, 25 μm, and 60 μm, and 1.5 Jy at 100 μm. The vast majority of the extragalactic objects detected by IRAS are late–type spirals, while elliptical and S0 galaxies have smaller detection rates, and detection is confined to the (apparently) brightest objects (Soifer, Houck & Neugebauer 1987). However, IRAS data have been revealed essential for measuring the dust content of early–type galaxies, and for recognizing a continuing star formation activity in such galaxies.

While the far infrared (far–IR) luminosity of Spirals is much larger than that of E and S0 galaxies, the long wavelength infrared spectra of E and S0 and of Spirals have nearly identical shapes, indicating a common origin of the emission. However, while for Spirals the far–IR luminosity is correlated with total blue luminosity, for early–types is not (Knapp *et al.* 1989). This is generally interpreted as due to large

variations of the ISM content at fixed luminosity, consistently with the same results found for the other phases of the intragalactic gas, and whose origin could be due to the ISM being, at least in part, acquired from outside. Other sources of scatter are a possible contribution of far–IR emission from nuclear activity, variations in the efficiency of converting the optical and UV radiation into infrared photons, or variations of the dust temperature. There is a slight dependence of the infrared flux at 12 μm with the blue luminosity, which is accounted for by the fact that at this wavelength there is a relevant contribution from stars.

The infrared emission is produced by (Thronson & Bally 1987):

1) Infrared cirrus, i.e. dust that is part of the general non star forming diffuse interstellar medium
2) dust associated with star forming region
3) photospheres of stars, and dust in circumstellar envelopes around mass losing red giants
4) Seyfert–like nuclear activity

These different sources have different infrared colours, so that their relative importance in a given object reflects on its position in a far–IR luminosity–color or color–color diagram. The contribution from stars, as mentioned before, is important at 12 μm, but is almost negligible in the other bands. The $F_{60} - F_{100}$ color discriminates between the first two sources: if $\log \frac{F_{60}}{F_{100}} > -0.35$, the far infrared flux from star forming region dominates over that coming from cirrus, vice versa if $\log \frac{F_{60}}{F_{100}} < -0.35$. This criterium has been established on the bases of IRAS observations of galactic molecular clouds hosting star formation activity and of theoretical models (Thronson & Bally 1987). About one third of early–type galaxies have infrared properties consistent with ongoing star formation, while the majority have color consistent with emission predominantly from cirrus. This does not mean that star formation has necessarily stopped in these objects, as several well–known star formation regions in the Milky Way have infrared colors compatible to that of cirrus.

The 100 μm flux can be used to compute the dust mass:

$$M_{dust} = 0.5 F_{100} D^2 \left(e^{144/T_{dust}} - 1\right)$$

where D is the distance in Mpc and T_{dust} is evaluated from the $F_{60} - F_{100}$ color, adopting a dust emissivity law $\varepsilon_\lambda \propto \lambda^{1-}$ (see van Driel & de Jong 1990). The dust temperature so obtained ranges from 25 to 45 K, and dust masses varies between $3\,10^4$ and $5\,10^6$ $M_\odot$.

8.5 Radio emission in early–type galaxies

8.5.1 Radio structures

Arcsecond imaging of elliptical and lenticular galaxies detected as radio sources frequently show components on three distinct linear scales (Wrobel & Heeschen 1991). Compact cores with powers $P_{6cm} > 10^{21}$ W Hz−1, flat spectrum, and parsec scale structure are often present. Kiloparsec scale components are often found adjacent to the compact cores, and these components are usually jetlike, and two–sided with respect to the compact core. Radio emission on galactic scales is sometime present, and often appears as outer double lobes feed by twin jets.

Three radio luminosity regimes can be identified:

- $P_{radio} < 10^{29}$ erg s^{-1}: the emission is generally confined within the central kiloparsec;
- $10^{29} < P_{radio} < 10^{31}$ erg s^{-1}: radio emission is mostly confined in the central kpc, but there can be also a more extended radio component (of the order of the galaxy size, or larger);
- $P_{radio} > 10^{31}$ erg s^{-1}: radio emission come from extended or very extended sources.

8.5.2 Origin: active nuclei versus star formation

It is thought that radio jets, lobes, unresolved cores with flat spectrum, and, if present, time variability, indicate an AGN driven radio emission. On the contrary, extended emission associated with star formation should exhibit optically thin, steep spectra; thermal emission from gas associated to star formation regions produces flat spectra.

In order to better distinguish between the two possibilities, it is useful to look at the $(S_{FIR} - S_R)$ plane, being S_{FIR} and S_R the far–infrared and radio fluxes, respectively. In this plane three groups of galaxies can be recognized (Fig. 8.3):

1. "radio excess" galaxies, which departs from the star formation $S_{FIR} - S_R$ correlation, defined by Spirals in which star formation activity is present. This group is thus characterized by the presence of extra radio emission from AGNs, as also suggested by the presence of jets or lobes adjacent to the radio core;
2. "star–forming" galaxies, which conform to the above relation;
3. "far–IR excess" galaxies, with far–IR emission but too little radio emission to conform to the relation.

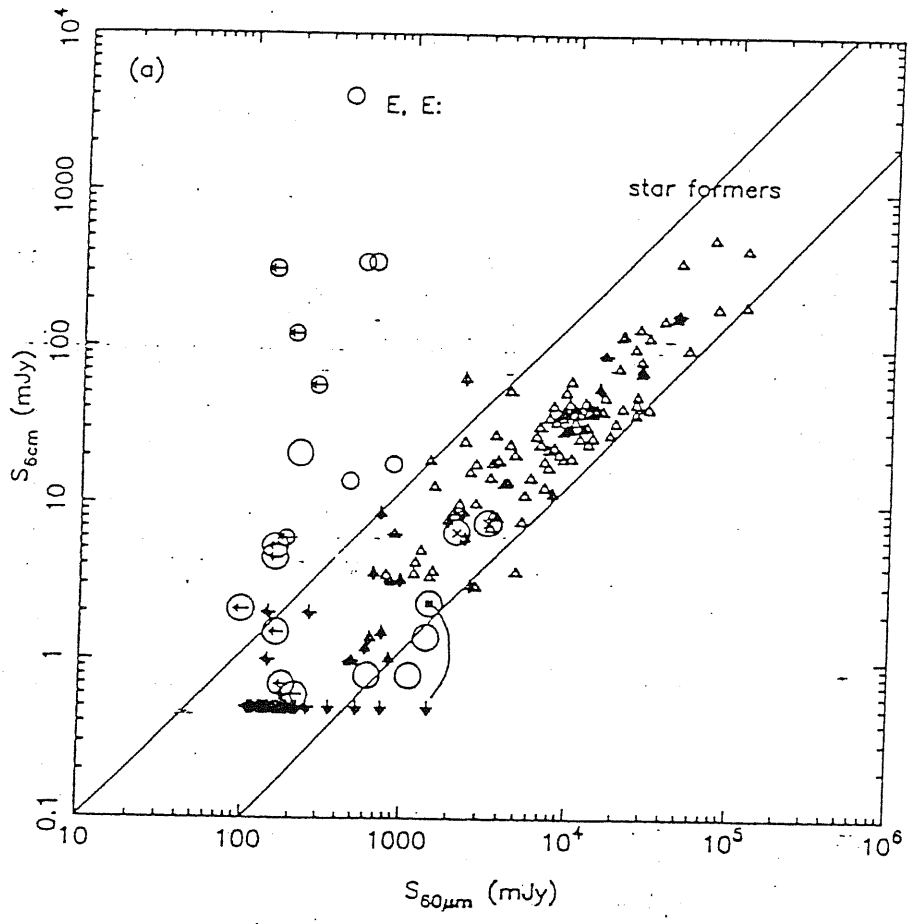

Figure 8.3: Radio fluxes density at 6 cm S_{6cm}, as a function of flux density at 60 μm, $S_{60\mu m}$ for known star forming galaxies and for E and S0 galaxies. Triangles refer to known star forming galaxies; small circles to E and S0 galaxies with AGN–driven radio emission, large circles to other E's and S0's; arrows upper limits in the radio or infrared flux. From Wrobel & Heeschen 1991.

We will notice that galaxies showing extended radio emission are characterized by having star–forming regions, or regions which are expected to be star–formation sites.

E and S0 galaxies behave differently: E galaxies are mostly radio excess, thus radio emission is mainly driven by active nuclei, while S0's have radio emission driven by star–formation activity.

As for the influence of the gas content on the radio power, it has been found that in elliptical brighter than $M_B = -18$ the presence of HI significantly enhance the likelihood that the galaxy is a radio source, while lower luminosity ellipticals are not powerful radio sources even when they contain gas; anyway, the radio power is not proportional to the HI content.

8.5.3 Radio luminosity and structural parameters

Concerning the dependence of the radio luminosity on other structural parameters, Calvani, Fasano & Franceschini (1989) have pointed out that, if the main dependence on the absolute magnitude is accounted for, there is no correlation with either central velocity dispersion or the mean surface brightness, implying that the radio emission is not related to the depth of the potential well. This is at odd with the idea that the gas responsible for the radio activity is produced by stellar mass–loss processes, as in this case we expect some dependence of radio emission on the shape of the gravitational potential. Moreover, the same authors found that radio–loud ellipticals tend to be apparently rounder than radio–quiet ones.

This seems somehow related to the known correlation between boxiness and radio–loudness (see Sect 3.2). Only ellipticals with boxy or irregular isophotes are strong radio sources, while radio emission from ellipticals with disky deviations is generally fainter. However, part of this relation may come from the relation between isophotal shape and total luminosity, while it is also known that galaxy with boxy or irregular isophote tend to be rounder.

These results can be explained considering what follows. If angular momentum of a disk component in a E or S0 galaxy is dynamically important, then it could dominate the dynamics of an associated gaseous system, which would thus be unable to travel inward to fuel a central massive object, leaving the galaxy radio–silent. On the other hand, the radio activity is due encounter and/or galactic mergers, whit large amounts of gas and dust being redistributed among the colliders, and possibly infalling, thereby providing fuel for the massive central object.

8.5.4 Radio emission and hot interstellar medium

Looking at the $(L_{RC}, L_X/L_B)$ diagram, where L_{RC} is the radio core luminosity, Fabbiano, Gioia &Trinchieri (1989) show that the core radio power has a steep

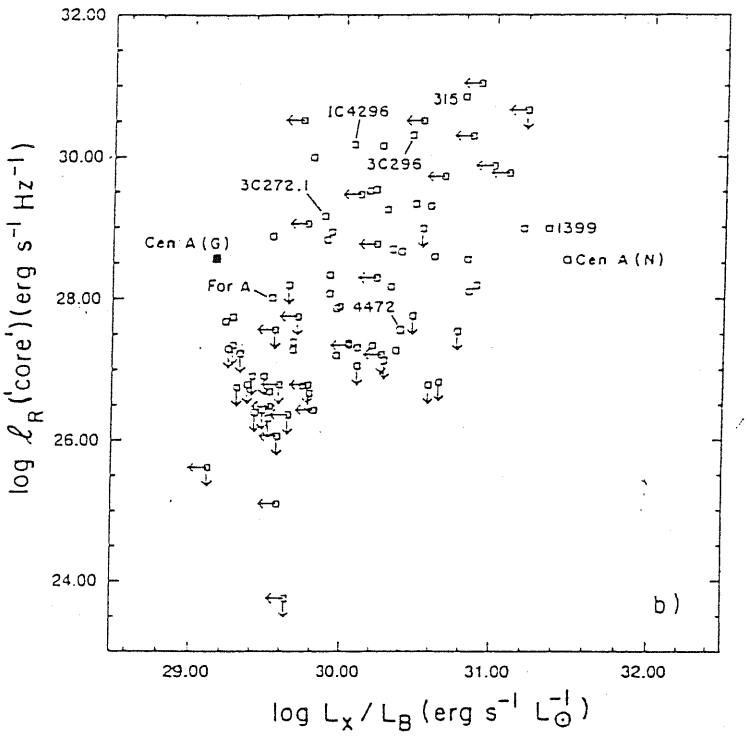

Figure 8.4: The radio core luminosity plotted versus the X–ray to optical ratio. From Fabbiano *et al.* (1989).

dependence on the X–ray to optical ratio (Fig. 8.4).

Moreover, extended radio lobes are associated to small L_X/L_B, while galaxies with high X–ray emission galaxies exhibit confined radio lobes. This suggests that the thermal pressure of the hot interstellar medium is able to confine the radio lobes; moreover, the gas is a potential fuel of the radio source, in the picture that the radio emission is due to a black hole in the nucleus of the galaxy.

8.6 X–ray emission in elliptical galaxies

As revealed by Einstein Observatory (launched in 1978; see Giacconi *et al.* 1979), normal elliptical galaxies, both isolated or belonging to group and clusters, can be powerful X–ray sources. In the range $0.5 - 4.5$ keV, their luminosity varies from 10^{39} to 10^{42} ergs. While there is a correlation of the X–ray luminosity with the optical one, the scatter is too high to be explained by observational errors: at $L_B \simeq 5\,10^{10}\ L_\odot$, scatter in L_X is about a factor of 50. In this section we shall review the properties and the sources of the X–ray flux in ellipticals, along with the information we can obtain concerning the presence of Dark Matter in E galaxies, and the theoretical models so far proposed. An extensive review of the X–ray properties of normal galaxy can be found in Fabbiano 1989, while the evolutionary

models here presented are those by Ciotti *et al.* (1991).

8.6.1 X–ray properties of spiral galaxies

Spiral galaxies are extended and complex X–ray sources, with total luminosity of $\sim 10^{38}$ to a few 10^{41} erg s^{-1}. Observations of the Galaxy and of the Local Group galaxies suggest that most of the X–ray emission is due to a collection of individual bright sources, characterized by different energies and spectral distributions:

- close accreting binaries and SN remnants, with energies in the range $10^{35} \div 10^{38}$ erg s^{-1}, and a hard spectrum ($kT > 2$ keV)
- star coronals, with smaller energies, $10^{26} \div 10^{33}$ erg s^{-1}, and a softer spectrum ($kT \sim 0.5 \div 1$ keV)
- diffuse thermal emission from a hot phase of the interstellar medium, heated by SNe
- in some galaxies, nuclear sources, which are related to star formation activity or to non–thermal Seyfert–like activity.

The X–ray surface brightness in face–on spiral galaxies has been found to follow closely the optical one, indicating that sources are distributed as the optical matter. For most spirals, the X–ray luminosity is tightly correlated with the B–band one, with an almost constant ratio $L_X/L_B \simeq 10^{-7}$ independent of other parameters such as the bulge–to–disk ratio.

In starburst galaxies (or nuclei), there is an enhanced X–ray emission, coming from young SN remnants and massive binaries, plus the coronal emission of young, massive stars. In some cases, plumes of emission have been observed, often associated to $H\alpha$ emission or to morphological/kinematical peculiarities: they are interpreted as gaseous outflows which could be responsible of the formation and enrichment of the intracluster medium.

8.6.2 Hot gaseous halos in elliptical galaxies

The presence of a hot gaseous medium in normal ellipticals is indicated by several facts. If only discrete sources were the responsible of the X–ray emission, we would expect elliptical galaxies to follow the same relation $L_X \propto L_B$ exhibited by spirals; instead, in the plane (L_B, L_X) E and SO occupy a region above that filled by spirals, and the correlation between L_B and L_X is much steeper: $L_X \propto L_B^n$ with $n \sim 1.7 \pm 0.3$. Second, the X–ray isophotes of some bright ellipticals, such as M86 and M89 in the Virgo Cluster, appear significantly asymmetric with respect to the optical ones (Fig. 8.5), suggesting that a galaxy gaseous halo is experiencing ram pressure stripping.

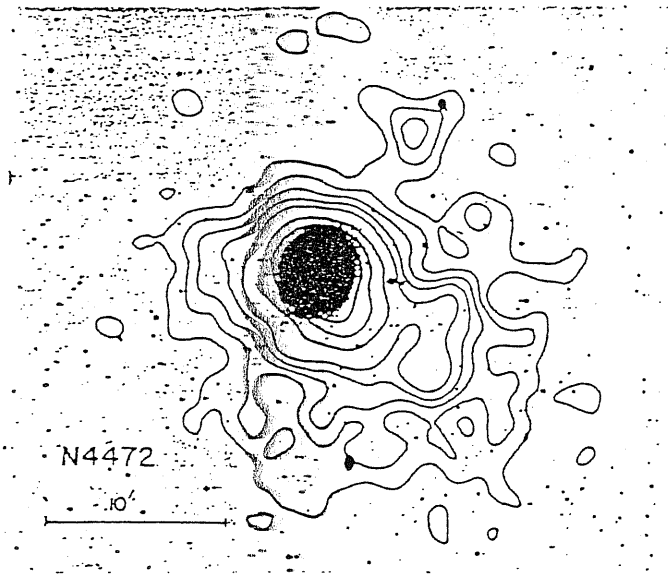

Figure 8.5: The *Einstein* X–ray map of NGC 4472, a giant elliptical galaxy in the Virgo Cluster. The asymmetry of the halo is clearly visible. From Forman, Jones, & Tucker (1985).

The X–ray emission is well extended, with radii of $\sim 40 \div 70$ kpc, generally comparable with those of the stellar distribution. The emission temperature ($kT \sim 0.5 \div 2.0$ keV), as inferred either by the spectral distribution or by the iron emission lines, is lower than that characterizing the brighter spirals ($kT > 2$ keV).

However, a more careful look at the (L_B, L_X) plane allow to recognize three groups of ellipticals (Fig. 8.6):

- faint ellipticals, with $M_B > -19.5$: they follow the trend defined by spiral, hence their X–ray luminosity is consistent with being due essentially to discrete sources; this class is composed mainly of S0's and disky E's.
- intermediate ellipticals, with $-19.5 > M_B > -22$: they show a large dispersion in L_X, for a fixed L_B, of the order of 50.
- bright ellipticals, with $M_B < -22$: they are much X brighter than spirals of comparable luminosity, so that a hot gas component must dominate the x–ray emission in all these galaxies. This class is composed mainly by boxy objects.

8.6.3 The X–ray surface brightness profiles

X–ray data can be used to derive the physical properties of the hot gas, such as central density, cooling time, total mass; in the case of the best observed galaxies, radial profiles of density and cooling time can also be derived.

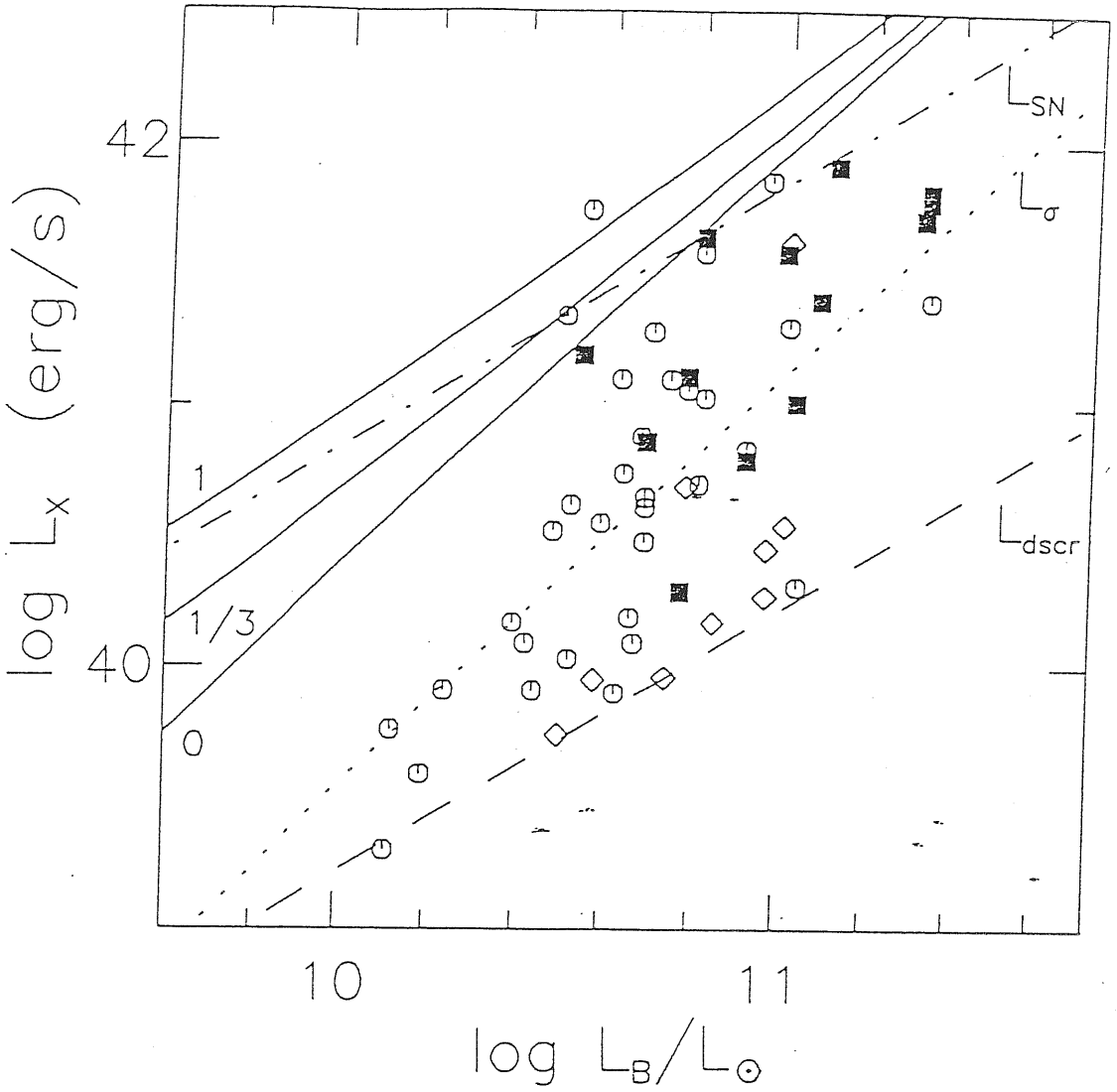

Figure 8.6: The distribution of elliptical galaxies in the (L_B, L_X) plane, from Canizares, Fabbiano & Trinchieri (1987). Filled squares and open diamonds refer to boxy and disky galaxies respectively, while open circle represents galaxies without isophotal shape information. The dashed line corresponds to the best fit of the relation exhibited by spirals, and represents the expected contribution from discrete stellar X–ray sources.

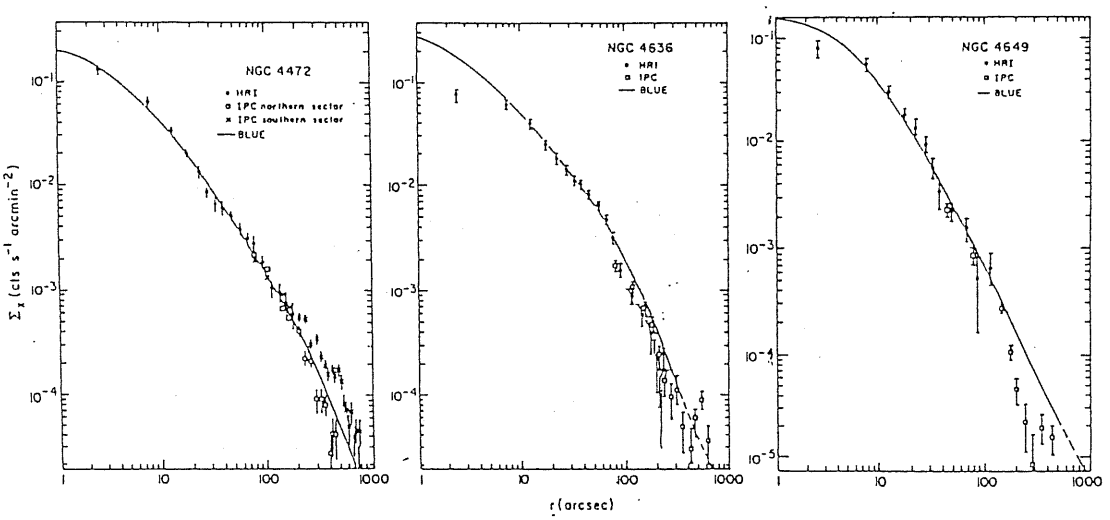

Figure 8.7: X–ray and optical (blue, from King 1978 and Lauer 1985) surface brightness profiles for NGC 4472, NGC 4436, and NGC 4649. HRI refers to the High Resolution Imager, IPC to the Imager Proportional Counter. Notice the asymmetry of the two opposite sectors of NGC 4472. From Trinchieri *et al.* (1986).

The X–ray surface brightness profile (displayed in Fig. 8.7 for three galaxies) is usually described using a parameterization of the form:

$$S_X(r) = S_X(0)\left[1 + (r/a_X)^2\right]^{-3\beta+1/2}$$

By deprojection, taking into account that the volume emissivity ε_X is proportional to N_e^2, the square of the electron density, and under the assumption that the gas is isothermal, we can derive the electron density profile $N_e(r)$ (and therefore the gas density ρ_{gas}):

$$N_e(r) = N_e(0)\left[1 + (r/a_X)^2\right]^{-3\beta/2}$$

Fits to X–ray data give $\beta \sim 0.4 \div 0.6$, so that $N_e(r) \propto r^{-(1.2\div1.8)}$, although departures from this simple law and from spherical symmetry are common. The parameter a_X, the core radius of the X–ray gas distribution, is of the order of a few kpc.

Estimates of the gas parameters give typical central densities of ~ 0.1 cm^{-3}, central cooling time ranging between 10^6 and 10^8 yr, gas masses ranging between

10^8 and 10^{11} $M_\odot$. These are upper limits, since part of the X–ray emission comes from discrete sources.

8.6.4 The mass of elliptical galaxies

Measurements of the mass of early–type galaxies are based on the assumption that the X–ray emission is thermal bremsstrahlung from hot gaseous halos, and the gas traces the potential but does not contribute to it significantly. This is reasonable, as $M_{gas}/M_{star} \lesssim 5\%$.

The equation of hydrostatic equilibrium, in combination with the ideal gas law and under the assumption of thermal equilibrium, is:

$$M(<r) = -\frac{r_{gas} k_B T_{gas}}{G\mu m_H}\left[\frac{d\ln\rho_{gas}}{d\ln r} + \frac{d\ln T_{gas}}{d\ln r}\right]$$

where μm_H is the mean gas particle mass ($\mu \simeq 0.6$). Therefore, the measurement of the binding mass depends on four variables: the radius r_{gas} within which the mass is estimated, the gas temperature T_{gas} at this radius, and the logarithmic gradient of both temperature and gas density at the same radius. In particular, the mass depends strongly on $T(r)$, but only weakly on $\rho_{gas}(r)$.

The uncertainties on the gas temperature and on its gradient, are such that the mass estimates can differ by up to a factor of 10 (see Fig. 8.8)

Therefore, X–ray emission does not allow to prove that dark massive halos are a general feature of early–type galaxies, although there is evidence that DM must be present in cluster dominant galaxies and in most X–ray luminous normal ellipticals.

8.6.5 Evolutionary models for the X–ray emission

Before discovering the X-ray emission in E galaxy, models of supernova–driven galactic winds were developed to explain the apparent lack of the gas originated by stellar mass loss, inferred from radio and optical observations. Afterwards, cooling flows model have been extensively investigated, in order to account for the X–ray emission; in these models, the hot gas inflows into the center of the galaxy, releasing an energy which is the sum of three sources: the thermalization of stellar winds to the stellar velocity dispersion, the energy heating by SNe, and the gravitational energy coming from the infall. Cooling flows models however fail in two respects to reproduce the observed X–ray properties: they predict too high X–ray luminosities, and a too high central X–ray surface brightness, with X–ray profiles much more centrally concentrated that the optical ones. Moreover, there is the problem of the fate of the gas accumulating in the center of the galaxy. Some mechanism have been proposed to reduce the X–ray output of these models, such as thermal instabilities inducing local condensations, or lower SN explosion rate, but none has revealed satisfactory.

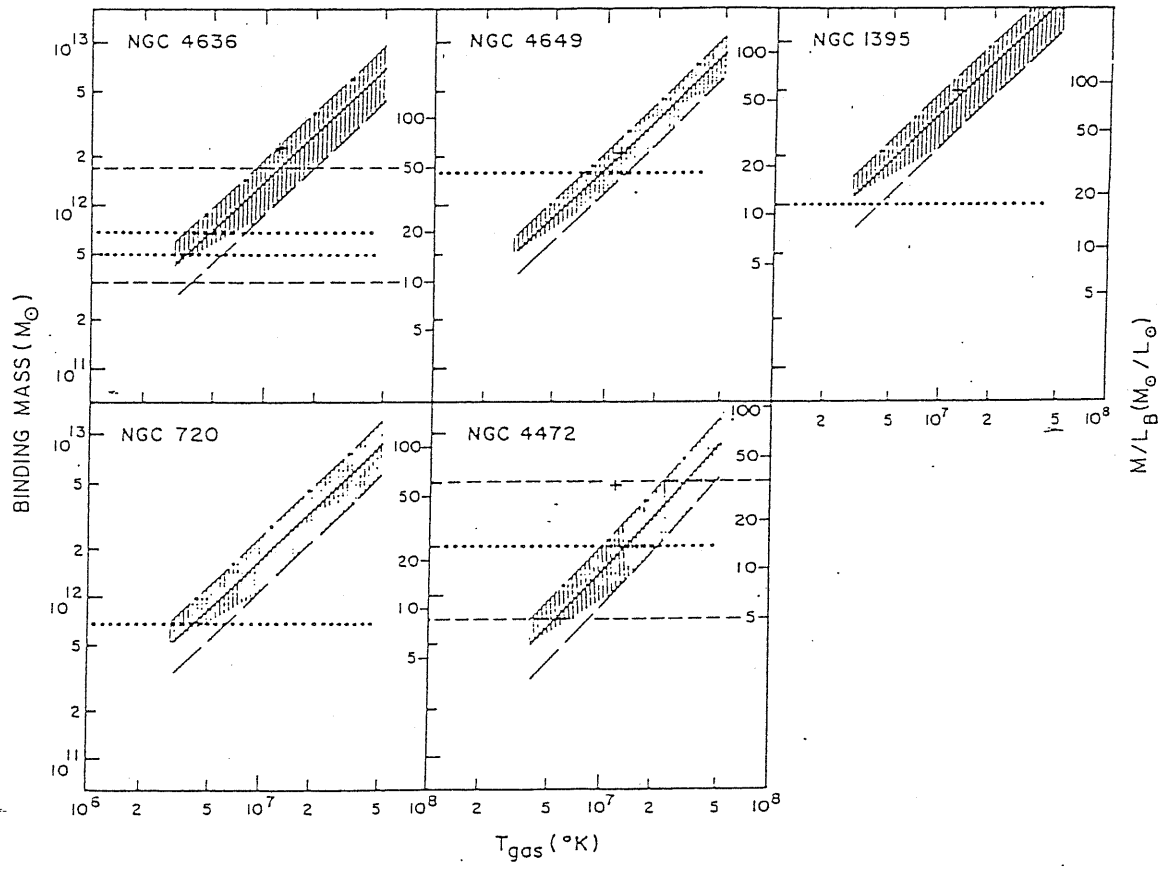

Figure 8.8: The allowed values of the binding masses and corresponding M/L ratio for 5 galaxies, as a function of the gas temperature. The solid line bisecting the dashed region gives the masses in the isothermal case; the lines defining the upper and lower envelopes of the dashed region correspond to the case $T \propto r^{-0.5}$ and $T \propto r^{0.5}$ respectively. Dotted lines represent values inferred from stellar velocity dispersion data (Tonry and Davies 1981), dashed lines represent the range of M/L derived by Katz and Richstone (1985). From Trinchieri *et al.* (1986).

Recently, a new class of hydrodynamical evolutionary sequences for the gas flows in elliptical galaxies has been built (Ciotti *et al.* 1991): in these models, galaxies evolve through up to three consecutive stages: the wind, outflow and inflow phases, according to the characteristics of the galaxy. Aim of this section is to describe briefly these models, and to compare them with observations.

Model galaxies and source terms

Galaxy models

Elliptical galaxies are described as King or de Vaucouleurs ($r^{1/4}$) models. Each model is identified by five independent parameters, which for the $r^{1/4}$ law are:

- L_B, the total blue luminosity,
- $\sigma_\star$, the stellar velocity dispersion (assumed to be independent of the radius),
- r_t/r_e, the ratio between the tidal radius and the effective radius,
- M_{DM}/M_{lum}, the ratio between dark and luminous mass,
- r_{DM}/r_c, the ratio between the core radius of the Dark Matter distribution (assumed to follow a quasi–isothermal law) and the effective radius.

We shall notice that the effective radius is fixed by L_B and $\sigma_\star$ imposing that galaxies lie on the Fundamental Plane, while the total luminous mass is fixed by r_e and $\sigma_\star$ through the Poveda formula.

Stellar mass loss

In a stellar population, stars restitute mass to the ISM at a rate which, in case of a single–age population, is given by:

$$\dot{M}_\star(t) = \psi(M_{TO})|\dot{M}_{TO}|\Delta M \qquad (M_\odot \text{ yr}^{-1})$$

where ψ is the initial mass function (IMF), $M_{TO}(t)$ is the turnoff mass of the population, and ΔM is the mass restituted by the star of mass M_{TO} to the interstellar medium. The quantities entering the above formula can be evaluated from stellar evolutionary models. A useful approximation is:

$$\dot{M}_\star(t) = -1.5\,10^{-11} L_B t_{15}^{-1.3} \qquad (M_\odot \text{ yr}^{-1})$$

where t_{15} is the age in units of 15 Gyr), valid in the range ~ 0.5 to over 15 Gyr; the time exponent is fairly insensitive to variations of the IMF slope. We also define the specific rate of mass return $\alpha_\star = \dot{M}_{star}/M_\star$.

SN heating

Only type I supernovae have so far been observed in elliptical and S0 galaxies. Two scenarios have been proposed to explain SN I explosions, both involving carbon deflagration in a white dwarf accreting mass from a binary companion, and exceeding the Chandrasekhar limit:

1) *Single Degenerate* model: the companion is a living, evolved star which fills its Roche–lobe and pours matter onto the WD.
2) *Double Degenerate* model: also the companion is a WD, and the explosion occurs when the two WD merge as a result of angular momentum losses via gravitational wave radiation.

In both models, the SN I rate turns out to be secularly declining, and can be described by:

$$R_{SN}(t) = 2.2\,10^{-13}\theta_{SN} L_B t_{15}^{-s} \qquad \mathrm{yr}^{-1}$$

where θ_{SN} is a parameter. For $\theta_{SN} = 1$ and $t_{15} = 1$ the standard SN I rate in ellipticals is recovered, i.e., 0.22 SNU (SN per century per $10^{10}\ L_\odot$). The s value is slightly larger than 1.3, so that R_{SN} decreases slightly faster than $\alpha_\star$. It assumed that each SN I injects into the ISM a total kinetic energy $E_k = 10^{51}$ erg, and ejects 1.4 $M_\odot$, of which 0.5 $M_\odot$ is ^{56}Ni which ultimately decays into iron; therefore, the specific mass return rate is $\alpha = \alpha_\star + \alpha_{SN}$.

We shall notice that one can gather information on the SN heating by comparing the iron abundance in the flows (which can be obtained from the X–ray iron lines) to that of stars.

The energy budget

There are four terms entering the global energy balance of the ISM:

- kinetic heating:

$$L_\sigma = \frac{3}{2}\alpha(t)\int_0^{r_t} 4\pi r^2 \rho_\star(r)\sigma_\star^2(r)dr$$

  which is due to thermalization through collisions between stellar winds, and/or between winds and ambient gas;

- the power required to steadily from the galaxy the gas shed by stars:

$$L_{grav}^- = -\alpha(t)\int_0^{r_t} 4\pi r^2 \rho_\star(r)\phi(r)dr$$

- the power generated by the steady inflow of this gas through the galactic potential well, down to the galaxy center:

$$L_{grav}^+ = \alpha(t)\int_0^{r_t} 4\pi r^2 \rho_\star(r)[\phi(r) - \phi(0)]dr$$

- the SN heating:

$$L_{SN} = E_k R_{SN}(t) \simeq 7.1\, 10^{30} \theta_{SN} L_B t_{15}^{-s}$$

The function $\chi(t)$ is defined as the ratio of the power required to steadily extract the gas from the galaxy, to the power actually made available by kinetic and SN heating. It can be approximated as:

$$\chi(t) = \frac{L_{grav}^{-}(t)}{L_\sigma(t) + L_{SN}(t)} \simeq \frac{t_{15}^{s-1.3}}{\theta_{SN}} \left(\frac{\sigma_\star}{300}\right)^2 F(M_{DM}/M_{lum}, r_{DM}/r_e, r_t/r_e)$$

where F is an adimensional function of the order 1.

According to the dependence of χ on t, we can recognize four cases:

1. $\chi(t) < 1$ at any time: galaxies are able to sustain a supersonic wind from the beginning all the way to the present; thus, since they contain little gas at any time, such galaxies are faint X–ray emitters.

2. $\chi(t) > 1$ wind is energetically impossible, and an inflow is established over the whole time interval; this case corresponds to cooling flow models.

3. $\chi(t) > 1$ initially, then $\chi(t) < 1$: galaxies initially host an inflow, and as *chi* decreases below unit, the inflow is turned into an outflow and eventually into a wind.

4. $\chi(t) < 1$ initially, then $\chi(t) > 1$: initial wind turns later into inflows.

We note that for $\theta_{SN} = 1$ and low values of M_{DM}/M_{lum} one has $\chi \ll 1$ for any reasonable combination of the other parameters. Furthermore, for low $\sigma_\star$ the present χ is less than unit with the standard SN rate, hence low X–ray luminosities are predicted; for high $\sigma_\star$($\gtrsim$ 300km s^{-1}) one has $\chi \gtrsim 1$ even for modest amount of dark matter, hence large X–ray luminosities are expected.

The evolutionary sequences

Model galaxies are initially assumed devoid of gas. This is a reasonable assumption, since at the very early stage of star formation, the explosions of type II SN are able to produce supersonic winds which sweep out all the gas inside the galaxy. SN II are confined in the first few 10^7 yr.

The galaxy evolves trough three main phases, which can be roughly sketched as follows:

- *wind* phase: Initially the rate of SN I is so high that most of the gas produced by stellar mass loss is lost from the galaxy by means of supersonic wind. After a few Gyr (the exact length depending on the values of the structural parameters) the gas content M_{gas} has reached a minimum.

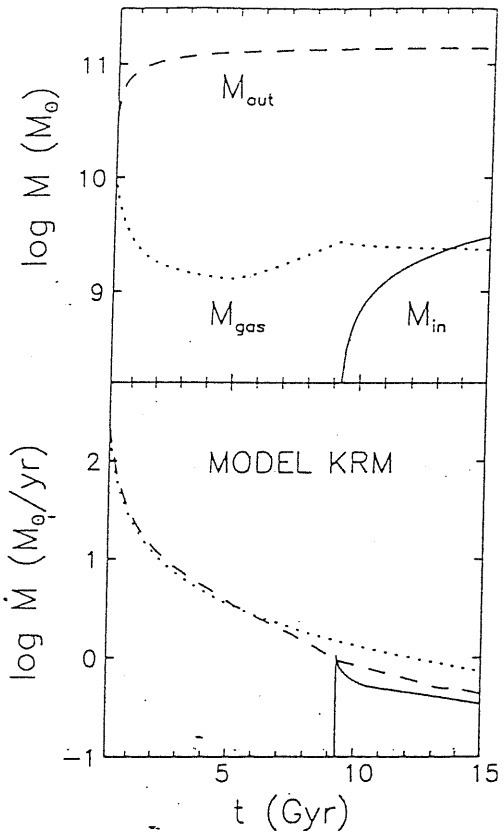

Figure 8.9: Time evolution of the mass budget of hydrodynamical model. The upper panel shows the total mass of the hot gas (M_{gas}) inside the galaxy, together with the total mass ejected from the galaxy M_{out} and lost in the central sink M_{in}. The lower panel shows the time derivative $\dot{M}_{out}$ and $\dot{M}_{in}$, together with the total rate of mass return $\dot{M}_\star$.

- *outflow* phase: The faster decreasing of SN I rate with respect to $\dot{M}_\star$ cause the rate of the gas loss rate $\dot{M}_{out}$ to become smaller than $\dot{M}_\star$, thus the gas content starts increasing. In this phase, the gas inside the galaxy has nearly no temperature gradient, due to the distributed SN heating, while outside the galaxy gas cools down in a quasi-adiabatic expansion.

- *inflow* phase: when at the center the heating rate drops below the cooling time rate, a "central cooling catastrophe" suddenly reverts the direction of the flow in the inner region. This phenomenon rapidly affects a large part of the galaxy (say the inner $5 \div 10$ kpc), while outside this region the outflow keeps on.

The mass budget evolution of this model is sketched in Fig. 8.9.

Since there is a close similarity between the time evolution of L_X and M_{gas}, as cooling is proportional to the square of the gas density, we expect galaxies in the wind phase to have a very faint X-ray emission, galaxies in the outflow phase to show a larger L_X, reaching a maximum at the occurrence of the inflow phase, in

which objects show a X–ray surface brightness profile peaked at the center (much more than the optical profile), due to the peaked gas density.

The length of each stage depends on the exact value of the structural parameters. For instance, since the depth of the potential well and L^-_{grav} are both proportional to $\sigma_\star^2$, the larger $\sigma_\star$, the deeper the potential well, the harder for the gas to leave the galaxy, the sooner the model galaxies experience their cooling catastrophe and the associated X–ray brightening; keeping L_B and all the other parameters fixed, we expect L_X to vary from $\sim 10^{38}$ to over 10^{41} erg s^{-1} as $\sigma_\star$ varies from 240 to 265 km s^{-1}. Furthermore, models in this range of $\sigma_\star$ are very sensitive to changes in every other parameter.

If instead we fix $\sigma_\star$ and let L_B increase, as a consequence r_e increases, so the galaxy gets bigger and its density gets smaller. Therefore, gas densities are lower, radiative losses are reduced, the cooling catastrophe is delayed. This would suggest that more luminous galaxies should have lower X–ray luminosities, but actually, as required by the Faber–Jackson relation, $\sigma_\star$ increases with L_B, and this effect dominates in a large sample of galaxies.

The effects of the environment

Galaxies in cluster are actually surrounded by the intracluster medium. For galaxies at rest in the cluster, the effect of the medium is to contain the outflowing gas, which, at the start of the cooling catastrophe, will fall down into the galaxy center, together with the gas already present inside the galaxy. As a consequence, the X–ray luminosity will be increased ; in practice, the outer pressure simulates the presence of a massive dark halo.

If, as it is, galaxies are moving inside the cluster, the effects are more complicated. While it is likely that the outer parts of the X–ray coronal are ablated, it is not clear what happens to the inner core, so both an increase or a decrease of L_X should be expected, depending on whether a core inflow is triggered or not. There are however some evidences that ellipticals in the rich Coma cluster are underluminous in X compared to galaxies in Virgo (a much looser cluster), explained as a more effective ram pressure stripping in the Coma cluster. However, also the tidal stripping of the dark matter halo could be the cause.

Another problem or galaxy in cluster is the fact that a temperature gradient must exists between the galaxy gas ($T \sim 10^7$ K) and the hotter intracluster medium ($T \sim 10^8$ K). Therefore, some mechanisms (magnetic fields?) must exist which suppress the heat conduction and the subsequent evaporation of the gaseous galactic halo.

As for encounters with other galaxies, in case of a merge with a smaller galaxy, the resultant deepening of the potential well could anticipate the transition to the inflow regime, producing a major X–ray brightening; if a wide tidal encounter occurs, a supersonic wind, due to the stripping of the DM halo or to the reduction of the effective L^-_{grav}, could be triggered, and a decrease in L_X is expected. The

boxiness–L_X correlation can thus be accounted for by a late merging causing at once the isophotal distortion and the transition to the inflow regime, or by the L^-_{grav}/L_B ratio being smaller in rotationally supported galaxies.

Comparison with observations

The models we have described are successful to reproduce the observed correlation between L_B and L_X, and the associated scatter. Faintest galaxies are predicted to be in their wind phase, while the X brightest galaxies have already experienced the transition to the inflow phase. The remaining galaxies are in the outflow phase, in which case the large dispersion in L_X at fixed L_B is naturally accounted for by the high sensitivity of the X output to even modest variations in the structural parameters, such as central velocity dispersion or the M_{DM}/M_{lum} ratio. The models also predict the trend of the X surface brightness profile: during the wind phase it is narrower than the optical one, closer or wider than the optical in the outflow phase, and much more centrally peaked in the inflow phase. The three galaxies for which detailed data are available appear to be in its outflow phase.

The fate of the inflowing gas

Even if also in this models the "mystery" of the fate of inflowing gas is present, the situation is by far less dramatic with respect to the cooling flow models, for two main reasons:

1) Only the brightest galaxies have already transited to the inflow phase
2) The infalling gas is only a fraction of the total gas produced, since the greatest part is lost from the galaxies in the initial superwind phase.

However, the problem still exists, at a reduced scale. A viable solution is the star formation: as 10^9 $M_\odot$ are accumulated in the galaxy center, the gas settle in a dense disk, few 100 pc in diameter, which may soon become gravitationally unstable and fragment into starlike objects (lower main sequence stars, jupiters, brown dwarfs). It must be noticed that recent star formation has been detected in some medium redshift elliptical galaxies (post–burst ellipticals), as indicated by spectral characteristics typical of intermediate stars.

Chapter 9

The UV flux in E galaxies

9.1 The observations

UV spectra of a large sample of galaxies have been obtained with the IUE (*International Ultraviolet Explorer*) satellite, launched in (1978). The most striking result has been the discovery that most of the galaxy exhibit a strong upturn in the spectral energy distribution, with a rise shortward of $\lambda \simeq 2300$ Å (Fig. 9.1).

Since the stars that are expected to produce most of the light in a E galaxy show a "normal" spectral energy distribution, declining monotonically as λ decreases, there must be a distinct stellar population characterized by a very high effective temperature $T_{eff} \gtrsim 30000$ K. The possibility that the UV flux is due to nuclear, non–thermal source is ruled out by the spatial distribution of the UV flux, which is very close to that seen in optical bands (Fig. 9.1).

Surprisingly, the UV color $(1550 - V)$, defined as the magnitude difference between the flux in the UV range, $1250 \div 1850$ Å and the flux in the V band, correlates with the metallicity (measured by the Mg_2 index), but with two relevant differences with respect to optical colors (Burstein *et al.* 1988). First, UV color gets bluer as Mg_2 increases, while optical ones get redder; second, it varies into a range as large as 3 mags, while optical colors exhibit changes of a few tenth of magnitude (see Fig. 9.2).

Moreover, galaxies are segregated in the plane according to their isophotal properties, as shown by Longo *et al.* (1989): boxy galaxies (BG) are in the mean UV brighter and slightly more metal rich the disky ones (DG); BGs populate a region in the diagram at a more or less constant metallicity, while DGs define a sequence protruding from the 'red' end of the BG distribution and extending toward lower metallicities (Fig. 9.3). It is this second group which displays the dependence of the UV color on the Mg_2 index.

We conclude that the light in a E galaxy is the sum of two components:

1) the "standard" old, red population, dominated by stars in the Main Sequence, in the Subgiant Branch and in the Red Giant Branch;

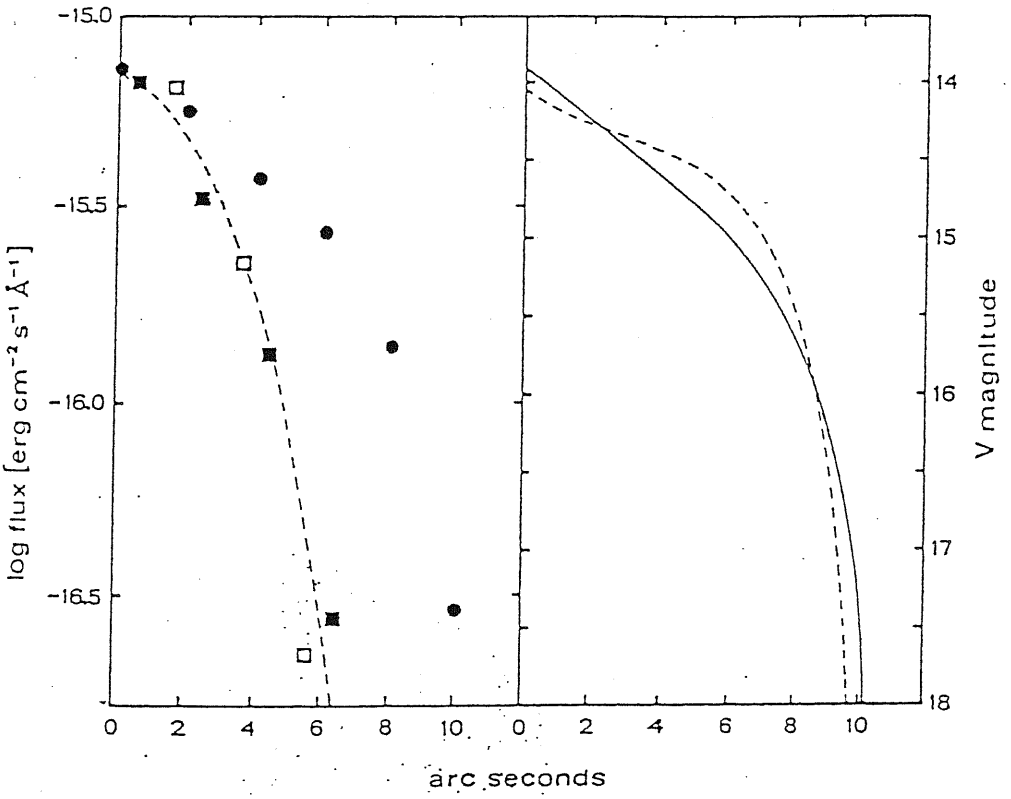

Figure 9.1: Left: the visual and UV energy distribution of the nucleus of M87. Right: The UV smoothed luminosity profile (solid line) compared with the blue profile (broken line) of M87. From Bertola *et al.* (1980).

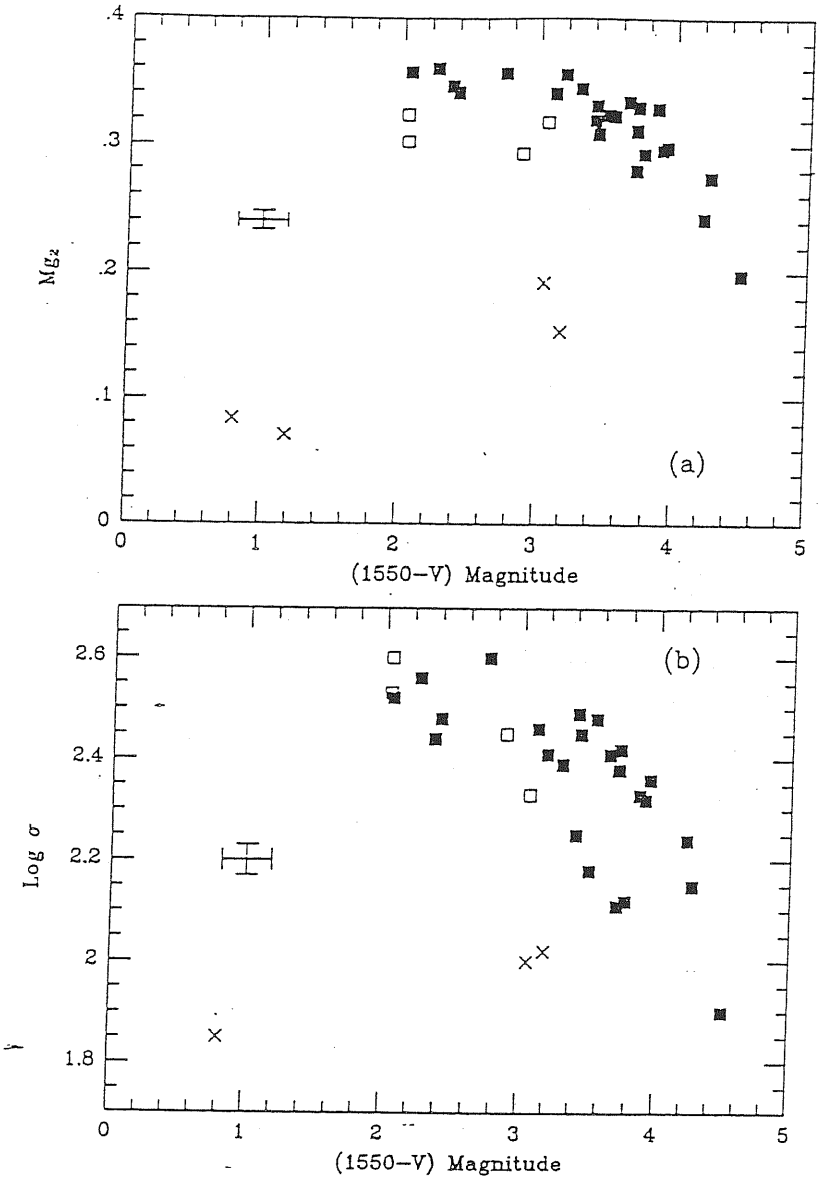

Figure 9.2: Upper panel: the optical absorption index Mg_2 plotted vs. the ultraviolet/optical $(1550 - V)$ color for 32 galaxies in the sample of Burstein *et al.* (1988). Closed squares represent "quiescent" galaxies, open squares "active" galaxies and crosses galaxies with on–going star formation. Lower panel: central velocity dispersions are plotted vs. the $(1550 - V)$ color.

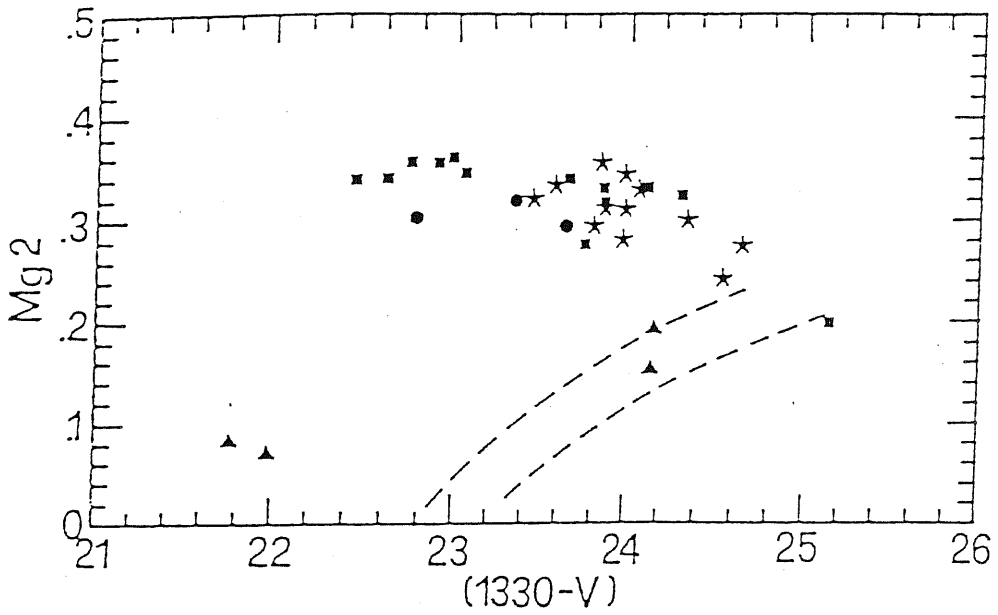

Figure 9.3: Mg_2 versus UV color for a sample of early–type galaxies with isophotal shape data. Filled squares represent boxy and irregular galaxies, asterisks disky galaxies, triangles and filled circles star forming and active galaxies respectively. Dashed lines are the 'bluing vectors' followed by objects experiencing star formation activity (Burstein *et al.* 1988).

2) a very hot component ($T_{eff} \gtrsim 30000$ K), with a steep slope toward the far UV. The large variation in the $(1550 - V)$ color is due to a large change in the amplitude of this hot component relative to the old one. The change is driven by metallicity.

9.2 Possible sources of the UV flux

The possible candidates of the UV flux are usually divided in the following four groups:

1. young stars
2. hot HB stars
3. stars in binary systems
4. post–AGB stars

9.2.1 Young stars

They have been proposed by several authors as responsible for the UV flux. For instance, Veron & Veron (1985) propose that, if optical $U - B$ and $B - V$ colors are reported to a same absolute magnitude, on the basis of the well–known color luminosity relation, galaxies tend to place in the $(B - V, U - B)$ diagram along the line: $U - B = 2(B - V) - 1.4$, with a pretty small scatter, and with the star forming galaxies at the blue end. This figure can be reproduced by adding a variable amount of a young population ($B - V \simeq 0.2$, $U - B \simeq -0.1$) to the old one ($B - V \simeq 1.0$, $U - B \simeq 0.6$). Also Bica and Alloin (1988) reached a similar result through a population synthesis model in which the ingredients are globular and open clusters, spanning a wide range in age and metallicity. They pointed out that young cluster are needed to reproduce the UV and optical energy distribution of elliptical galaxies.

However, there are several points which makes young stars unlikely to be the sought UV sources (see Greggio & Renzini 1990):

- star forming galaxies do not follow the $Mg_2 - (1550 - V)$ relation defined by quiescent ones;
- in the bulge of M31, as well in NGC 205, no young stars have been detected;
- star formation is expected to be patchily distributed and peaked toward the center, while UV and optical surface brightness have the same radial trend;
- type II SNs have never been observed in elliptical galaxies.

Moreover, at present there is no theory capable of explaining why stellar formation is so strongly influenced by metallicity.

9.2.2 Hot Horizontal Branch stars

It has been demonstrated (Nesci & Perola 1985) that a bimodal T_{eff} distribution of HB stars is required to reproduce the observed gradient, with the peaks at $T_{eff} \simeq 20000$ and $T_{eff} \simeq 6000$. This is at variance with the fact that, since E galaxies are metal–richer than Globular Cluster, we expect a very red HB. However, the HB morphology is affected also by the mass loss star during the RGB phase, which can be a function of the metallicity and of the helium content. If mass loss is important, and significantly affected by metallicity, it could be possible to produce the required bimodal distribution

9.2.3 Stars in binary systems

It is known that up to 50% of stars are members of binary systems, with separation small enough to allow Roche lobe overflow in the course of their evolution. However, due to the complexity of the problem, and due to the large variety of of possible situations, models of photometric synthesis with the contribution from binary stars taken into account are still lacking, so that, also because of the success of PAGB models, the binary star alternative for the UV emission is almost never considered.

9.2.4 Post–AGB stars

The UV flux is interpreted as due to low mass stars in their final evolution toward the white dwarf cooling sequence. For instance, Brocato *et al.* (1990) suggest that in metal–rich galaxies the HB stars present an evolutionary behaviour that does not follow the traditional path (Schönberber 1983). Their model predicts that either a $\Delta Y/\Delta Z$, the increase of the Helium content with the metallicity due to galactic chemical evolution, larger than zero, or an increase of the mass–loss rate with metallicity, will cause stars with metallicity greater than a critical value Z_c to evolve from the HB toward the early phase of the AGB, but not to develop thermal pulses, because the H–burning shell reaches the external layers of the star. At this point, the stars cross the HR diagram toward the blue and settle on its cooling sequence, with a mass coinciding with the mass in the HB. The metallicity dependence on metallicity is explained by the fact that the masses of stars in this phase get smaller as Z increases, and as a consequence the time spent in the blue phase, inversely proportional to the final star mass, gets longer.

On the contrary, according to Bertelli, Chiosi & Bertola (1989) the stars responsible of the UV flux are classical post–AGB stars which have experienced the thermal pulse phase, superwind and planetary nebula ejection. The dependence of the UV flux on metallicity is explained, in the frame of the mixing–length theory, as due to the Helium enrichment following from the enrichment in metals, and using normal values for the mass loss rate on the RGB and the superwind phase.

9.3 Future observational strategies

What kind of observations could give further information on the UV flux in galaxies, and what test can be performed concerning the possible sources?

Globular Cluster are suited for studying Post–AGB stars, even if very hot stars ($T_{eff} > 35000$ K) could be undetected in optical bands. Spectroscopic observations (both in optical and UV) could help understand the "history" of these stars, so as to reconstruct their evolutionary path and distinguish among the different models proposed. On the other hand, the binary star population in G.C. is different than in ellipticals, due to the strong dynamical evolution occurring in G.C. Deep photometry in M31 could be a tool to investigate accreting white dwarf, which should distinguish from other hot stars because of their variability on months to years timescales.

In the bulge of our galaxy very metal–rich stars can be found. However, the very strong absorption put these stars below the current photometric threshold; HST could go 2 mag deeper.

Important information could be obtained by looking at the redshift–UV flux dependence. As the galactic age decreases, the mass of the stars on the phases later than the Main Sequence increases, and therefore in the Post–AGB and in the HB stars models the UV flux is expected to decrease with redshift; in the former case, the UV spectrum become harder, in the latter softer. It is essential to extend the $Mg_2 - (1550 - V)$ relation to redshift of the order 0.2, but this would require a $5 \div 10$ meter telescope in orbit.

Chapter 10

Chemical evolution of E galaxies

Elliptical galaxies are complex system with a mix of different stellar population, characterized by differences in chemical composition and age. In order to study the "history" of an elliptical galaxy, both in term of luminosity and colors, a detailed chemical evolution model is required. The model is required to reproduce the observed global properties of early–type galaxies: spectral distribution, color–luminosity (hence mass) correlation, color gradients inside the galaxy, and so on.

The first model constructed were based on oversimplified assumption: a single star burst (i.e. the time interval to convert all the gas into stars is negligible compared to the present galaxy age) originate stars all with the same metallicity (assumed to be close to the solar abundance, $Z_\odot = 0.02$; see for instance Tinsley 1980). Later, it was realized that there must be a spread of metallicities, as the first stars to form enrich the interstellar medium with metals, so that the metallicity of newly formed stars should change as the galaxy evolves. In this way the color–magnitude diagram of E galaxies was reproduced, showing that it is due to metallicity variations.

Since the initial activity of star formation lead to subsequent supernovae explosions, and since the SN heating could be larger than the binding energy, in which case the remaining gas is expelled from the galaxy through galactic winds and the star formation stops, it is essential to take this effect into account when constructing chemical evolution models. In this section we shall describe the chemical and photometric properties of the galactic wind model for elliptical galaxies (Brocato *et al.* 1990; see also Arimoto & Yoshii 1987).

10.1 Galaxy models

The basic assumptions are:

- Elliptical galaxies are considered as homogeneous spheres of gas; initial masses in the range 10^9 to $5\,10^{12}$ $M_\odot$ are considered. They evolve as closed boxes

(no material enters or escapes from the galaxy), until the occurrence of a galactic wind.

- Galactic winds set as soon as the SN energy input becomes larger than the binding energy. This occurs earlier in less massive galaxies, and in any case within the first Gyr. At this time the star formation stops, while new gas is produced through normal stellar mass loss and SN Ia explosions, which may be responsible of further events of mass loss.

- Instantaneous mixing of gas is assumed.

- The star formation process is continuous, and the star formation rate is proportional to the gas density.

- The initial mass function (IMF) is a power law of the mass, $\phi(m) \propto m^{-(1+x)}$, and is constant in space and time.

- A proper treatment of the SN types, and of their energy and mass release is done. In particular, type II SNe are assumed to originate from single massive stars.

It is assumed that the galaxy integrated light is generated by the emission form each star populating the galaxy; therefore, neither non–thermal source, nor thermal emission from interstellar gas is considered, and moreover absorption from gas or dust is neglected.

The properties of each star are fixed by 4 parameters:
1) the mass m, 2) the age τ, 3) the helium content Y, 4) the metal abundance Z. Therefore two functions are required to derive the total flux in a given photometric band: the flux (in the same band) from a single star as a function of these four parameters, $f_x(m, \tau, Y, Z)$ and the number density of stars in this 4–D space, $N(m, \tau, Y, Z)$. f_x depends on one side on the stellar evolutionary tracks, which link the parameters (m, τ, Y, Z) to the star bolometric luminosity L and effective temperature T_e, on the other side on the stellar atmosphere models, which give the flux inside a given band coming from a star with given L, T_e, and chemical composition Y and Z. N depends on the model assumptions such as star formation rate, initial mass function, stellar nucleosynthesis, and stellar lifetimes.

10.2 Dynamical and chemical evolution

It is found that galactic winds occur later, hence star formation continues longer, in larger galaxies, because the binding energy of the galaxy per unit mass increases with increasing galaxy mass M_G (t_{GW}, the time at which the galactic wind take place, varies from $\simeq 0.05$ Gyr for $M_G = 10^9\ M_\odot$ to $\simeq 1$ Gyr for $M_G = 10^{12}\ M_\odot$). Also the fraction of initial mass which is loss depends on M_G. For $M_G \lesssim 10^{10}$

$M_\odot$, more than 30% of the mass is lost in wind, while, for instance, a galaxy with $M_G = 10^{12}\ M_\odot$ loses less than 10% of its mass. In the former case, there will be strong influence on the dynamical structure of the system: the galaxy begins to expand, until when the state of virial equilibrium is recovered. The luminous mass–to–luminosity ratio increases with the galaxy mass; however, if the mass of stellar remnants is included, the total mass–to–luminosity ratio becomes nearly constant ($\simeq 20$).

The chemical abundance in gas, at the moment in which it is expelled from the galaxy through winds, is a strong function of the mass. In general, the fraction of metals increases as the mass increases, but with significant differences among the individual elements (Fe, O, Mg, Si); in particular, Fe shows the steepest dependence on M_G. This is caused by the fact that in massive galaxies a large number of SN I, which produce the bulk of iron, had the time to explode and restore a substantial amount of this element, whereas in less massive galaxies the galactic wind appears before the occurrence of the first SN I, so that iron come essentially from massive stars. On the contrary, oxigenum and magnesium are produced mainly by SN II, and therefore their abundance are less dependent on the galactic mass. Silicium, which is produced in a non negligible amount by type I SNe, shows an intermediate behaviour.

Of course, it is by far more important to evaluate the content of heavy element in star, as this quantity can be compared with observations. As for the stellar metallicity distribution, it ranges from [Fe/H] $\simeq -2.5$ to [FE/H] $\simeq 1.0$ for massive galaxies, while it is truncated at [Fe/H] $\simeq 0$ for $M_G = 10^9\ M_\odot$, as the chemical evolution is stopped by a galactic wind before it is completed. The average metallicity increases monotonically with mass (hence luminosity), going from $\langle [Fe/H] \rangle = -0.8$ for $M_G = 10^9 M_\odot$ ($M_V = -14$) to $\langle [Fe/H] \rangle = 0.4$ for $M_G = 10^{12} M_\odot$ ($M_V = -24$). There is also a dependence on the value of the exponent of the IMF, x: models with a higher x are less metal–rich, because of the smaller number of massive stars.

10.3 Photometric evolution

All integrated colors become redder with increasing M_G, the reddening being closely related to the metallicity increasing. The mass dependence is particularly prominent in $U-B$, $V-J$ and $V-K$. (Fig. 10.1).

The color difference, for a fixed range in metallicity, is largest in $V-K$, so this color is the best suited as metallicity indicator. We shall notice that in the color–magnitude diagram there is a scatter which is greater than observational errors, and therefore it is in part intrinsic. There are several possible reasons: an intrinsic dispersion in the SFR for fixed M_G (higher SFR enhances the rate of SN explosions, inducing an anticipated wind; as a consequence, stellar metallicity decreases and colors shift bluewards), or variations in the IMF slope; also recent star formation could contribute to the scatter (after galactic wind, star mass loss

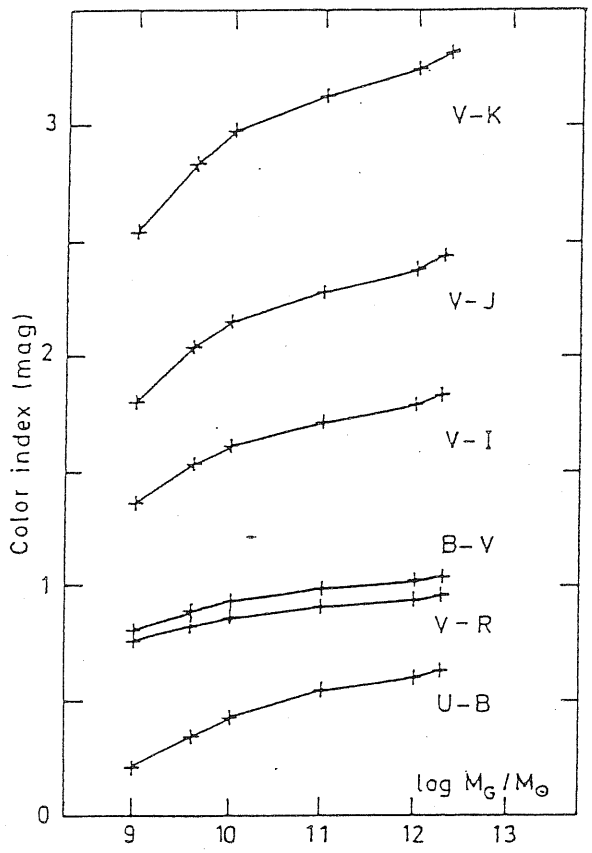

Figure 10.1: Photometric colors of the models at 15 Gyr plotted against the initial mass of the galaxy. From Arimoto & Yoshii (1987).

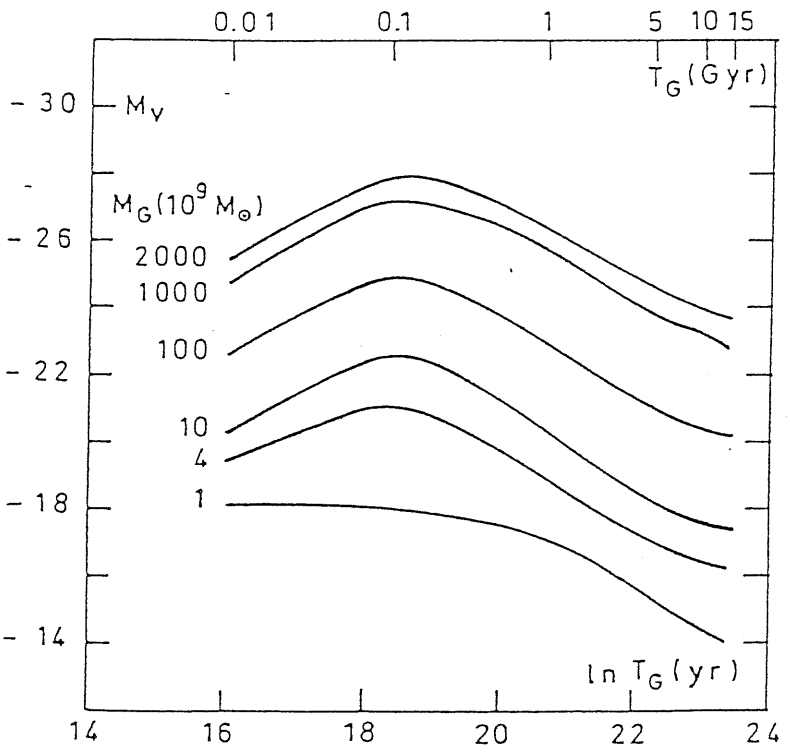

Figure 10.2: Luminosity evolution predicted by the wind galactic models. M_G indicate initial galactic mass in units of 10^9 $M_\odot$. From Arimoto &Yoshii (1987).

and SN I produce gas that could later used to from new stars).

It is traced by computing the models for several ages. Galaxies with M_G larger than $4\,10^9$ $M_\odot$ reaches a maximum when the luminosity decrement due to the death of massive stars exceeds the luminosity increment due to the formation of new stars. The maximum is reached very soon, at τ of 0.1 Gyr. On the contrary, in less massive galaxies most of gas is ejected very soon, so the contribution from newly formed stars is very small and the luminosity decreases monotonically. The luminosity decrement from this time up to the present age (15 Gyr) is of about 4 magnitudes, but is nearly independent of the galaxy mass, hence the Luminosity Function of elliptical galaxies does not change its shape during the evolution of galaxies (Fig. 10.2).

On the contrary, the evolutionary behaviour of the color depends significantly on the initial mass of the galaxy, and is determined by the evolution of those stars which contribute most to the galactic light. Just after star formation is stopped by galactic wind, upper main sequence stars dominate the light, and therefore the color turns red rapidly. At present, the distribution of low mass giants stars along the RGB, which dominate the integrated light, is nearly independent of time, and therefore there are essentially no color changes for $\tau \geq 10$ Gyr.

The dependence of the color evolution on the mass is closely related to the

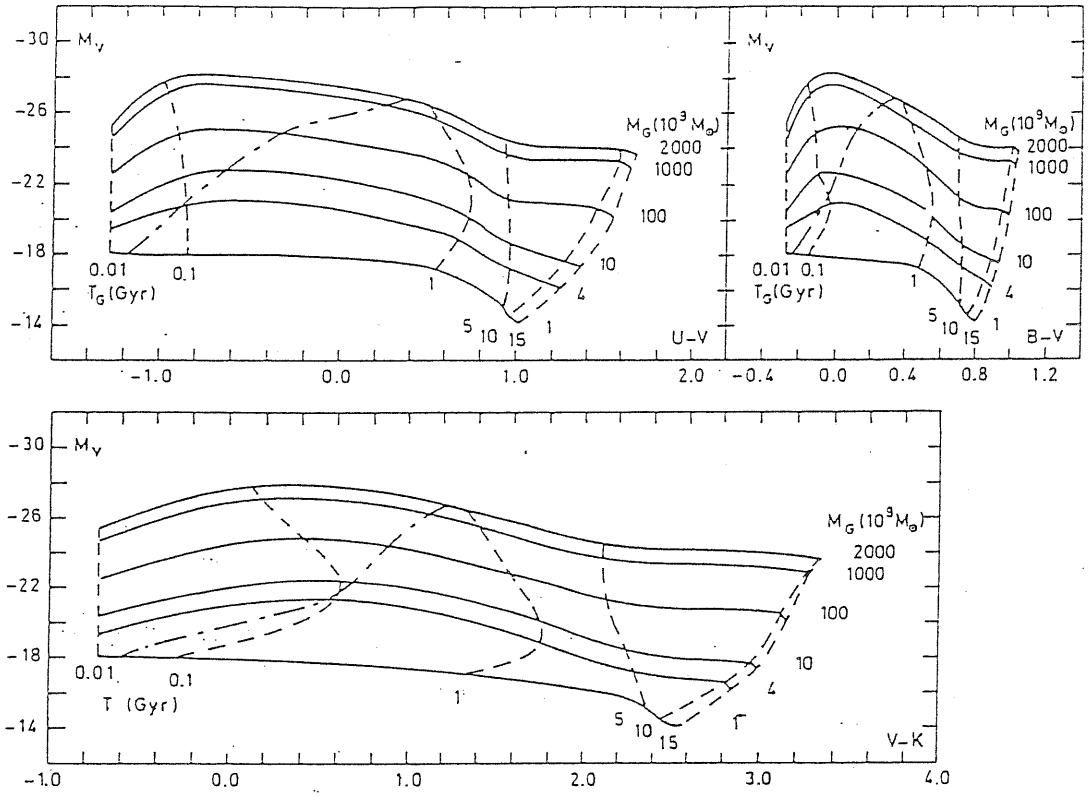

Figure 10.3: The photometric evolution in the absolute magnitude–color diagram. Solid and dashed curves represent evolutionary tracks and isochrones, respectively. Dot dashed line represents the epoch when galactic wind occur. From Arimoto & Yoshii (1987).

metallicity evolution: since the time derivative of the stellar metallicity $dZ_\star/dt$ is higher in more massive galaxies, the color changing with time is the steeper the larger is the initial mass (see Fig. 10.3). In particular, the rate of reddening is faster in the period 1 Gyr $\leq \tau \leq$ 10 Gyr, and color evolution can be detected in distant galaxies younger than 10 Gyr. Moreover, the reddening is larger in ultraviolet and infrared colors.

Notice that, while as we have seen before, at present more massive galaxies are redder, during early stage of evolution massive galaxies were bluer than less massive ones, because the star formation rate per unit mass is smaller, and hence the formation of young, massive stars continues longer. Later, the colors of massive stars become redder much rapidly because of their higher metallicity with respect to less massive galaxies.

Appendix A

The main photometric laws: useful formulae

A.1 The de Vaucouleurs $r^{1/4}$ law

The $r^{1/4}$ law is defined as follows:

$$I(r) = I_0\, 10^{-C\,(r/r_*)^{1/4}} \quad \text{with} \quad \begin{cases} I_0 = & \text{central surface brightness,} \\ r_* = & \text{'normalization' radius.} \end{cases} \tag{A.1}$$

The constant C is not empirical; its value depends on the definition of r_*. If $r_* = r_e$ is defined as the radius containing 1/2 of the total luminosity:

$$L(r_*) = \int_0^{r_*} I_0\, 10^{-C\,(r/r_*)^{1/4}}\, 2\pi\, r\, dr = \frac{1}{2}\, L_T = \frac{1}{2} \int_0^{\infty} I_0\, 10^{-C\,(r/r_*)^{1/4}}\, 2\pi\, r\, dr \tag{A.2}$$

then $C = 3.3307$.
r_e is referred to as 'effective radius'; the surface brightness at r_e, I_e, is called 'effective surface brightness':

$$I_e = I_0\, 10^{-3.3307} = (1/2141.4)\, I_0 \tag{A.3}$$

The $r^{1/4}$ law is usually written in the following forms:

$$I(r) = I_e\, 10^{-3.3307\left[(r/r_e)^{1/4} - 1\right]} \tag{A.4}$$

$$\mu(r) = \mu_e + 8.3265\, \left[(r/r_e)^{1/4} - 1\right] \tag{A.5}$$

the second of which shows that it is a straight line in the $(r^{1/4}, \mu)$ plane: $\mu = a + b\, r^{1/4}$.

Useful formulae:

Total luminosity: $L_T = \int_0^\infty I(r)\, 2\,\pi\, r\, dr = 22.665\, I_e\, r_e^2$

Apparent tot. mag.: $m_T = \mu_e(\mathrm{mag/arcsec^2}) - 5\,\log(r_e'') - 3.388$

Absolute magnitude: $M_T = \mu_e(\mathrm{mag/arcsec^2}) - 5\,\log(r_e[\mathrm{kpc}]) - 39.97$

Luminosity inside R: $L(R) = L_T\, k(z) = L_T \left\{1 - e^{-z}\left[1 + \sum_{k=1}^{7}(z^k/k!)\right]\right\}$ (A.6)

where $z = 7.669\,(R/r_e)^{1/4}$

A.2 The exponential law

It is defined as follows:

$$I(r) = I_0 e^{-r/h} \tag{A.7}$$

$$\mu(r) = \mu_0 + 1.086\, r/h \tag{A.8}$$

where h is the scalelength radius. It is a straight line in the (μ, r) plane.

Useful formulae:

Total luminosity: $L_T = \int_0^\infty I(r)\, 2\,\pi\, r\, dr = 2\,\pi\, I_0\, h^2$

Apparent total magnitude: $m_T = \mu_0(\mathrm{mag/arcsec^2}) - 5\,\log\,(h'') - 1.995$

Absolute total magnitude: $M_T = \mu_0(\mathrm{mag/arcsec^2}) - 5\,\log\,(h[\mathrm{kpc}]) - 38.565$

Luminosity inside R: $L(< R) = L_T\, G(R/h) = L_T \left[1 - e^{-R/h}(1 + R/h)\right]$ (A.9)

The radius containing half of the total luminosity is $R_{1/2} = 1.678\, h$, at which the surface brightness is $\mu_{1/2} = \mu_0 + 1.882$

A.3 The $\cosh^2$ law

The volume emissivity is expressed as:

$$\rho(r, z) = \rho_0 e^{-r/r_0} \mathrm{sech}^2(z/z_0)$$

By projecting we obtain the surface brightnesses:

$$\begin{aligned} &\text{face–on :} \qquad I(r) = 2\rho_0 z_0 e^{-r/r_0} \\ &\text{edge–on :} \qquad I(r,z) = 2\rho_0 r K_1(r/r_0)\text{sech}^2(z/z_0) \end{aligned} \tag{A.10}$$

where K_1 is a modified Bessel function of the first kind.

For the edge–on case the following approximations hold:

$$z = 0 : I(r) = 2\rho_0 r K_1(r/r_0) \tag{A.11}$$

$$z = 0, r \gg r_0 I(r) = 2\rho_0 r_0 \sqrt{\frac{2}{\pi}\frac{r}{r_0}} e^{-r/r_0} \tag{A.12}$$

$$z \ll z_0 : \quad I(r,z) = 2\rho_0 r K_1(r/r_0) e^{-z^2/z_0^2} \tag{A.13}$$

$$z \gg z_0 : \quad I(r,z) = 2\rho_0 r K_1(r/r_0) 4 e^{-2z/z_0} \tag{A.14}$$

In general, r_0 can be a function of z, $r_0 = r_0(z)$, while z_0 can be a function of r, $z_0 = z_0(r)$.

Bibliography

Aguilar, L.A., & Merrit, D. 1990, ApJ, 354, 33

Arimoto, N., & Yoshii, Y. 1987, A&A, 173, 23

Baade, W. 1944, ApJ, 100, 137

Barnes, J., & Efstathiou, G. 1987, ApJ, 319, 575

Baum, W.A. 1955, PASP, 83, 199

Bertelli, G., Chiosi, C., & Bertola, F. 1989, ApJ, 339, 889

Bender, R. 1988, A&A, 193, L7

Bender, R. 1990, Dynamics and Interactions of Galaxies, ed. R. Wielen (Heidelberg: Springer–Verlag), p. 232

Bender, R., & Möllenhoff, K. 1987, A&A, 177, 71

Bender, R., Capaccioli, M., Macchetto, F., & Nieto, J.–L. 1989a, The Messenger, 55, 6

Bender, R., Surma, P., Döbereiner, S., Möllenhoff, C., & Madejsky, R. 1989b, A&A, 217, 35

Bertola, F., 1987, IAU Symp. No. 127, Structure and Dynamics of Elliptical Galaxies, ed. T. de Zeeuw (Dordrecht: Reidel), p. 135

Bertola, F., & Capaccioli, M. 1975, ApJ, 200, 439

Bertola, F., & Capaccioli, M. 1978, ApJ, 219, L95

Bertola, F., Buson, L.M., & Zeilinger, W.W. 1988, Nature, 335, 705

Bertola, F., Vietri, M., & Zeilinger, W.W. 1990, Bulges of Galaxies (La Serena), eds. B. Jarvis and D.M. Terndrup (Garching: ESO Workshop Publ.), p. 275

Bertola, F., Capaccioli, M., Holm, A.V., & Oke, J.B., 1980, ApJ, 237, L65

Bertola, F., Bettoni, D., Danziger, J., Sadler, E., Sparke, L., & de Zeeuw, T. 1991, ApJ, in press

Bettoni, D. 1989, AJ, 97, 79

Bettoni, D., & Buson, L. 1987, A&AS, 67, 341

Binggeli, B., Sandage, A., & Tammann, G. 1985, AJ, 90, 1681

Binggeli, B., Sandage, A., & Tammann, G. 1988, ARA&A, 26, 509

Binney, J. 1978, MNRAS, 183, 501

Binney, J., & de Vaucouleurs, G. 1981, MNRAS, 194, 679

Binney, J. & Tremaine, S. 1987, Galactic Dynamics (Princeton: Princeton Univ. Press)

Bothun, G.D., Caldwell, N., & Schombert, J.M. 1989, AJ, 98, 1542

Brocato, E., Matteucci, F., Mazzitelli, I., & Tornambé, A. 1990, ApJ, 349, 458
Brosche, P. 1973, A&A, 23, 259
Caldwell, N. 1983, ApJ, 268, 90
Caldwell, N. 1984, PASP, 96, 287
Caldwell, N., Kirschner, R.P., & Richstone, D.O. 1986, ApJ, 305, 136
Calvani, M., Fasano, G., & Franceschini, A. 1989, AJ, 97, 1319
Canizares, C.R., Fabbiano, G., & Trinchieri, G. 1987, ApJ, 312, 503
Caon, N., Capaccioli, M., & Rampazzo, R. 1990, A&AS, 86, 429 (=CCR)
Capaccioli, M. 1985, New Aspects of Galaxy Photometry, ed. J.-L. Nieto (New York & London: Springer–Verlag), p. 53.
Capaccioli, M. 1987, IAU Symp. No. 127, Structure and Dynamics of Elliptical Galaxies, ed. T. de Zeeuw (Dordrecht: Reidel), p. 47.
Capaccioli, M. 1989, Second Extragalactic Astronomy Regional Meeting (Cordoba, Argentina) (Cordoba: Academia de Ciencias), p. 317
Capaccioli, M. 1989, Le Monde des Galaxies (Paris), eds. H.G. Corwin Jr. and L. Bottinelli (Berlin: Springer–Verlag), p.208
Capaccioli, M. 1990, Bulges of Galaxies (La Serena), eds. B. Jarvis and D.M. Terndrup (Garching: ESO Workshop Publ.), p. 231
Capaccioli, M., & Caon, N., 1989, First ESO/ST–ECF Data Analysis Workshop, eds. P.J. Grosböl, F. Murtagh, and R.H. Warmels (Garching: ESO), p. 107
Capaccioli, M., & Caon, N. 1991, MNRAS, 248, 523
Capaccioli, M., & Vietri, M. 1989, Proc. of the Yellow Mountain Summer School, (Yellow Mountain, China), p. 150
Capaccioli, M., Caon, N., & Rampazzo, R. 1990, MNRAS, 242, 24p
Capaccioli, M., Fasano, G., & Lake, G. 1984, MNRAS, 209, 317
Capaccioli, M., Held E.V., & Nieto J.–L. 1987, AJ, 94, 1519
Capaccioli, M., Vietri, M., & Held, E.V. 1988, MNRAS, 234, 335
Capaccioli, M., Cappellaro, E., Della Valle, M., D'Onofrio, M., Rosino, L., & Turatto, M. 1990b, ApJ, 350, 110
Capaccioli, M., Vietri, M., Held, E.V., & Lorenz, H., 1991, ApJ, 371, 535
Cappellaro, E., Capaccioli, M., & Held, E.V. 1990, The Messenger, 58, 48
Carlberg, R.G. 1984, ApJ, 286, 416
Carlberg, R.G. 1986, ApJ, 310, 593
Carter, D. 1987, ApJ, 312, 514
Ciotti, L., D'Ercole, A., Pellegrini, S. & Renzini, A. 1991, ApJ, 376, 380
Corwin, H.G.Jr., de Vaucouleurs, G. & de Vaucouleurs, A. 1985, University of Texas Monographs in Astronomy, 5 (Austin: Texas Univ. Press)
Davies, R.L. 1987, IAU Symp. No. 127, Structure and Dynamics of Elliptical Galaxies, ed. T. de Zeeuw (Dordrecht: Reidel), p. 63
Davies, R.L., Efstathiou, G., Fall, S.M., Illingworth, G., & Schechter, P.L. 1983, ApJ, 266, 41
de Carvalho, R.R., & Djorgovski, S., 1989, ApJ, 341, L37
de Vaucouleurs, G. 1948, Ann. d'Astrophys., 11, 247

de Vaucouleurs G. 1959, Handbuch der Phys., 53, 275
de Vaucouleurs, G., & Capaccioli, M. 1979, ApJS, 40, 699
de Vaucouleurs, G., de Vaucouleurs, A., & Corwin, H.G. Jr. 1976, Second Reference Catalogue of Bright Galaxies (Austin: Texas Univ. Press) (RC2).
de Vaucouleurs, G., & Olson, D.W. 1982, ApJ, 230, 697
de Zeeuw, P.T., & Franx, M. 1989, ApJ, 343, 617
Djorgovski, S.B. 1985, Ph.D. Thesis, Univ. of California at Berkeley
Djorgovski, S., & Davis, M. 1987, ApJ, 313, 59
Djorgovski, S., de Carvalho, R., & Han, M.-S. 1989, The extragalactic distance scale, ed. S. van den Bergh & C.J. Pritchet (Provo: Brigham Young University Print Service), p. 239
Dressler, A. 1979, ApJ, 231, 659
Dressler, A. 1980, ApJ, 236, 351
Dressler, A. 1987, ApJ, 317, 1
Dupraz, C., & Combes, F. 1986, A&A, 166, 53
Ebneter, K. & Balick, B. 1985, AJ, 90, 183
Efstathiou, G., & Fall, S.M. 1984, MNRAS, 206, 453
Fabbiano, G. 1989, ARA&A, 27, 87
Fabbiano, G., Gioia, I.M., & Trinchieri, G. 1989, ApJ, 347, 127
Faber, S.M. 1977, in The Evolution of Galaxies and Stellar Population, eds. B.M. Tinsley, & R.B. Larson (New Haven: Yale University Observatory), p. 157
Faber, S.M., & Jackson, R.E. 1976, ApJ, 204, 668
Fasano, G. 1987, IAU Symp. No. 127, Structure and Dynamics of Elliptical Galaxies, ed. T. de Zeeuw (Dordrecht: Reidel), p. 395
Fasano, G. 1991, MNRAS, 249, 208
Fasano, G. 1991, & Vio, R. 1991, MNRAS, 249, 629
Ferguson, H.C. 1989, AJ, 98, 367
Forman, W., Jones, C., & Tucker, W. 1985, ApJ, 293, 102
Franx, M., & Illingworth, G. 1988, ApJ, 327, L55
Franx, M., Illingworth, G.D., & Heckman, T. 1989, ApJ, 344, 613
Franx, M., & Illingworth, G. 1990, ApJ, 359, L41
Freeman, K.C. 1970, ApJ, 160, 811
Freeman, K.C. 1983, in IAU Symposium 106, The Milky Way Galaxy, ed. H. van Woerden (Dordrecht: Reidel).
Gerhard, O.E. & Binney, J. 1985, MNRAS, 219, 467
Gerhard, O.E. & Vietri, M. 1986, MNRAS, 223, 377
Giacconi, R., Branduardi, G., Briel, U., Epstein, A., Fabricant, D. *et al.* 1979, ApJ, 230, 540
Gorgas, J., Efstathiou, G., & Aragon Salamanca, A. 1990, MNRAS, 245, 217
Gott, J.R., & Thuan, T.X. 1976, ApJ, 204, 649
Greggio L. and Renzini A., 1990: ESO preprint n. 697
Hamabe, M., & Kormendy, J. 1987, IAU Symp. No. 127, Structure and Dynamics of Elliptical Galaxies, ed. T. de Zeeuw (Dordrecht: Reidel), p. 379

Heckman, T.M. 1980, A&A, 87, 152
Hernquist, L., & Quinn, P.J. 1987, ApJ, 312, 1
Hernquist, L., & Quinn, P.J. 1988, ApJ, 331, 682
Hoessel, J.G., & Schneider, D.P. 1985, AJ, 90, 1468
Hubble E. 1926, ApJ, 64, 321
Hubble E. 1930, ApJ, 71, 231
Illingworth, G. 1977, ApJ, 218, L43
Jaffe W. 1983, MNRAS, 202, 995
Jedrzejewski, R.I. 1987, MNRAS, 226, 747
Jensen, E.B., & Thuan, T.X. 1982, ApJS, 50, 421
Katz, N., & Richstone, D.O. 1985, ApJ, 296, 331
Kent, S.M. 1985, ApJS, 59, 115
King, I. 1962, AJ, 67, 471
King, I. 1966, AJ, 71, 276
King, I. 1978, ApJ, 222, 1
Knapp, G.R., Turner, E.L., & Cunniffe, P.E. 1985, AJ, 90, 454
Knapp, G.R., Guhathakurta, P., Kim, D.-W., & Jura, M. 1989, ApJS, 70, 329
Kodaira, K., Okamura, S., & Watanabe, M. 1983, ApJ, 274, L49
Kodaira, K., Watanabe, M., & Okamura, S. 1986, ApJS, 60, 475
Kormendy, J. 1977, ApJ, 217, 406
Kormendy, J. 1982, in Morphology and Dynamics of Galaxies, ed. L. Martinet, M. Mayor, (Sauverny: Geneva Obs.), p. 113
Kormendy, J. 1985, ApJ, 292, L9
Kormendy, J., & Djorgovski, S. 1989, ARA&A, 27, 235
Lake, G. 1979, in Photometry, Kinematics and Dynamics of Galaxies, D.S. Evans ed., Austin, p. 381
Lauer, T.R. 1985, ApJS, 57, 473.
Lauer, T.R. 1985, ApJ, 292, 104
Lindblad, B. 1956, Stockolm Obs. Ann., 19, No. 2
Londrillo, P., Messina, A., & Stiavelli, M. 1991, MNRAS, 250, 54
Longo, G., Capaccioli, M., Bender, R., & Busarello, G. 1989, A&A, 225, L17
Malin, D.F., & Carter, D. 1983, ApJ, 274, 534.
Malumuth, E.M., & Richstone, D.O. 1984, ApJ, 276, 413
Malumuth, E.M., & Kirshner, R.P. 1985, ApJ, 291, 8
Marchant, A.B., & Olson, D.W. 1979, ApJ, 230, L157
May, A., van Albada, T.S., Norman, C.A. 1985, MNRAS, 214, 131
Merrit, D. 1982, AJ, 87, 1279
Michard, R. 1984, A&A, 140, L39
Murtagh, F., & Heck, A. 1987, Multivariate Data Analysis, Dordrecht:Reidel
Nesci, R., & Perola, G.C. 1985, A&A, 145, 296
Nieto, J.-L., & Bender, R. 1989, A&A, 215, 266
Nieto, J.-L., Bender, R., & Surma, P. 1991, A&A, 244, L37
Nieto, J.-L., Capaccioli, M., & Held, E.V. 1988, A&A, 195, L1

Nieto, J.-L., Bender, R., Arnaud, J., & Surma, P. 1991, A&A, in press
Oemler A. 1976, ApJ, 209, 693
Peletier, R., Davies, R.L., Illingworth, G.D., Davis, L.E., Cawson, M. 1990, AJ, 100, 1091
Phillips, M.M., Jenkins, C.R., Dopita, M.A., Sadler, E.M., & Binette, L. 1986, AJ, 91, 1062
Porter, A.C. 1988, PhD thesis, Calif. Inst. Technol., Pasadena
Quinn, P.J., & Hernquist, L. 1987, IAU Symp. No. 127, Structure and Dynamics of Elliptical Galaxies, ed. T. de Zeeuw (Dordrecht: Reidel), p. 249
Richstone, D.O. 1979, ApJ, 234, 825
Rix,H.-W., & White, S.D.M. 1990, ApJ, 362, 52
Sandage, A., & Tammann, G.A. 1981, A revised Shapley–Ames Catalog of Bright Galaxies, (Washington, DC: Carnegie Inst. Washington)
Sandage, A., Freeman, K.C., & Stokes, N.R. 1970, ApJ, 160, 831
Sandage, A., Binggeli, B., & Tammann, G.A. 1987, AJ, 90, 1759
Sarazin, C.L. 1986, Rev. Mod. Phys., 58, 1
Schombert, J.M. 1986, ApJS, 60, 603
Schombert, J.M. 1988, ApJ, 328, 475
Schönberber, D. 1983, ApJ, 272, 708
Schweizer, F. 1982, ApJ, 252, 455
Schweizer, F. 1983, IAU Symp. No. 100, Internal Kinematics and Dynamics of Galaxies, ed. E. Athanassoula (Dordrecht: Reidel), p. 319
Schweizer, F. 1987, IAU Symp. No. 127, Structure and Dynamics of Elliptical Galaxies, ed. T. de Zeeuw (Dordrecht: Reidel), p. 109
Schweizer, F., & Ford, W.K. 1985, New Aspects of Galaxy Photometry, ed. J.-L. Nieto (New York & London: Springer–Verlag), p. 145
Schweizer, F. & Seitzer, P. 1988, ApJ, 328, 88
Scorza, C., & Bender, R. 1990, A&A, 235, 49
Scoville, N.Z., & Sanders, D.B. 1987, in Interstellar Processes, eds. D.J. Hollenbach and H.A. Thronson (Reidel.), p. 21
Sersic J.-L. 1968, Atlas de Galaxias Australes (Cordoba: Observatorio Astronomico).
Shaw, M.A., & Gilmore, G. 1989, MNRAS, 237, 903
Shaw, M.A., & Gilmore, G. 1990, MNRAS, 242, 59
Silva, D.R., Boroson, T.A., Thompson, J.B., & Jedrzejewski, R. 1989, AJ, 98, 131
Simien, F., & Michard, R. 1990, A&A, 227, 11
Soifer, B.T., Houck, J.R., & Neugebauer, G. 1987, ARA&A, 25, 187
Terlevich, R., Davies, R.L., Faber, S.M., & Burstein, D. 1981, MNRAS, 196, 381
Thomsen, B., & Baum, W.A. 1989, ApJ, 347, 214
Thronson, H.A., & Bally, J. 1987, ApJ, 319, L63
Tinsley, B.M. 1980, Fund. Cosmic Physics, 5, 287
Tonry, J., & Davis, M. 1981, ApJ, 246, 680
Trevisani, S. 1991, Thesis, University of Padova.

Trinchieri, G., & di Serego Alighieri, S. 1991, AJ, 101, 1647
Trinchieri, G., Fabbiano, G., & Canizares, C.R. 1986, ApJ, 310, 637
Vader, J.P., Vigroux, L., Lachieze-Rey, M. & Souviron, J. 1988, A&A, 203, 217
van den Bergh, S. 1990a, PASP, in press
van den Bergh, S. 1990b, ApJ, 348, 57
van der Kruit, P.C. 1987, A&A, 173, 59
van der Kruit, P.C., & Searle, L. 1982, A&A, 110, 79
van Driel, W., & de Jong, T. 1990, A&A, 227, 6
van Driel, W., & van Woerden, H. 1991, A&A, 243, 71
van Houten, C.J. 1961, Bull. Astron. Netherlands, 16, 1
Veron, P., & Veron, M.-P. 1985, A&A, 145, 433
Wardle, M., & Knapp, G.R. 1986, AJ, 91, 23
White, S.S.M. 1979, MNRAS, 189, 831
White, S.D.M. 1982, Morphology and Dynamics of Galaxies, ed. L. Martinet, M. Mayor (Sauverny: Geneva Obs.), p 289
White, S.D.M., 1987, IAU Symp. No. 127, Structure and Dynamics of Elliptical Galaxies, ed. T. de Zeeuw (Dordrecht: Reidel), p. 339
Whitmore, B.C. 1980, ApJ, 242, 53
Whitmore, B.C., McElroy, D.B., & Tonry, J.L. 1985, ApJS, 59, 1
Whitmore, B.C., Mc Elroy, D.B., & Schweizer, F. 1987a, ApJ, 314, 439
Whitmore, B.C., Mc Elroy, D.B., & Schweizer, F. 1987b, IAU Symp. No. 127, Structure and Dynamics of Elliptical Galaxies, ed. T. de Zeeuw (Dordrecht: Reidel), p. 413
Wiklind, T. 1991, Dynamics of Galaxies and Their Molecular Cloud Distribution, eds. F. Combes & F. Casoli, p. 33
Wiklind, T., & Henkel, C. 1989, A&A, 225, 1
Williams, T.B., & Schwarzschild, M. 1979, ApJ, 227, 56
Wrobel, J.M., & Heeschen, D.S. 1991, AJ, 101, 148
Wyse, R.F.G., & Gilmore, G. 1988, AJ, 95, 1404
Young, P.J., Sargent, W.L.W., Kristian, J., & Westphal, J.A. 1979, ApJ, 234, 76